NUMERICAL SIMULATION OF ARCTIC OFFSHORE STRUCTURES INTERACTING WITH LEVEL ICE AND NONLINEAR TIME-DOMAIN SIMULATIONS OF ARCTIC SPAR

A Dissertation

by

HAKUN JANG

Submitted to the Office of Graduate and Professional Studies of
Texas A&M University
in partial fulfillment of the requirements for the degree of

DOCTOR OF PHILOSOPHY

Chair of Committee,	Moo-Hyun Kim
Committee Members,	Jeffrey Falzarano
	Richard Mercier
	Steve DiMarco
Head of Department,	Sharath Girimaji

December 2018

Major Subject: Ocean Engineering

ABSTRACT

One of the greatest challenges of developing the arctic regions is the harsh environmental conditions caused by the presence of ice. When offshore structures interact with ice, significant structural motion is induced by the ice load, which influences the overall structural robustness. In this study, three different numerical tools are developed to investigate the ice-structure interaction using three scenarios. First, the fixed-type monopile offshore wind turbine in level ice is studied. Because the crushing is the dominant failure mode of level ice against a cylindrical structure, a mechanical ice-crushing model is developed to estimate the ice force on the structure in time domain. The model is further implemented into the wind turbine analysis software, FAST, developed by National Renewable Energy Laboratory (NREL). Second, the floating offshore platform, Artic Spar, in level ice is investigated by employing an analytical method. Artic Spar is characterized by the inverted cone-shaped hull near the waterline so that level ice can fail when bending. The fully coupled floater-riser-mooring dynamic analysis program, CHARM3D, is extended by implementing the analytical ice-bending model. Third, the numerical software for the interaction between level ice and an arbitrary-shaped floating offshore structure is developed by coupling two software programs, LIGGGHTS and CHARM3D. Based on the discrete element method, level ice is modelled as an assembly of multiple spherical particles, and the bonding parallel method is employed to consider the interaction force among the bonded particles. Throughout the newly developed

numerical simulation tools, the ice load on different offshore structures is numerically estimated, and the corresponding structural performances are systematically investigated. In addition to these three ice-structure interactions, the nonlinear behavior or Arctic Spar is investigated in time domain. To capture the nonlinearity of platform motions, a nonlinear time-domain simulation tool considering the nonlinear hydro-restoring coefficient and nonlinear Froude-Krylov force is developed by extending CHARM3D with a body-nonlinear method. The heave-to-pitch and heave-to-heave Mathieu instabilities of Arctic Spar are also investigated in both regular and irregular waves.

DEDICATION

To My Heavenly Father

Jesus Christ

To My Wife

Shinhee Jeong

To My Son

Aaron Yeju Jang

To My Parents

Kwangsub Jang and Youngsuk Lee

And

To Their Love for Me

ACKNOWLEDGEMENTS

First, and most of all, I would like express my sincere gratitude to my advisor, Dr. Moo-Hyun Kim, for his expertise, encouragement, patience, and guidance throughout the course of this research. Without his valuable assistance, this dissertation would not have been completed. I would also like to thank my committee members, Dr. Falzarano, Dr. Mercier, and Dr. DiMarco, for their guidance and support during my research.

I also want to thank Dr. Gordon whose encouragement and advice have been especially valuable throughout my doctoral studies. Thanks also go to my friends and colleagues and the department faculty and staff for making my time at Texas A&M University a great experience.

Additional gratitude is offered to my mother, father, and sister for their continuous encouragement and continued support over the years. Finally, I would like to express special thanks to my lovely wife, Dr. Shinhee Jeong, for her patience and love.

CONTRIBUTORS AND FUNDING SOURCES

Contributors

This work was supervised by a dissertation committee consisting of Dr. Moo-Hyun Kim and Dr. Falzarano of the Department of Ocean Engineering, Dr. Mercier of the Department of Civil Engineering, and Dr. DiMarco of the Department of Oceanography.

All work for the dissertation was completed by the student, under the advisement of Dr. Moo-Hyun Kim of the Department of Ocean Engineering.

Funding Sources

Graduate study was supported by a fellowship from Texas A&M University and a scholarship from American Bureau of Shipping (ABS) and British Petroleum (BP).

TABLE OF CONTENTS

Page

LIST OF FIGURES

Page

LIST OF TABLES

Page

CHAPTER I

INTRODUCTION

1.1 Motivation of the Research

Numerous research activities related to arctic offshore development have been conducted over the past few decades as interest in developing the arctic region has increased. The most important discovery in the arctic region has been the massive amount of hydrocarbon. In 2008, a team from the U.S. Geological Survey (USGS) first published a comprehensive assessment of potential oil/gas reserves in the north arctic region (Bird et al., 2008). It stated that the largest underdeveloped region for petroleum on Earth was the arctic continent. According to the assessment, 13% of the world's undiscovered oil and 30% of the undiscovered gas may remain in the arctic (see Figure 1). Approximately 81% of new oil and gas exploration is expected to occur offshore under less than 500 meters of water.

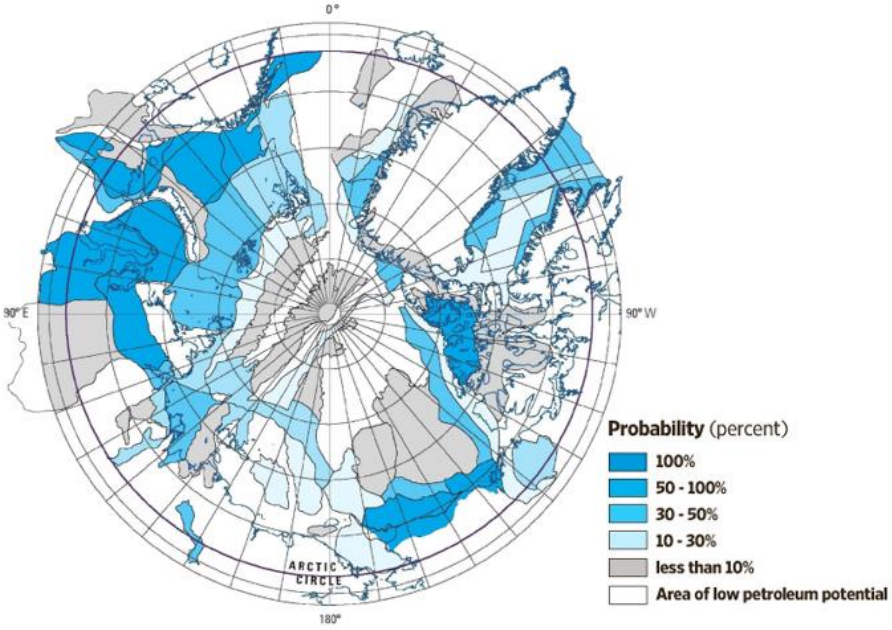

Figure 1. The probability of the presence of at least one undiscovered oil and/or gas field with recoverable resources greater than 50 million barrels of oil equivalent (Bird et al., 2008(USGS))

Climate change and the melting arctic sea ice have also led to more open-water regions and longer periods throughout the year for oil and gas exploration. The effects of global warming including the rising temperatures in the arctic have given unprecedented, increased marine access throughout the arctic basin. The melting and thinner sea ice has extended the ice-free navigation season and enhanced ship transit. For instance, the Northern Sea Route (NSR) is more navigable. Liu and Kronbak (2010) stated that the sailing distance from Asia to Europe could be reduced by about 40% if ships could pass through the Arctic Ocean via the NSR, compared to the traditional route. Additionally, with increased energy development activities in Russian waters, the transport volumes on the NSR and the Northwest Passage have increased significantly with escorts and

guidance from icebreaking vessels. Within several years, it is expected that non-ice strengthened vessels could navigate through the NSR for at least two months each summer.

Increased offshore wind energy development activities have also been conducted around north European nations due to their limited fossil energy and environmental protection. Since the wind in offshore sites is steadier and stronger than on-land wind, offshore wind farms have been strongly proposed. In Finland, for example, interest in developing offshore wind farms has grown, with 3000 MW offshore projects under investigation or in preparation (Salo and Syri, 2014). Since 2017, the Tahkoluoto offshore wind farm in Finland has operated 10 offshore wind turbines (OWTs) with a capacity of 4.2 MW for each, and produced 155 GWh annually. By 2030, Sweden is also expected to supply 30 TWh annually from offshore wind energy (Jacobsson et al., 2014).

Despite the interest and progress, however, enormous challenges exist in developing arctic regions. In particular, harsh environmental conditions such as severe wave and wind loads as well as ice impacts make arctic development more difficult. Since ice actions are influenced by various factors from ice properties to structure types and shapes, designing offshore structures in arctic regions is much more challenging than conventional offshore structures. In addition, one of the greatest concerns is what impact arctic activities would have on the fragile arctic ecosystem and how to clean up an oil or gas spill in icy conditions. Therefore, the integrity and safety of offshore structures should be assessed and secured to prevent unexpected accidents when conducting arctic activities. Before proceeding with development, the appropriate organizations should investigate these considerations to prevent environmental problems.

Although considerable arctic exploration and development have been successfully carried out since the late 1960s without significant incidents, some structures have experienced severe structural vibrations induced by ice interactions. The field experiences of the Cook Inlet oil and gas production platforms (Figure 3) revealed that resonant type vibration can be caused by varying ice thickness and velocity. For example, the cylindrical steel mono-pile type lighthouse in the Gulf of Bothnia, as shown in Figure 4, experienced ice-induced vibration and was self-excited during the winter of 1974. These ice-induced vibrations have not only occurred with narrow and slender structures, but also with wide structures. In 1986, a steel caisson drilling structure, Molikpaq, operating in the Beaufort Sea measured local ice loads and platform displacement with harmful dynamic ice loads at its lowest natural frequency.

As an ice class drillship, the semi-submersible conical platform, Kulluk, was used in the Beaufort or Chukchi Seas in the 1980's and 1990's. This moored-floating vessel operated in heavy pack-ice conditions with the support of icebreakers. It collected extensive environmental data and identified the factors affecting the global performance of the platform and mooring dynamics.

In 2010, the International Standards Organization (ISO) published an International Standard for Arctic Offshore Structures stating that with a practical level of reliability with respect to safety, environmental protection can be achieved by offshore structures in arctic and cold regions. It was the first international standard based on full-scale data and observations that were compiled between 1965 and 2007 in the Beaufort Sea, Cook Inlet, Baltic Sea, the Gulf of Bohai, and to a limited extent the Sea of Okhotsk. It specifies the

requirements and provides guidance for the design, construction, transportation, installation, and removal of offshore structures, related to the activities of the petroleum and natural gas industries in arctic and cold regions (ISO 19906 Standard). It also describes the ice properties, the effects on the interaction with structures, and the design loads for various types of structures including fixed, floating, and subsea structures.

These guidelines are useful, but there is still limited information available to reliably design an offshore structure in the arctic. There is also a lack of consensus and practical experience. Palmer (2011) indicated that some informative sections in the International Standard for Arctic Offshore Structures document do not provide quantitative guidance. For example, the design load for a dynamic analysis and the interaction between ice and a structure were excluded, which makes it difficult to demonstrate ice-induced vibration. As a result, additional industrial research activities have been conducted to provide more detailed information. The Russian-Norwegian Barents 2020 projects in phase 4 (2012) performed gap identification and analysis particularly for the floater design under external environmental loadings caused by ice. Based on the identified gaps, they suggested additions and amendments to ISO 19906:2010, which included adding a definition for a stationary floating structure, clarification of the ice event terms, requirements about ice management, and amending clauses to be more relevant for floating structures with disconnect availability. Since the ISO 19906 standard does not provide any guidance on the design of floating structures, the ICESTRUCT joint industry project (JIP) led by DNV from 2009 to 2013 also attempted to develop designer-friendly methods to determine ice load characteristics and effects on fixed and floating offshore structures.

1.2 Objectives

Numerous studies have been conducted to help arctic development projects more reliable and safer. From a naval engineer's perspective on structural dynamics, the author of the current study would like to focus more on the dynamic interaction between ice and structures. For this purpose, it is important to determine specific scenarios of the interaction between ice and structures, because the analysis procedures of each scenario must be considered differently, depending on the types of ice, ice properties, and shapes of the structures. Therefore, the aims of the current research are as follows:

- Develop an ice and fixed mono-pile interaction model that reliably estimates the ice forces on the pile during interaction. It will be further applied to the offshore fixed type wind turbine analysis. In northern European countries, there has been increased interest in developing offshore wind turbines in cold regions. Advanced technology is needed to meet this demand for offshore wind farms. The developed model is implemented in an offshore wind turbine simulator, FAST, developed by the National Renewable Energy Laboratory (NREL) and is used for the coupled dynamic simulation in time domain. The performance of an offshore wind turbine in operational and parked conditions is assessed under various ice conditions.
- Develop an ice and floating structure interaction model that reliably calculates the ice forces on the floater, compared with the experimental data, and physically demonstrates the interaction phenomenon. The study examines the various factors of ice properties to investigate these effects on structure dynamics. This model is

combined with the coupled floater-mooring dynamic simulator, CHARM3D, developed by Professor Moo-Hyun Kim's group over decades. The global behavior of a floater as well as the mooring dynamics are investigated under various design conditions.

- Develop a universal simulation tool by taking the advantage of the discrete element method tool (LIGGGHTS). By modeling level ice with multiple bonded particles, the ice load on the structure, which is not limited to the square shape hull, is estimated. This discrete element method tool is also coupled with CAHRM3D to analyze the fully-couple, ice-floater-mooring dynamics simultaneously in time domain, while minimizing the assumptions and limitations. The coupling is achieved externally using the named pipe method and MPI coding. The ice forces on floating structures are compared to those on fixed structures and the global performance of floating structures is discussed.
- Develop a numerical algorithm to examine the nonlinear effects on Arctic Spar with an inverted conical shape hull near the mean water level. The irregular hull shape of Arctic Spar would induce the nonlinear wave interaction with large increased wave forces. In this study, the partially nonlinear time-domain method is introduced by considering the time-varying restoring coefficients and Foude-Krylov forces for Arctic Spar. The structural integrity is discussed under both regular and irregular wave conditions. Finally, the Mathieu instability in the pitch and heave directions are investigated.

CHAPTER II

LEVEL ICE AND FIXED MONO-PILE INTERACTION INDUCED BY ICE CRUSHING FAILURE*

2.1 Introduction

Due to limited oil/gas energy, wind energy is one of the fastest growing renewable energy resources. In particular, offshore wind energy is attractive because of the higher-quality (stronger and steadier) wind, fewer regulations, and no opposition from coastal residents. Therefore, countries located in the northern region with cold climates are particularly interested in developing offshore wind farms.

The greatest challenge for developing arctic offshore wind farms, however, is the harsh environmental conditions. Icing increases the mass on the blades of offshore wind turbines (OWTs) and affects aerodynamic performance by increasing the thrust load, resulting in a reduction of power production. For a bottom-fixed wind turbine, a severe ice load could be applied dynamically on the OWT foundation system, and may cause

* Part of this chapter is reprinted with permission from "Numerical Simulation of Offshore Wind Turbine Dynamics in Drifting Level Ice" by Jang and Kim, 2017. Proceedings of the 27th (2017) International Ocean and Polar Engineering Conference, Copyright [2017] by the International Society of Offshore and Polar Engineers (ISOPE)

failure of the supporting structures. In addition, offshore structures may experience resonance-type motion from serious ice-induced vibration.

In this study, the dynamic ice-structure interaction of the bottom-fixed wind turbine is studied numerically. The numerical method to estimate the ice load for a compliant cylindrical structure is implemented into the aero-hydro-servo-elastic tool, FAST v7 (Jonkman and Buhl, 2005), to investigate the interaction between the level ice and OWT. A monopile-type supporting structure is selected, and the ice is assumed to fail due to ice crushing the vertical cylinder. The dynamics of an OWT tower and blades are examined in parked and operating conditions by varying the ice drift velocity.

2.2 Literature Review

The interaction of level ice against a vertical cylindrical structure involves a complicated process with different failure modes such as splitting, bending, buckling, crushing, creep, and mixed mode. Among these failure modes, the severe self-excited vibration of a structure is most likely to occur from ice crushing failure with a large ice load. Several characteristics of ice crushing failure can be drawn from experiment and field data:

- Loading rate: The maximum compressive strength of ice significantly depends on the rate of deformation and the strain rate (Schulson, 2001; Timco and Weeks, 2010). The damage process of creep occurs at lower strain rates, while fractures and spalls (brittle behavior) occur at higher strain rates. According to ISO 19906, the uniaxial

compressive strength of first-year ice has the maximum strength at a strain rate of approximately $10^{-3}s^{-1}$ where ice failure transitions from ductile to brittle failure.

- Nonlinear ice stiffness on low and high loading rates: Karna and Jarvinen (1994) conducted laboratory indentation tests and observed a strain-softening effect as the ice force approaches the peak value. He stated that at a low strain rate, ice deformed inelastically after about 20~30% of the total displacement of ice. Hendrikse and Metrikine (2015) studied the ice-structure interaction numerically by modeling combinations of a spring-dashpot-slider system and considered the plastic deformation of ice at a low strain rate while the strain modulus remained linear at a high strain rate.
- Non-simultaneous failure: The local effects of crushing failure increase as an ice sheet continuously crushes against a very wide structure. Kry (1978) developed a formula using a statistical approach to estimate the influence of structure width on design stress. Based on the empirical data from relatively narrow structures, Kry found that the effective stress decreased non-linearly with an increase in the contact area or number of zones due to non-simultaneous failure. Ashby et al. (1986) also presented a statistical method to describe the analytical relationship between the compressive strength and volume of ice. Their results accounted for the size effects in ice through non-simultaneous failure and were in good agreement with the field measurements. According to a series of indentation tests conducted by Sodhi (1998), the indentation velocity effect on the failure mode was examined such that a random or non-simultaneous failure by brittle flacking occurred at a high indentation velocity. He

also presented the concept of crushing zones which interacted with ice independently and indicated that the number of crushing zones increased with increasing drifting velocity.

To demonstrate the ice-structure interaction with a crushing failure mode, Matlock et al. (1971) introduced a simple mechanical linear model consisting of a mass-dashpot-spring system. They envisioned drifting ice as a series of ice teeth. When ice contacts a structure, it deflects and the ice force increases proportional to the relative displacement between the structure and ice. When the critical deflection of an ice tooth occurs, ice fails, and the ice force drops to zero. After that, the structure swings back until the structure is in contact with the next ice tooth.

The Matlock method has been widely modified and extended further by many researchers for decades. In particular, Karr et al. (1993) studied the Matlock model in depth and identified periodic behaviors of the system response, revealing that ice-induced vibration is a complex nonlinear dynamic process, and a slight variation in ice parameters significantly changes the predicted response. In addition, they stated that due to the existence of multiple periodic solutions, dynamic interaction is more complicated and nonlinear. Huang et al. (2009) extended the Matlock model with time-varying ice strength depending on the strain rate. They examined the steady response of a structure and captured the frequency lock-in mode of ice failure and a structure. Withalm et al. (2010) modified this model further by adding the zonal concept. The ice contact area is divided into several zones that interact with the structure individually. They concluded that the

transition velocities changing the ice failure behavior from ductile to brittle modes is influenced by not only the ice proprieties but also the structural parameters.

Studies about offshore wind turbine subjected to ice impacts have also been conducted both numerically and experimentally. Following up on the development of a Danish offshore wind farm, extensive model tests have been conducted to investigate the key issues for the design of ice loads and loading behavior. Barker et al. (2005) tested seven different model configurations and observed four distinct ice failure modes: flexure, crushing, mixed mode, and lock-in. Gravesen et al. (2005) further analyzed those experimental results to develop design methods for practical applications for offshore wind turbines. They produced a time history of ice and wind combined loads under extreme conditions for a dynamic analysis of offshore wind turbines. They also presented a methodology of the design procedure for offshore wind turbines. In parallel studies, Heinonen et al. (2011) and Hetmanczyk et al. (2011) investigated the overall performance of a cylindrical offshore wind turbine subjected to ice loads using the Maattanen-Blenkarn ice-model with OnWind wind turbine simulation software. They analyzed various conditions to account for the influences of ice velocity, thickness, structural damping and stiffness on global performance. Wei Shi et al. (2016) presented a study of ice-structure interaction of a conical mono-pile type offshore wind turbine in drifting level ice. The ice model based on empirical parameters from ships tests is coupled with the aero-hydro-servo-elastic tool, HAWC2. They concluded that the ice thickness significantly affected the response of OWT and could cause significance vibrations in the structure.

The latest version of numerical software, FAST (v8.16.00a-bjj), which is modified and used in this study, originally has two ice-load-calculation modules for fixed mono-pile type offshore wind turbines. One module, IceFloe created by DNV GL, predetermines the ice loads in accordance with ISO 19906 and IEC 61400-3 standards and inputs the data into FAST. However, this module does not account for the bidirectional coupled interaction between the ice and the structure; thus, it is difficult to examine the frequency lock-in mode which may cause severe structure motion.

Another module, IceDyn, developed by the University of Michigan is capable of simulating various ice load cases with different ice failure modes and structure types. The simulation types on a sloped structure are divided into three modes: the buckling failure mode of wedge-shape ice, the creep and random ice crushing failure mode, and the bending failure mode. However, for the crushing failure model, some characteristics of the crushing failure are not included such as nonlinear stiffness, strain rate effects as well as ice-structure interaction model (unloading and extrusion phase).

2.3 Numerical Approach

In this study, Matlock's method is modified and extended to model the interaction between level ice and a fixed mono-pile under crushing failure. The zonal concept, where the contact area is divided into multiple zones, is used to model the non-simultaneous failure of ice. The compressive ice strength is modeled as a time-varying parameter,

depending on the loading rate, and nonlinear stiffness is introduced to capture the plastic deformation of ice.

2.3.1 Zonal concept

The non-simultaneous failure of crushed ice is observed in both model tests and field data, when the structure is wide or the ice drifting speed is relatively high. In order to simulate the non-simultaneous failure, the contact width is divided into *N* ice zones (Figure 2), and each zone is assumed to interact with the structure individually.

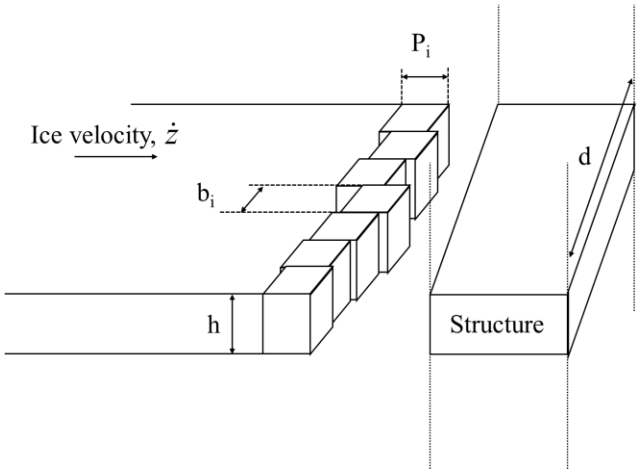

Figure 2. Illustration of ice zonal concept interating with a structure

This zonal concept was first introduced by Kry (1978) who predicted the total ice force on a wide structure using a statistical method. According to ice models from other literature (Ashby et al., 1986; Karna et al., 1999; Withalm et al., 2010; Hendrikse et al., 2015), each zone could be assumed to be statistically independent and equivalent, and these studies have resulted in good agreement with measurements.

2.3.2 Ice strength

The compressive strength of ice is strongly dependent on the strain rate. According to the studies by several researchers, (Michel and Toussaint, 1977; Kim and Keune, 2007; Withalm et al., 2010), the compressive strength, $\sigma_{c,i}$, of each zone corresponding to the full-scale regime is approximated as follows:

$$\sigma_{c,i} = \begin{cases} 4.6 \cdot \left(\dfrac{\dot{\varepsilon}}{5 \cdot 10^{-4}} \right)^{0.32} & \text{MPa for } \dot{\varepsilon}_i < 5 \cdot 10^{-4}\,\text{s}^{-1} \\ 4.6 \cdot \left(\dfrac{\dot{\varepsilon}}{5 \cdot 10^{-4}} \right)^{-0.1} & \text{MPa for } 5 \cdot 10^{-4}\,\text{s}^{-1} \le \dot{\varepsilon}_i \le 3 \cdot 10^{-2}\,\text{s}^{-1} \\ 3.0 & \text{MPa for } \dot{\varepsilon}_i > 3 \cdot 10^{-2}\,\text{s}^{-1} \end{cases} \quad (1)$$

where stain rate, $\dot{\varepsilon}_i = \dfrac{(z_i - u_i)}{\alpha \cdot b_i \cdot \Delta t_i}$

In the current model, with this compressive strength, the maximum force is calculated at every time step, and the instantaneous ice force is checked to determine whether it exceeds the maximum force. The strain rate of each zone is computed with the relative average velocity between a zone and structure, divided by the constant α and ice width, *b*. The constant α of 2 is selected as suggested by Ralston (1979).

2.3.3 Ice fracture pitch

P_i is the ice fracture length of an individual i^{th} zone which determines the ice force frequency and dynamic characteristics. Eranti et al. (1981) presented the deterministic

relationship of the ice fracture length as a function of the maximum force through small-scale experiments. They found that the ice fracture length proportionally increases with the maximum ice force.

$$P_i = \frac{\zeta \cdot F_{\max,i}}{b_i} + \Delta_{\max,i} \tag{2}$$

where the constant ζ is equal to 6.7 m^2/GN and Δ_{max} is the maximum deflection of the ice tooth.

2.3.4 Ice-structure interaction

In 1971, Matlock presented the ice-load mechanical model to describe the ice-structure interaction. It assumes that the ice is the series of ice teeth. The ice force increases linearly with the ice deflection Δ. The maximum ice force occurs when the ice force reaches its critical value F_{max}, and the force drops to the minimum value of ice force after breaking. Once the ice tooth is broken, the structure interacts with the next ice tooth sequentially. The process of this mechanical model describes the ice breaking and clearing away from the structure. This method has been adopted by many researchers (Matlock et al., 1971; Huang et al., 2009; Withalm et al., 2010) for decades. Recently, Hendrikse (2015) further considered the plastic deformation as well as nonlinear relationship between ice deflection and ice force.

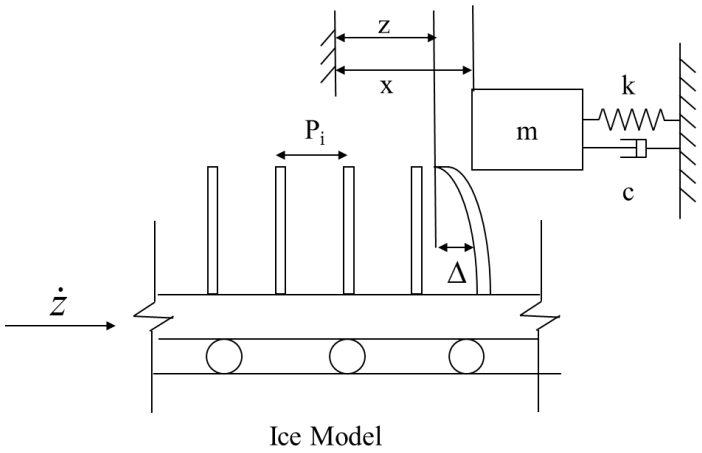

Figure 3. Ice-structure mechanical model by Matlock

In this study, ice-structure interaction is divided into three phases: the loading phase when the ice force increases with ice deformation, the unloading phase when the ice force decreases after ice breaking, and the extrusion phase when the crushed ice is cleared in the pulverized zone.

- Loading Phase

Two different ice stiffness modes are modeled in the loading phase to describe the nonlinear relation between ice stiffness and deformation. At low strain rates, ice fails in the ductile mode and shows inelastic deformation after about 20~30% of ice edge deformation. Therefore, a bilinear-type force-displacement relation is introduced when the strain rate is smaller than $5 \cdot 10^{-4} s^{-1}$. The linear relation between force and displacement is considered at high strain rates where the brittle failure occurs.

Deflection of an ice tooth can be calculated with the geometry consideration between the ice and the structure's position and velocity.

$$\Delta_i = \dot{z}t + z_{0,i} - x - \sum_{k=1}^{n-1} P_{k,i} \tag{3}$$

where $\dot{z}$ is the ice drift velocity, $z_{0,i}$ is the initial position of the first ice tooth, x is the position of the structure, P is the distance between the neighboring ice teeth, i represents the i^{th} zone, and n is the number of ice teeth completing the interaction with the structure. With the given deflection, the force is computed as follows:

$$F_i = \begin{cases} K_2 \cdot (\Delta_i - \Delta_{0,i}) + F_{0,i} \ , & \text{in ductile stress rate} \\ K_1 \cdot \Delta_i \ , & \text{otherwise} \end{cases} \tag{4}$$

where K_1 and K_2 are the penetration stiffness of ice, $F_{0,i}$ is the reference force that changes the ice stiffness, and $\Delta_{0,i}$ is the deflection corresponding to $F_{0,i}$. According to Karna et al. (1989), the ice penetration stiffness is calculated as Eq. (5).

$$K_1 = \left(\frac{1}{E_{eff} \cdot b_i} + \frac{4.58 - \nu}{\pi \cdot E_{ice} \cdot h} \right) \tag{5}$$

where E_{ice} is the elastic modulus of the ice, E_{eff} is the effective young's modulus equal to 5% of E_{ice}, ν is the Poisson's ratio of 0.33, and h is the ice thickness. The first and second terms account for a near-field and a far-field stiffness, respectively. The parameters, K_2

and F_0 were chosen as $0.2K_1$ and $0.3F_{max,i}$ based on studies by Karna (1994) and Hendrikse and Metrikine.(2015). The $\Delta_{0,i}$ can be found by manipulating the linear relation between K_1 and $F_{0,i}$.

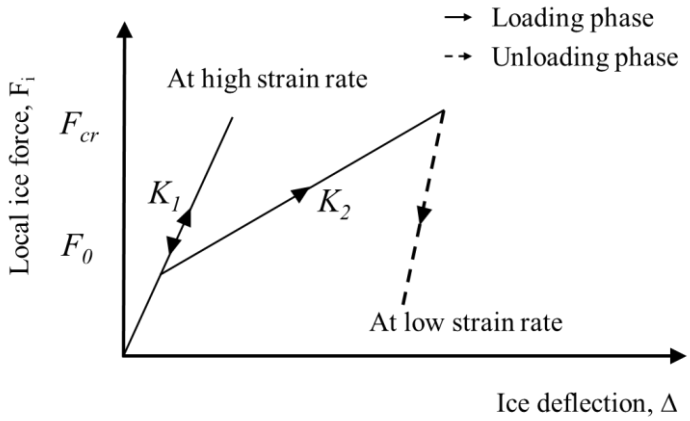

Figure 4. Ice load and deflection curve

- Unloading Phase

Once the ice force of zone *i* reaches the maximum crushing force, the unloading phase begins, and the ice force decreases. Karna's (1994) model tests revealed that the ice force did not abruptly drop after the peak, but it decreased gradually for the duration of around 10~20% of the loading time. The simple cosine smoothing function by Withalm et al. (2010) is adopted and modified to account for the unloading phase. By using the factor of 0.15, the ice force in unloading phase is calculated as Eq. (6). The unloading phase is maintained until the ice force reaches the extrusion force, F_e.

$$F_i = (\frac{F_{\max,i} - F_{e,i}}{2})[\cos(\frac{\pi(t - t_{failure,i})}{0.15 \cdot (t_{failure,i} - t_{contact,i})}) + 1] + F_{e,i} \quad (6)$$

$$for\ t_{failure,i} \le t \le t_{failure,i} + 0.15 \cdot (t_{failure,i} - t_{contact,i})$$

where $t_{contact,i}$ is the time when the ice tooth initially contacts the structure, and $t_{failure,i}$ is the time when the ice force of the ice tooth reaches the critical force, and the ice tooth is broken.

- Extrusion Phase

If the structure moves in the opposite direction of the drifting ice after the unloading phase, the structure would extrude the pulverized ice. During this time, the magnitude of the extrusion force F_e is assumed to be constant and identical as the minimum residual force from extrusion. Most authors (Karna et al., 1999; Huang et al., 2009) have considered it to be 10~20% of the previous peak force. The extrusion phase continues until the ice fracture pitch is reached, and the next loading cycle is reestablished.

2.3.5 Coupling and implementing into FAST

In this study, numerical simulations are conducted by extending FAST (see Figure 5), a coupled aero-hydro-servo-elastic numerical simulator developed by National Renewable Energy Laboratory (NREL), which is capable of analyzing wind turbine dynamics. FAST uses two combined methods. The nonlinear multi-body systems (MBS) formulation is applied for the dynamics of the entire system, while the finite element method (FEM) is used for sub-beam structures such as a tower and blades. The ice breaking module for the ice load calculation is implemented into the FEM scheme. FAST

feeds the position and velocity of the tower nodes around the mean sea level (MSL) and the ice breaking module calculates the global ice forces and moments, distributing them to the finite tower nodes interacting with the level ice. The calculated global ice loads are updated in every time step, and FAST solves the global equation of motion for an entire system including rotor dynamics.

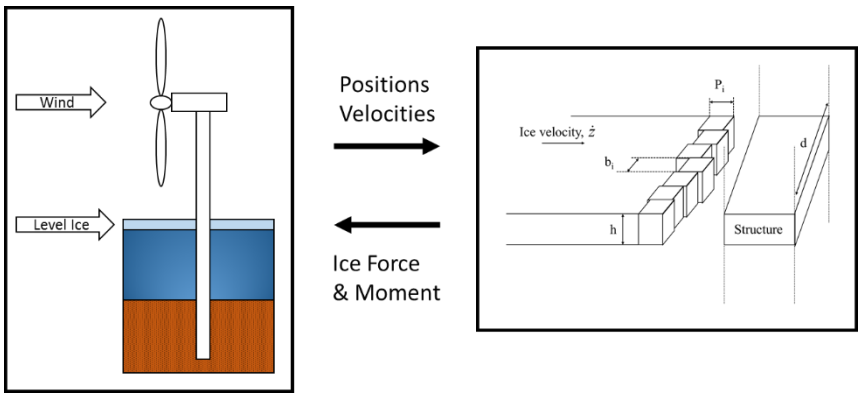

Figure 5. Numerical scheme for coupling

2.4 Validation of the Ice Crushing Model

To validate the ice crushing model, the numerical simulation results are compared to the experiment conducted by Sodhi (2001). He performed small-scale indentation tests with compliant structures to investigate the crushing failure during ice-structure interaction. Due to the limited information, only the interaction in the intermittent crushing range is compared in the current study. For the input parameters, the unknown

parameters are adopted from Hendrikse and Metrikine (2015). The test parameter used in the numerical simulation is tabulated in Table 1.

Table 1. Structure and Ice properties for intermittent crushing failure

Parameter	Value	Unit
Mass	300	kg
Damping coefficient	3000	kg/s
Stiffness	2.45	MN/m
Structure width	100	mm
Ice height	38	mm
Ice drifting velocity	36.30	mm/s
Ice crushing strength	8.78	MPa
Yong’s modulus	4	GPa
Number of zones	10	-

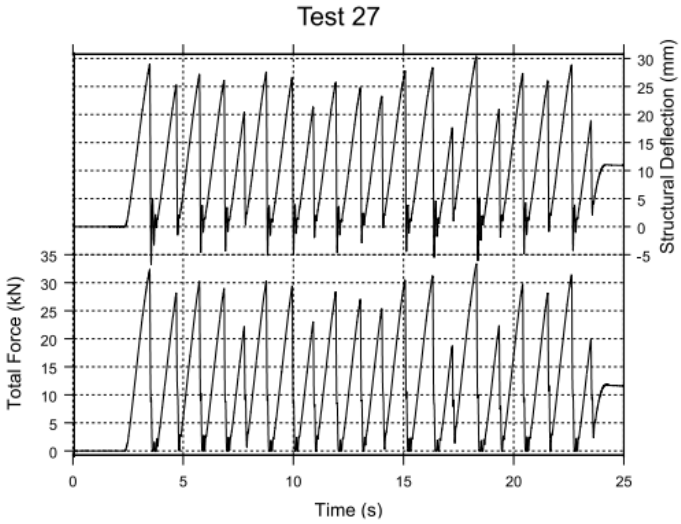

Figure 6. Time-history of interaction force and structural deflection based on the experiment (Sodhi, 2001)**

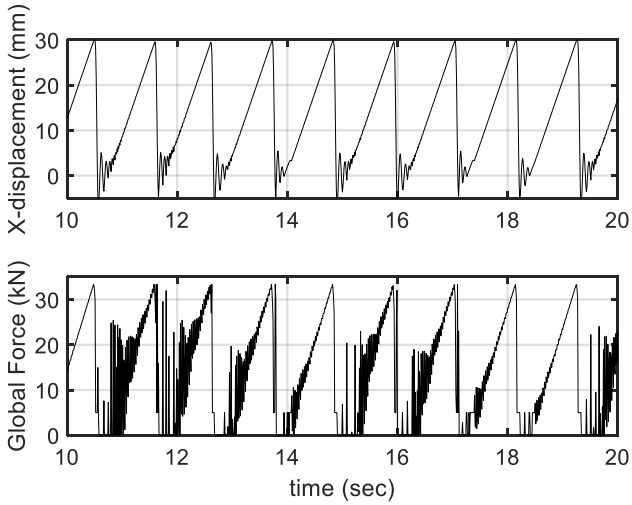

Figure 7. Time-history of interaction force and structural deflection by the numerical simulation

** Figure 6 is reprinted with permission from "Crushing failure during ice–structure interaction" by Sodhi, 2001. Engineering fracture mechanics, 68(17-18), 1889-1921., Copyright [2001] by Elsevier

In comparison between the experiment and numerical simulation (see Figure 6 and Figure 7), the interaction force and structural deflections are generally well matched, with a typical “saw-tooth” pattern in the time history. The structure shows the quasi-static response by following the ice force trend. The structure is deflected with an increasing ice load. After the ice force reaches the peak value, the structure moves forward with a high velocity. The magnitude of the maximum ice force in the numerical simulation is about 32 kN, which is identical to that in the experiment. The ice force frequency in both numerical simulations and explements is in good agreement.

2.5 Case Study for the Offshore 5-MW monopile wind turbine

2.5.1 Wind Turbine Specifications and Environmental Conditions

To assess the overall performance of the wind turbine, the NREL offshore 5 MW baseline monopile wind turbine is selected as an example. The wind turbine properties are tabulated in Table 1. Since the tower base and monopile diameter are the same, at 6 m, the constant value of 6 m is chosen as a structure width for the ice-structure interaction. The total length of the monopile is 56 m below MSL. The water depth is assumed to be 20 m, and 36 m of the monopile is extended below the mudline.

Table 2. Wind turbine characteristics

Parameter	Value	Unit
Rated power	5	MW
Cut-in, rated, cut-out wind speed	3, 11.4, 25	m/s
Tower top height above MSL	87.6	m
Tower base, top diameter	6, 3.87	m
Pile length below MSL, diameter	56, 6	m
Rotor/hub diameter	126, 3	m
Tower top, total mass	350, 1219	T
Water depth	20	m

Natural frequencies of the tower and blades are calculated by using the FEM program, BModes. The added mass per unit length is properly distributed. The soil-monopile interaction is modelled by applying the Winkler-type lateral springs distributed along the subsoil portion of the monopile. The stiffness constants of the distributed springs are dependent on the depth and are equivalent to the foundation properties. After calculating the natural modes of the tower, the tower 1^{st} and 2^{nd} mode shapes in Fore-aft and Side-and-side directions are inputted into FAST (see Figure 8). The 1^{st} and 2^{nd} blade mode shapes in the flapwise direction and 1^{st} in the edgewise direction are inputted in the same manner. The corresponding natural frequencies of each mode are listed in Table 3.

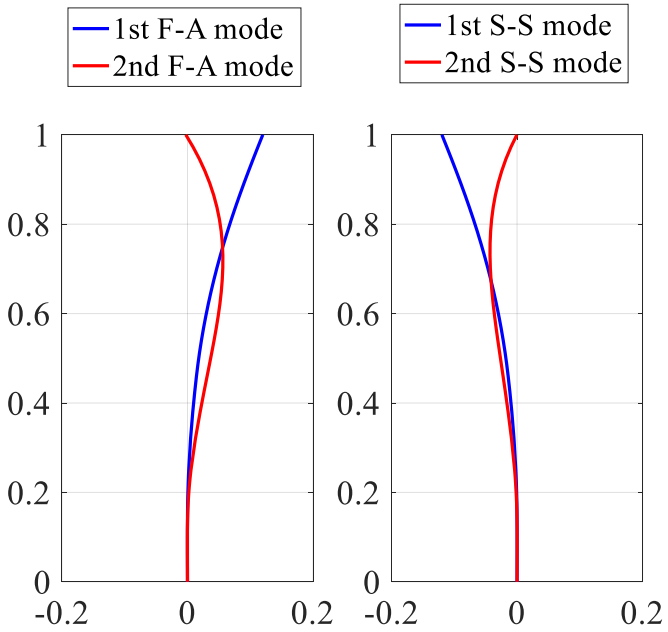

Figure 8. Normalized mode shapes of tower fore-aft and side-to-side

Table 3. Tower and blade natural frequencies

Parameter	Natural frequency (rad/sec)
1st Tower F-A mode	1.548
1st Tower S-S mode	1.538
2nd Tower F-A mode	9.493
2nd Tower S-S mode	8.528
1st Blade flapwise mode	4.394
2nd Blade flapwise mode	12.695
1st Blade edgewise mode	6.781

The ice properties are tabulated in Table 4. The crushing strength varies in a range of 3.0~4.6 MPa according to the strain rate. The international standard, ISO 19906, states that the representative ice modulus for design ranges from 2 GPa to 6 GPa. For the

simulations, the average value of 4 GPa is selected. The ice thicknesses of 0.5 m and 1 m are tested with varying ice speeds. In the current model, K_1 and K_2 depend on the number of zones, and consequently, F_{max} and P_i would be influenced. After a parametric study, the number 100 zones is chosen, which results in a converged value of K_1 and K_2. The comparison between the simulation and model test will be performed in a future study,

Table 4. Ice properties

Parameter	Value	Unit
Crushing strength	3~4.6	MPa
Young's modulus	4	GPa
Ice sheet thickness	0.5	m
Ice drifting velocity	0.005~0.5	m/s
Number of zones	100	

2.5.2 Tower motion in parked conditions

In the parked condition, the interaction of the ice and tower has three distinct modes (intermittent ice crushing, frequency lock-in, and continuous brittle crushing) depending on the ice drifting velocity. The maximum and average global forces in the low speed tests are greater than those of the high-speed tests due to the simultaneous failure as well as the high crushing strength. The statistic values are given in Table 5.

Table 5. Statistics of F-A tower displacement at MSL and Global ice force

	v_ice=0.005 m/s		v_ice=0.05 m/s		v_ice=0.5 m/s	
	Dis. (m)	Force (MN)	Dis. (m)	Force (MN)	Dis. (m)	Force (MN)
max	0.148	10.071	0.082	4.158	0.044	4.033
min	-0.024	0.000	0.004	0.944	0.043	2.286
mean	0.059	3.850	0.043	2.684	0.044	3.055
std	0.040	2.729	0.018	0.542	0.000	0.412

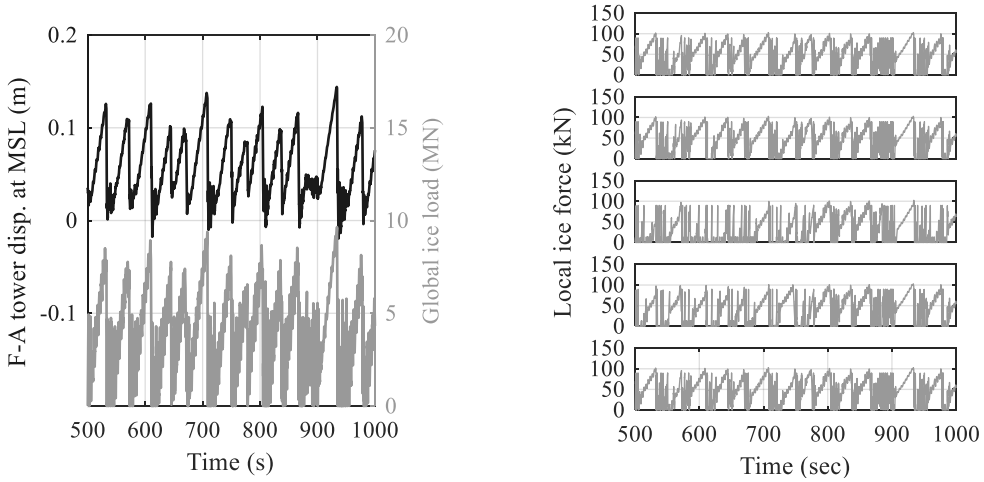

Figure 9. Time-series of F-A tower displacement at MSL and global & local ice load of randomly selected 5 zones out of 100 zones at v_ice=0.005m/s

At low velocity, the ductile failure of intermittent ice crushing occurs and a quasi-static response is indicated. The period of the tower response is the same as that of the ice load. As shown in Figure 9, the ice force has a repeated load signal with a saw-tooth pattern. When the tower moves in the same direction as the ice, the displacement gradually increases with the increasing force. Once the ice force reaches its critical value, the global force rapidly drops and the tower moves forward at a high velocity. During this swing-

back process, the local zones experience multiple local failures. Thus, the contacts of zones become uniform even though the initial contact with the zones are randomly set up. The local force signals of the discrete zones are shown in phase and the ice fails at the same time, even though the ice in the discrete zones interacts individually.

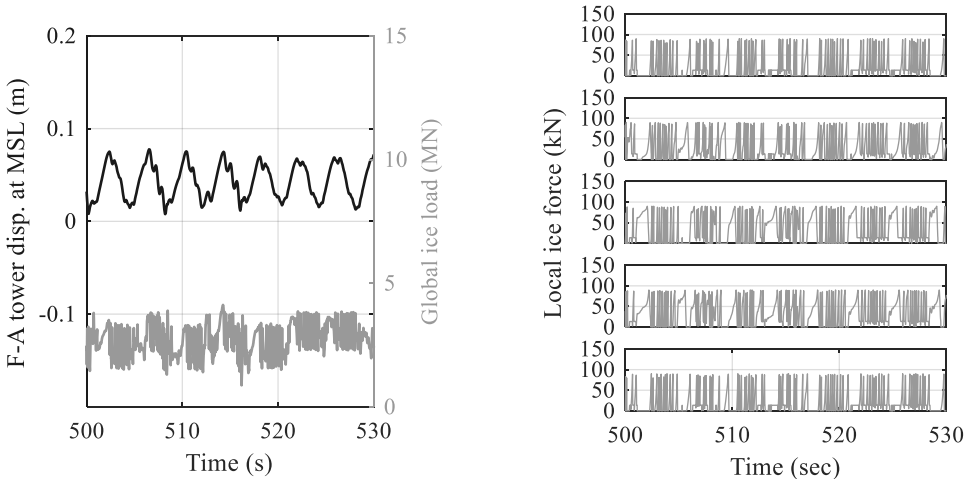

Figure 10. Time-series of F-A tower displacement at MSL and global & local ice load of 5 randomly selected zones out of 100 zones at v_ice=0.05m/s

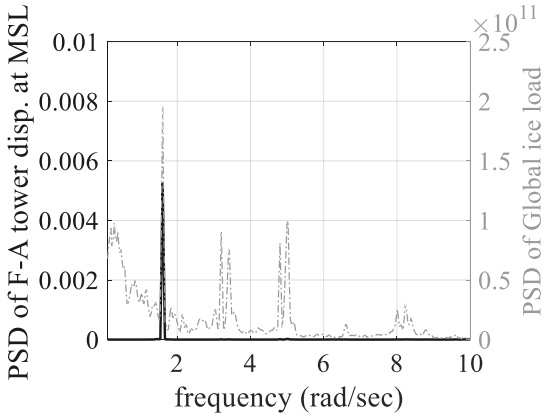

Figure 11. PSD of F-A tower displacement at MSL and global ice load at v_ice=0.05m/s

Figure 10 indicates that the tower motion has steady-state vibration and oscillates with the constant period and amplitude. The PSD plot in Figure 11 shows that the highest peak of the tower motion coincides with that of ice force. They are very close to the tower's natural frequency of 1.55 rad/sec, which indicates the resonance vibration. According to data of the local zone, some zones fail simultaneously around the interface of the contact area, whereas some zones fail non-simultaneously. The multiple simulation runs reveal that the frequency lock-in mode occurs in the range of the ice drifting velocity, from approximately 0.03 m/s to 0.05m/s.

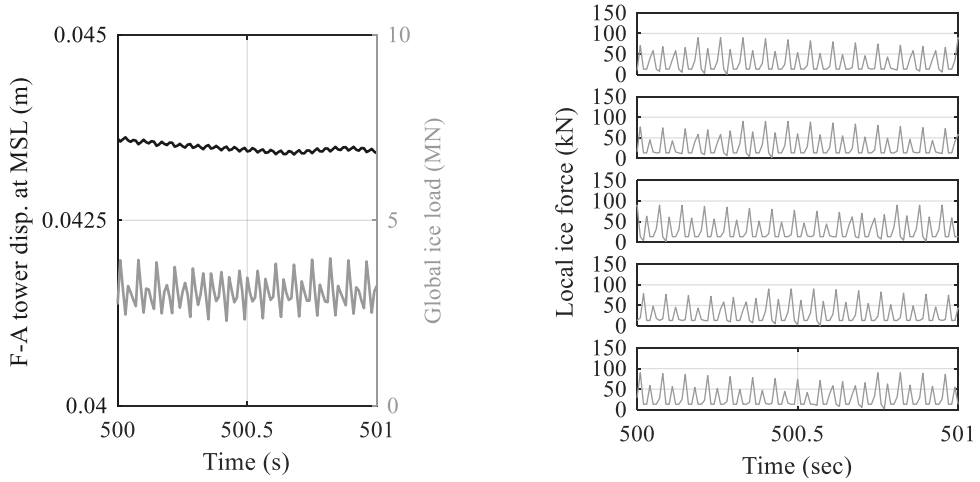

Figure 12. Time-series of F-A tower displacement at MSL and global and local ice load of 5 randomly selected zones out of 100 zones at v_ice=0.5m/s

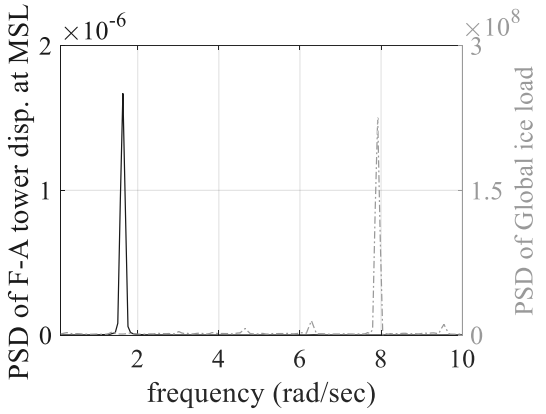

Figure 13. PSD of F-A tower displacement at MSL and global ice load at v_ice=0.5m/s

Continuous brittle crushing is observed in the high velocity region, as seen in Figure 12. The global force is relatively lower than those of previous cases because the local zones fail randomly. In addition, the ice force never drops to zero because of the constant contact between ice and the structure during the interaction. As the ice drifting velocity increases, the peak frequency of the ice force in Figure 13 also increases and is far away from the structure's natural frequency, which results in the small tower motion.

2.5.3 Comparison of the tower and blade motions in parked and operating conditions

In two different environmental conditions, the same structural properties are applied under the same ice conditions. In the parked condition, the rotor is fixed and the wind load is not applied. In the operating condition, the rotor rotates by the aerodynamic wind load, and the control system is used to control the blade pitch angle. The mean wind speed is chosen to be slightly greater than the rated speed so the near-constant power can be generated using the blade pitch control. To examine the coupling effect of the wind load on the entire wind turbine system, turbulent wind is generated and inputted into the

numerical simulations. Time-varying turbulent wind velocities in x, y, and z directions are generated using the Kaimal spectrum with the turbulence variables referred by the standard, IEC 61400-3.

Table 6. Turbulent wind conditions

Parameter	Value
Mean speed	12.0 m/s
Standard	IEC 61400-3
Turbulence type	Normal Turbulence Model(NTM)
Turbulence Characteristic	B
Turbulence model	Kaimal Spectrum

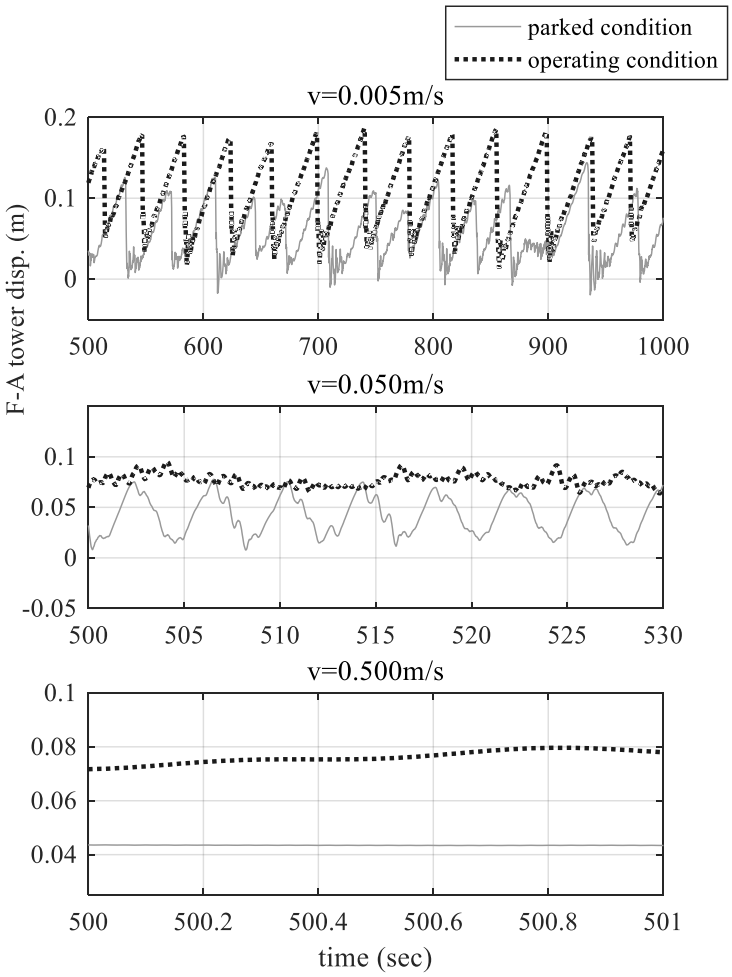

Figure 14. Time-series of F-A tower displacement at MSL in parked and operating conditions

The time-series of F-A tower displacement at MWL are compared in Figure 14. Generally, the trends of the ice load and tower responses at ice drifting speeds of 0.005 m/s and 0.5 m/s are both similar. At the velocity of 0.005m/s, the ice fails in the ductile mode and the tower motion in both cases shows a quasi-static response with the same period of the ice force. At the speed of 0.5 m/s, both cases show very small motion with the small amplitude. Due to the presence of the wind load, the mean total force acting on

the tower in the operating condition is greater than that in the parked condition, resulting in a large mean tower position. Based on this comparison, the ice load is not significantly influenced by the rotor's rotation at those speed.

It is observed, however, that the tower motion in the operating condition shows a small amplitude motion, whereas that in the parked condition has resonance motion with a large amplitude. This is because the aerodynamic damping induced by the dynamic wind drag force on the blades plays a significant role in the resonance frequency. As a result, the ice-induced dynamic tower motion in the operating condition is significantly damped at the ice velocity of 0.05m/s, compared to the responses in the parked condition. Figure 15 ~ Figure 17 indicate the PSDs of F-A tower displacement with varying ice drift velocity.

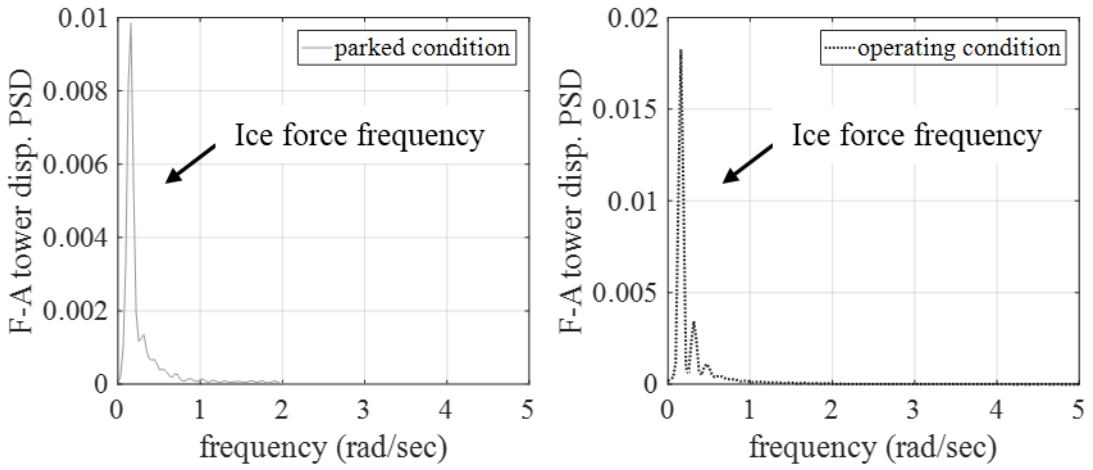

Figure 15. F-A tower displacement PSD comparison at v_ice = 0.005 m/s

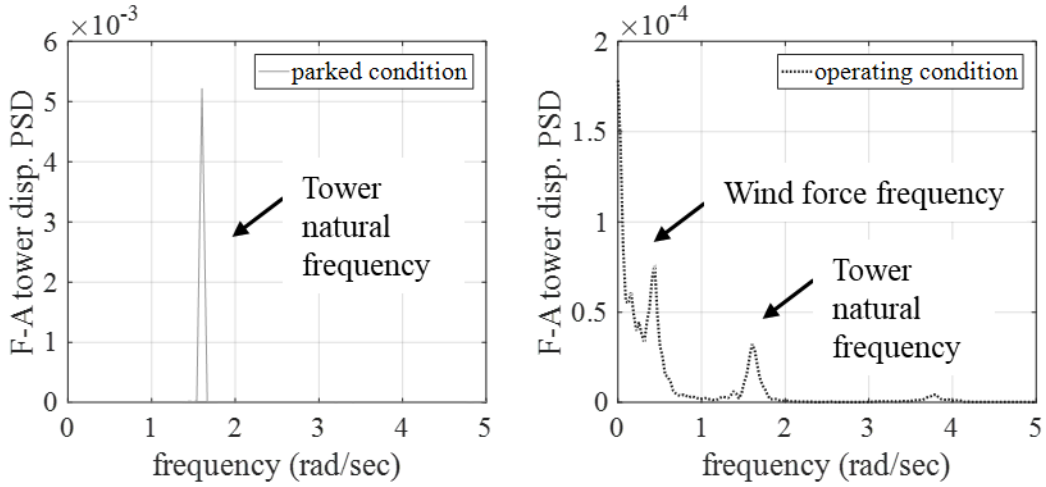

Figure 16. F-A tower displacement PSD comparison at v_ice = 0.05 m/s

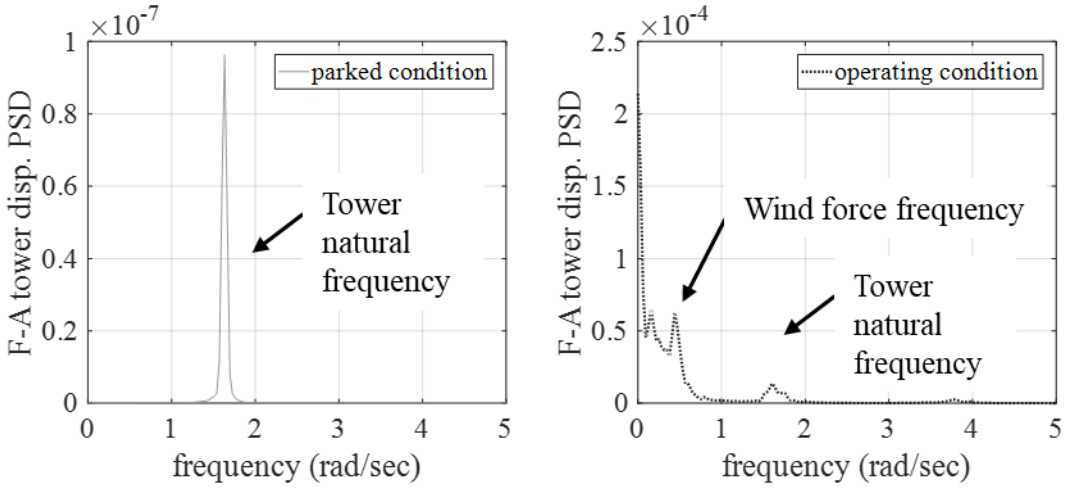

Figure 17. F-A tower displacement PSD comparison at v_ice = 0.5 m/s

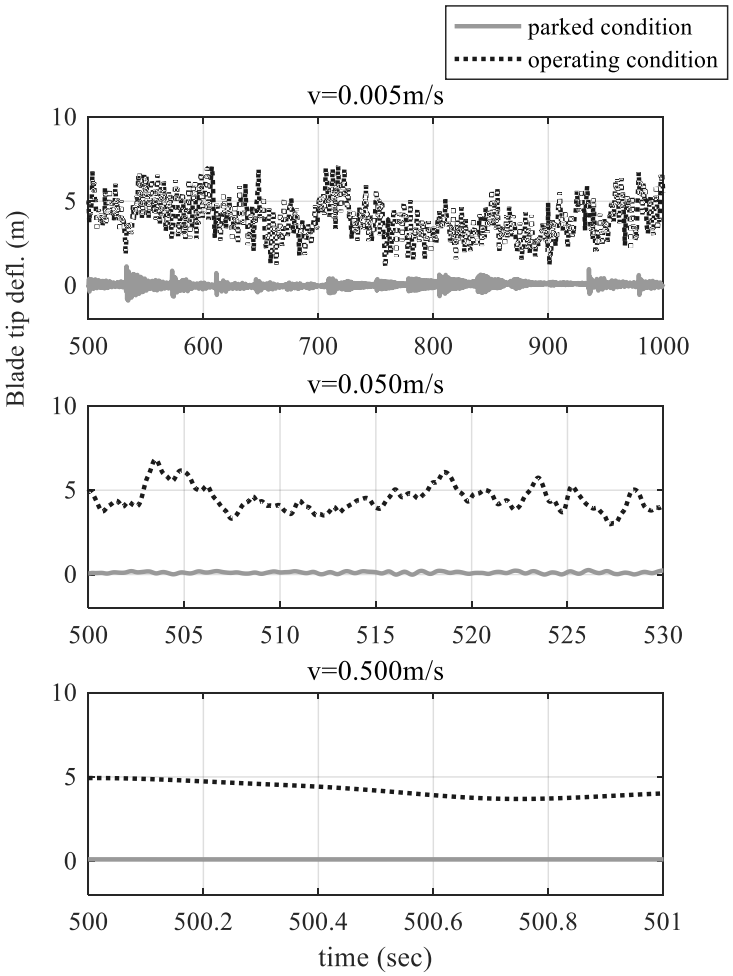

Figure 18. Time-series of blade tip deflection in the flapwise direction

Next, the dynamics of the blade tip deflection in the flapwise direction is investigated. In the parked condition, the blade pitch is fixed at 90 degrees and the power operation is stopped. The rotor rotates slowly in an idling condition. Therefore, the tip deflection is small. In the time-series plots in Figure 18, the spike-like peaks with the same frequency of the ice load are observed at a low ice velocity. These peaks occur when the ice force

reaches its critical value. Due to the sudden drop in force, the entire system of the wind turbine moves at a high velocity, which causes this abrupt motion with the large blade tip deflection. However, as the ice force becomes more random and smaller with increasing velocity, the blade tip does not deflect and no distinct frequency is observed. In the operating condition, the blade tip deflection is generally larger and more dynamic than that in the parked condition. In addition, the influence of ice load is not significant for the dynamics of the blades, because the blades are more dynamically influenced by the rotor speed and low-frequency wind load, as shown in Figure 19 ~ Figure 21.

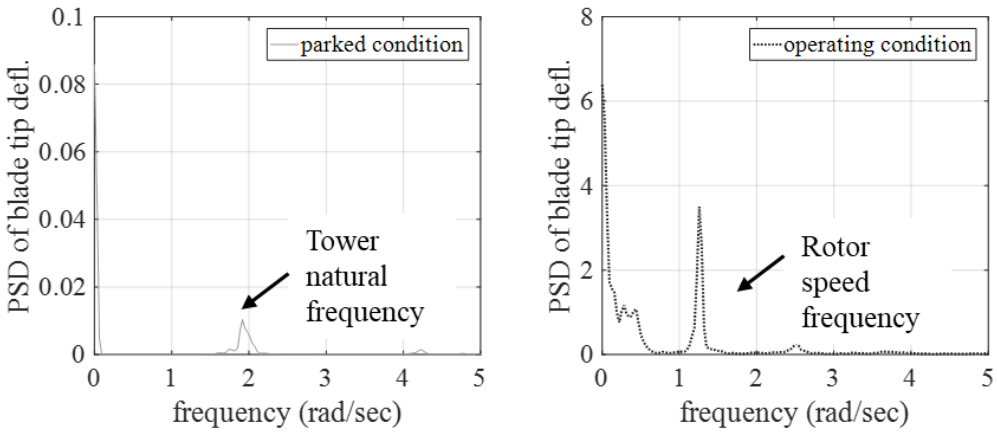

Figure 19. Blade tip displacement PSD comparison at v_ice = 0.005 m/s

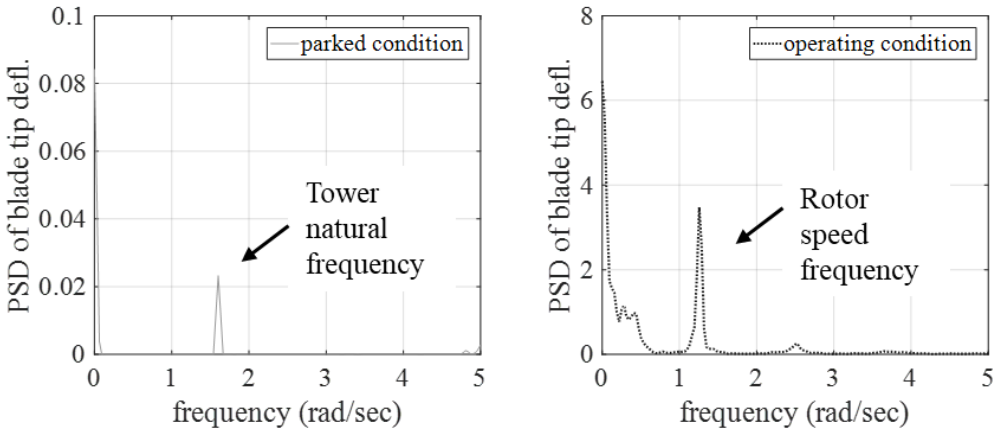

Figure 20. Blade tip displacement PSD comparison at v_ice = 0.05 m/s

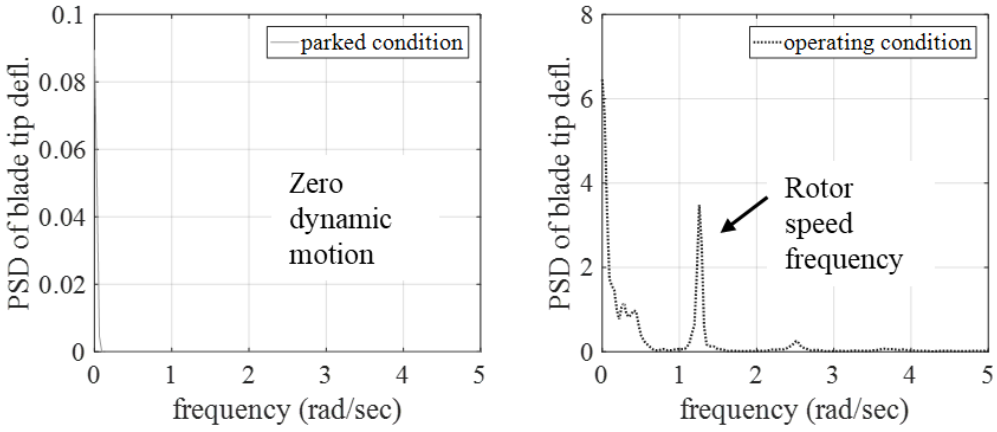

Figure 21. Blade tip displacement PSD comparison at v_ice = 0.5 m/s

2.6 Conclusions

In this study, the ice crushing failure against the cylindrical structures is numerically examined by developing an ice load calculation module, which features a modified Matlock's model with three phases: nonlinear ice stiffness, zonal concept for non-simultaneous failure, and strain-rate-dependent ice crushing strength. This ice module is

inputted into FAST so that a fully coupled aero-servo-hydro-elastic-ice analysis for an offshore wind turbine can be examined. As an example, a monopile type 5 MW offshore wind turbine is selected and investigated with varying ice drifting speeds under parked and operating conditions. The following conclusions are drawn from multiple simulations:

- Due to the nonlinear relation between the strain rate and ice compressive pressure as well as the interaction between the ice and structure, the global mean and maximum ice forces decrease and eventually become a constant value, as the drifting velocity increases.
- Three crushing modes (ductile failure, frequency lock-in, continuous brittle crushing) are well described in the ice breaking model. The time-series of the structure motion is quasi-static and follows the time-series of the ice force at low ice speeds. In the range of ice velocity from 0.03 m/s to 0.05 m/s, the structure shows a large amplitude frequency lock-in mode, and the frequency of the motion is identical to the ice force frequency. At high speeds, ice fails in the brittle mode, and the ice force is random with a small amplitude. As a result, the structure motion is also small.
- The non-simultaneous failure is well-modeled using a zonal concept. At low ice velocities. after the sequence of multiple ice failures, the ice surface of a contact becomes uniform, and the ice failures occur simultaneously, even though the initial contact surface is randomly inputted. However, at high speeds, the local ice fails non-simultaneously, and the global force remains random.
- The transition velocity is observed in accordance with the tower natural frequency. In the current simulation, ice force frequency is locked by the interaction with a wind

turbine at ice a drifting velocity of 0.03~0.05 m/s. Aero damping plays an important role near resonance.

- The trends of the tower dynamics in both parked and operating conditions are similar at low and high ice velocities. Due to the presence of aerodynamic forces, the mean value of tower motion in the operating condition is greater than that in the parked condition. At a high ice drifting velocity, the tower motion is slightly influenced by the rotor rotation in the operating condition, by having slowly-varying motion.
- Aerodynamic damping in the operating condition plays an important role near the resonance frequency. At an ice velocity of 0.05 m/s, the tower shows a frequency lock-in mode in the parked condition. However, the tower motion in the operating condition is damped by the aerodynamic damping induced by the wind drag forces. As a result, the tower shows a smaller motion with a small amplitude than that in the parked condition.
- The blades are mainly influenced by the rotor rotation rather than ice force. In the parked condition, spike-like peaks are observed when the ice force reaches the maximum value. However, the maximum value of the blade tip deflection in the parked condition is still less than that in the operating condition.

CHAPTER III

LEVEL ICE AND FLOATING ARCTIC SPAR INTERACTION INDUCED BY ICE BENDING FAILURE*

3.1 Introduction

When the level ice approaches the downward sloped structure, the interaction has three phases (Aksnes, 2010; Lu et al., 2014; Dalane, 2014): 1) the breaking phase when the ice contacts the structure and is bent by the bending moment, 2) the rotating phase when the broken ice is submerged and rotated underneath the structure, and 3) the sliding phase when the submerged broken ice that is parallel to the sloping structure causes frictional and buoyant forces.

In this study, the beam theory on an elastic foundation is applied for the breaking phase. The given solution by Hetenyi (1946) for the semi-infinite ice-beam model subjected to the vertical and axial compression forces is considered with the geometric relation between the ice and a structure. Until the incoming ice fails in bending against the inclined structure, the governing equation of an elastic beam with the initial boundary condition is solved numerically and the ice tip deflection is calculated according to the

* Part of this chapter is reprinted with permission from "Numerical Simulation of Dynamic Interactions of an Arctic Spar with Drifting Level Ice" by Jang et al., 2016. Intl. J. Ocean Systems Engineering, Copyright [2016] by Techno-Press, Ltd.

solution. Based on the given solution, the moment curve along the entire ice beam is checked to determine whether it exceeds the allowable ice flexural strength. If so, the broken ice length is calculated, and the rotating ice phase is turned on. Since it is assumed that the intact level ice continuously approaches the structure at a constant speed, the broken ice will gradually submerge and rotate downwards. During this process, the viscous drag forces and static pressure due to the ventilation effects are applied to the broken ice as functions of the ice velocity and its position. Therefore, the restoring and exciting forces are solved at every time step using the dynamic governing equation of rotating ice including the ice inertia, to obtain the instantaneous kinematics of the ice block. Once the ice block becomes parallel to the structure, the broken ice slides along the downward sloping structure, causing frictional force, which is basically induced by the buoyancy of the submerged ice. In this stage, it is assumed that after a limited depth, all broken ice is cleared and removed.

Based on the procedural time-dependent ice-load estimation, the result is coupled with the platform motions with the mooring dynamics. By adding the time-dependent ice-loading model to the time-domain simulation program, the dynamic interactions of the drifting level ice with a moored Arctic Spar is solved.

3.2 Literature Review

In the arctic region, a downward sloping structure is beneficial because it makes level ice fail when bending so the global ice load on the structure is reduced. Thus, floating

structures have been designed with a sloped-shape around the mean water level, and experimental tests for the interaction between the level ice and floating sloped structures have been conducted over decades. Comfort et al. (1999) presented a comprehensive summary report based on an extensive set of ice model test data assembled for four different moored floating structures (i.e., Kulluk, semi-submersible, turret-moored drillship, and tanker and loading terminal). They compared the test data under managed ice and level ice sheet conditions. Generally, the mooring force increased with increasing ice thickness and drifting velocity. Bezzubik et al. (2004) presented experimental results on level and ridged ice interactions with a floating Tension-Leg-Platform (TLP). It was intended that ice would be bent and broken downward with two different configurations of a platform. The test results showed good qualitatively and quantitatively agreement with Nevel's theoretical model in terms of ice force statistics and crack patterns. Bruun et al. (2009) presented the ice model-test results of a Spar platform in level ice and ridges, conducted at HSVA. They concluded that a conceptual Spar design for an arctic environment made it feasible to operate in the tested ice conditions, and small platform motions were observed due to a high GM and large displacement.

Similar to the development of experimental procedures for the floating structure interacting with level ice, an analytical approach has also been developed by many researchers. Mostly, these analytical approaches began with sloped/fixed structures. Nevel (1965) provided a formula to estimate the ice load acting on a structure by solving the semi-infinite plate on an elastic foundation problem. Croasdale (1978) conducted a two-dimensional study about the level ice force on a sloping structure while assuming that

level ice behaves like a beam on an elastic foundation, and extended this formula for a conical structure with a width that was equal to the distance along the anticipated circumferential crack. Ralston (1980) also estimated the global level ice force on a conical structure using a plastic limit analysis. He derived the formula including contributions from radial and circumferential cracks, foundation reaction, deforming region, ride-up component, and frictional dissipation.

Based on insights from these previous ice load formulas for sloped/fixed structures, some researchers have applied the analytical methods to floating structures. Aksnes (2010) studied the interaction of moored ships in level ice numerically. He simply assumed the interaction consisted of three different phases (i.e., breaking, rotating, sliding). Through his numerical simulation, the parameter sensitivity study of mooring behavior cases investigated the importance of various parameters. He concluded that the dynamic behavior of moorings was dominated by the vessel's natural period and mass as well as the ice drift speed.

Wille et al. (2011) presented a numerical simulation of a moored downward conical structure in level ice. They considered two phases during the interactions. For the first phase, the interaction force from semi-infinite ice moving at a constant speed was considered based on the beam theory. In the second phase, the rotation of the broken ice around the edge of the intact ice sheet was modeled. They indicated that the influence of the mass and damping of ice was not significant since the bending failure process can be considered quasi-static. In addition, the ice load was quasi-periodic resulting in a quasi-harmonic response of a moored floating structure.

Dalane (2014) performed both an experimental and numerical study for a conical floating structure in level ice. He focused more on the pitch motion of a floating structure by comparing it to that of a fixed structure. From the test data, the measured ice force of a compliant structure was reduced by about 12~18% compared to a fixed structure due to the inclination angle change and non-simultaneous failure. He also indicated that the structural response affected the ice loading process, which is important for moored floating structures. **Numerical Approach**

3.3.1 Ice breaking phase

According to ISO 19906, level ice can be defined as sea ice with un-deformed upper and lower surfaces. In order for offshore structures to resist the level ice load, the inclined wall was proposed to induce level failure against bending. If the ice floe is long and slender enough and is subjected to the reaction forces at the edge, then the ice will fail when the tensile stress of an upper surface reaches the ice flexural stress.

A semi-infinite beam theory on elastic foundation is employed to verify this assumption. A beam equation on the elastic foundation is used with variables for the vertical load, F_{BV} and horizontal load, F_{BH} on the contact area between the ice and structure.

$$EI\frac{d^4v}{dx^4} + F_{BH}\frac{d^2v}{dx^2} + \rho_w gBv = 0, \qquad x > 0 \tag{7}$$

(a) Reaction forces on Ice (b) Applying force on a sloping structure

Figure 22. Ice breaking procedure

where E is the modulus of elasticity, I is the second moment of area of the ice-beam, ρ is the water density, g is the gravitational acceleration, B is the width of the ice-beam, v is the vertical deflection of ice, and x is the horizontal spatial variable. To obtain the analytical solutions of the governing equation, boundary conditions are introduced. Since the ice is semi-infinite, the deflection and rotation are zero at infinite x. In contrast, the contact point is assumed to be a free end, where the moment is zero and the vertical shear force is the applied force, F_{BV}.

$$\lim_{x\to-\infty} v(x) = 0,\ \lim_{x\to-\infty} \frac{dv}{dx} = 0,\ \frac{d^2v(0)}{dx^2} = 0,\ -EI\frac{d^3v(0)}{dx^3} = -F_{BV} \tag{8}$$

The corresponding solutions given by Hetenyi (1946) are as follows:

$$v(\mathrm{x}) = \frac{F_{BV}}{2EI\,\alpha(3\beta^2-\alpha^2)} e^{-\beta x}(2\alpha\beta\cos\alpha\,\mathrm{x} + (\beta^2-\alpha^2)\sin\alpha\,\mathrm{x})$$

$$M(\mathrm{x}) = -EI\frac{d^2 v(\mathrm{x})}{d\,\mathrm{x}^2} = \frac{-2F_{BV}\lambda^2}{\alpha(3\beta^2-\alpha^2)} e^{-\beta x}\sin\alpha\,\mathrm{x} \tag{9}$$

and

$$\alpha = \sqrt{\lambda^2 + \frac{F_{BH}}{4EI}},\ \beta = \sqrt{\lambda^2 - \frac{F_{BH}}{4EI}},\ \lambda = \sqrt[4]{\frac{\rho_w g B}{4EI}}$$

One can find the relation of the forces by manipulating the geometry and force balance at the contact point, as shown in Figure 22. The reaction forces on ice would balance the normal and fictional forces at the contact point. The ISO standard also uses this vertical and horizontal forces relationship as follows:

$$F_{BH} = \xi \cdot F_{BV}, \qquad \xi = \frac{\sin\theta + \mu\cos\theta}{\cos\theta - \mu\sin\theta} \tag{10}$$

When the drifting ice contacts a sloping structure, the vertical deflection at the contact point can be calculated with the penetrated distance of the level ice into the structure. It can be expressed as $v(0) = (v_{ice} \cdot t - X(t))$, where v_{ice} is the ice drift speed and X is the horizontal contact point coordinate.

Therefore, utilizing all of the conditions and obtaining the analytical solutions, the forces acting on the structure can be computed at each time step. In addition, by checking the maximum moment along the level ice, the tensile stress from the bending and axial loads can be calculated by Eq. (11).

$$\sigma_{ice} = \frac{6M}{Bh_i^2} - \frac{H}{Bh_i} \tag{11}$$

If the maximum stress reaches the flexural strength of ice, the ice is considered to be broken and the ice rotation module is initiated. The ice breaking length, $L_{B,}$ is calculated as the distance from the edge of the ice sheet to the point where the maximum stress occurs.

3.3.2 Ice rotating phase

Once the level ice is broken and the broken ice-block starts to submerge, then the ice impact on a structure is computed in the ice rotation module immediately following the ice breaking module. This module runs until the ice block is parallel to the sloping surface. This process has been described in other papers (Liu et al, 2006 and Lu et al., 2014) stating that the ice block is subjected to the hydrodynamic force that results from viscous drag as well as the static pressure from the ventilation effects. The general process of the rotation of the ice block is illustrated in Figure 23.

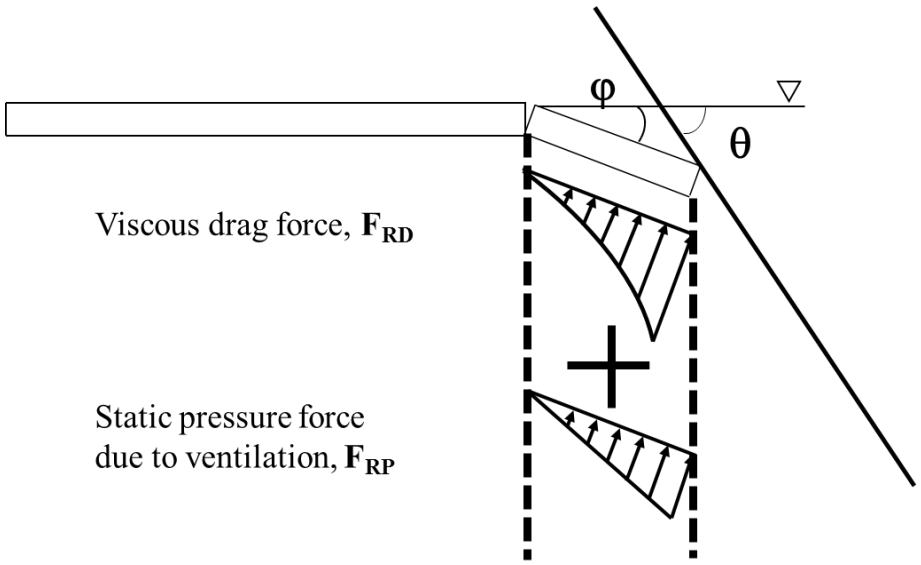

Figure 23. Ice rotating procedure

3.3.2.1 Viscous drag force

During the ice rotation process, the ice block is assumed to rotate around the rear edge and viscous drag force is applied to the ice block, which can be calculated by Eq. (12).

$$dF_{RD} = \frac{1}{2} \cdot \rho_w \cdot C_d \cdot B \cdot V_x^{\,2} \cdot dx \tag{12}$$

By integrating the breaking length, the viscous drag force acting on the ice block can be represented with the velocity of the front edge of the ice block, V_{LB} , in Eq. (13). From the paper by Kotras (1983), the drag coefficient, C_d, is selected as 1.0.

$$F_{RD} = \frac{1}{6} \cdot \rho_w \cdot C_d \cdot B \cdot V_{L_B}{}^2 \cdot L_B$$
$$V_{L_B} = L_B \cdot \dot{\varphi} \tag{13}$$

3.3.2.2 Static pressure due to ventilation

Static pressure due to ventilation is estimated based on the theories by Lindstrom (1990). Ventilation means that the water on the broken ice top is free from flooding. This factor depends the different conditions such as the size and shape of the broken ice and relative velocity. In this paper, the static pressure is assumed to be applied on the beam linearly underneath the rotating ice block, and it is factored by the coefficient, C_P. The static pressure force is

$$F_{RP} = C_P \cdot B \cdot L_B \cdot \rho_w \cdot g \cdot H_s \tag{14}$$

where $B \cdot L_B$ is the area of the ice block, H_s is the depth of the whole turning ice block, and C_p is a coefficient determined by the experimental or measured field data. In this simulation, the coefficient, Cp, is selected to be zero, because the structure is a floating type, and the level ice moves slowly.

3.3.2.3 Rotating ice dynamic equation

For simplicity, we assume the breaking point is a hinge, and thus, we formulate the moment equilibrium for the rotating ice with reaction forces, F_{RH} and F_{RV}. Since the

viscous drag and static pressure forces are proportional to the first and third power of the breaking length, the moment arm can be obtained as 2/3 and 4/5, respectively. Since the broken ice is rigid, the angle between the broken ice and the mean water level as well as the kinematics can be obtained by constructing the geometry relations.

$$\sum M_{hinge}: \quad (1+C_{added})(\frac{1}{12}\rho_i BL_B h_i {L_B}^2 + \frac{1}{4}\rho_i BL_B h_i {L_B}^2)\ddot{\varphi} + \frac{1}{2}L_B(\rho_w - \rho_i)BL_B h_i g\cos\varphi = L_B(F_{RV}\cos\varphi + F_{RH}\sin\varphi) - L_R(\frac{2}{3}F_{RP} + \frac{4}{5}F_{RD}) \quad (15)$$

The added mass coefficient for the rotating motion of the broken ice around one edge is calculated based on the potential theory. Through pre-processing, the added moment of inertia is obtained in the discretised length and interpolated for the corresponding breaking length. With the obtained reaction forces, the moment distribution along the broken ice length is checked for a secondary ice-breaking occurrence to determine whether it exceeds the maximum moment corresponding to the ice flexural strength. After the second breaking, the broken ice is considered to resist the bending and can rotate as a rigid piece.

3.3.3 Ice sliding phase

In the ice sliding phase, the frictional force is caused by the ice buoyancy forces and ice sliding. The buoyancy force is

$$F_{SS} = (\rho_w - \rho_i) \cdot g \cdot B \cdot h_i \cdot \frac{Z}{\sin\theta} \tag{16}$$

where Z is the water depth of the sliding ice. Moored structures in the arctic region are more likely to have a sloped wall and push ice sideway. Therefore, a limited amount of ice would slide under the structure up to the limited depth Z. Barker et al. (2012, 2015) emphasized the importance of Z, stating that the ride-up height influences the magnitude of the global ice action. For example, Mayne and Brown. (2000) observed the rubble pile heights of the Confederation Bridge and found that it depended on the ice thickness as a power law form in Eq. (17). Although there is an upward slope, we directly adopt the equation in this simulation.

$$Z = 7.6 h_{ice}^{\ 0.64} \tag{17}$$

By manipulating the force relationship, as shown in Figure 22, the horizontal and vertical ice forces acting on the structure can be calculated as follows:

- Reaction forces

$$\begin{cases} F_{SN} = F_{SS}\cos\theta \\ F_{ST} = \mu F_{SN} \end{cases} \tag{18}$$

- Forces applied to the structure

$$\begin{cases} F_{SH} = F_{ST}\cos\theta + F_{SN}\sin\theta \\ \quad = (\rho_w - \rho_i)\cdot g\cdot B\cdot h_i\cdot Z\cdot\cot\theta\cdot(\mu\cos\theta+\sin\theta) \\ F_{SV} = F_{SN}\cos\theta - F_{ST}\sin\theta \\ \quad = (\rho_w - \rho_i)\cdot g\cdot B\cdot h_i\dfrac{Z}{\sin\theta}\cdot(\cos^2\theta - \mu\cos\theta\sin\theta) \end{cases} \tag{19}$$

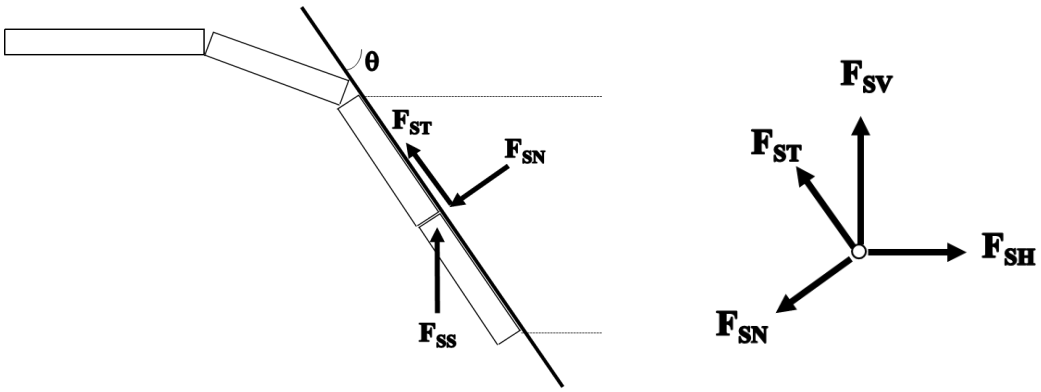

(a) Schematic view of the ice sliding phase (b) Force balance at contact point

Figure 24. Ice sliding procedure

3.3.4 Coupled dynamic simulation considering the ice-structure interaction

The current development is achieved by extending the existing hull-riser-mooring coupled dynamic program, CHARM3D. The program is to analyze the ice-structure interaction for floating moored structures in time domain, including hydrodynamic effects. The governing equation for the floating structure is

$$(M + M_{Add}(\infty))\ddot{x} + B_R\dot{x} + B_{vis}\left|\dot{x} - v\right|(\dot{x} - v) + (K_{mooring} + K_{hydro})x = F_{mooring} + F_{Brk} + F_{Rot} + F_{Sld} \quad (20)$$

where M is the mass of a structure, M_{add} is the added mass, B_R is the radiation damping coefficient, B_{vis} is the viscous damping coefficient, $K_{mooring}$ is the stiffness from mooring lines, K_{hydro} is the hydrostatic stiffness, $F_{mooring}$ is the mooring tension force, F_{Brk}, F_{Rot}, and F_{Sld} are ice induced forces by breaking, rotating, and sliding, respectively.

Based on the original CHARM3D program, the ice load calculation module is added to calculate the external ice forces. Figure 25 shows the flow chart of the CHARM3D ice module. With multiple input information, this simulator can provide additional output of the results of the ice load time-series for each phase, ice breaking length, and the broken ice kinematics.

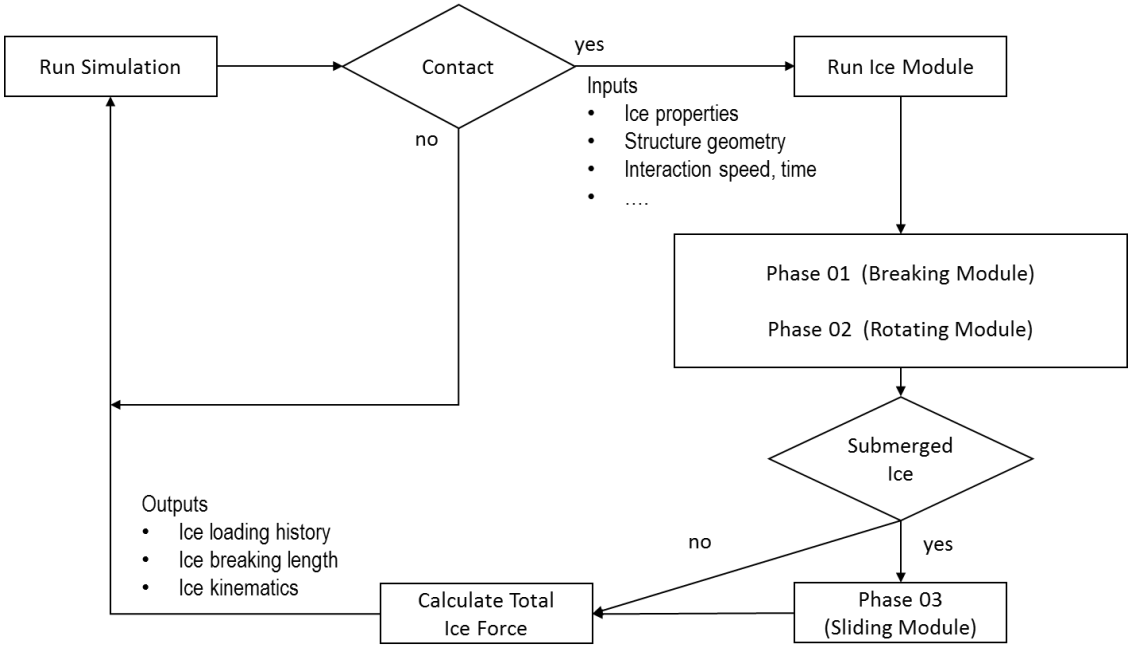

Figure 25. Flow chart for ice interaction

3.4 Numerical Model Description

For a case study, we design a generic model of a Spar-type floating structure with 14 mooring lines. In order to minimize the 3D-effect, the structure is modelled with a square cross-section as well as a flat inclined wall. The downward inclined angle is 45 degrees so the ice could fail from bending. Since the structure is a floating-type, the inclined wall angle with respect to the waterline can vary in time with pitch motions, affecting the calculation of the ice load.

Table 7. Structure properties

Parameter	unit	Value
Displacement	MT	2129860
Width at MWL	m	40
Draft	m	182
Slope angle at MWL	deg.	45
Number of mooring lines	ea	14
COG below MWL	m	102.4
COB below MWL	m	99.5
Roll, Pitch Radius Gyration	m	122.6
Yaw Radius Gyration	m	8.7
Water Depth	m	914.4

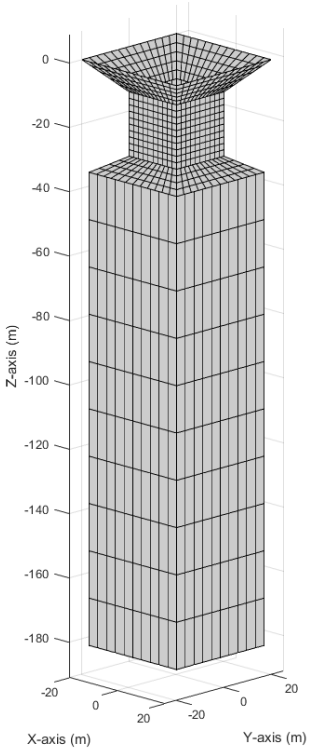

(a) Floating structure

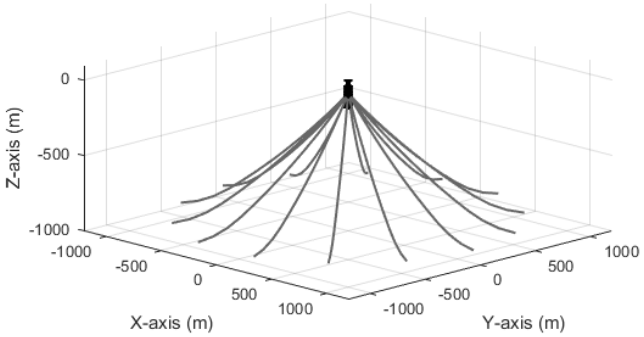

(b) Entire system configuration

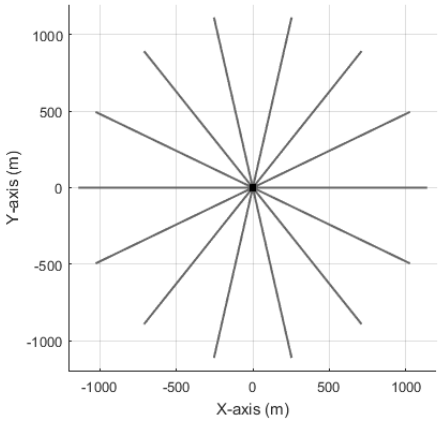

(c) Mooring line configuration

Figure 26. Moored floating structure system model

Table 8. Mooring properties

Type		Unit	Value
No. Mooring lines		ea	14
Chain	Dry/wet weight	N/m	370.93 / 322.71
	Axial stiffness	kN	1.328E+06
	added mass	N/m	48.22

Table 8. Continued

	Type	Unit	Value
Wire	Dry/wet weight	N/m	99.10 / 19.79
	Axial stiffness	kN	1.628E+06
	Added mass	N/m	19.79
	Unstretched length	m	1402.98

3.4.1 Hydrodynamic coefficient

The hydrodynamic coefficients including added mass and radiation damping were calculated from the 3D panel-based radiation program. The spar model was modeled with 1352 panels and analyzed at 42 wave frequency in the frequency domain. The hydrodynamic coefficients of added mass and radiation damping are presented in Figure 27 and Figure 28.

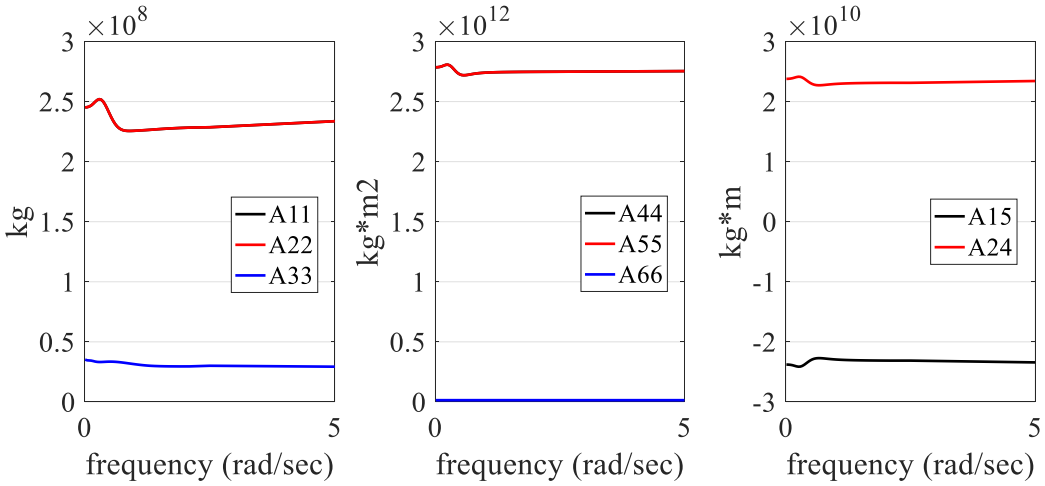

Figure 27. Dimensional added mass coefficients
(1: surge, 2: sway, 3: heave, 4: roll, 5: pitch, 6: yaw)

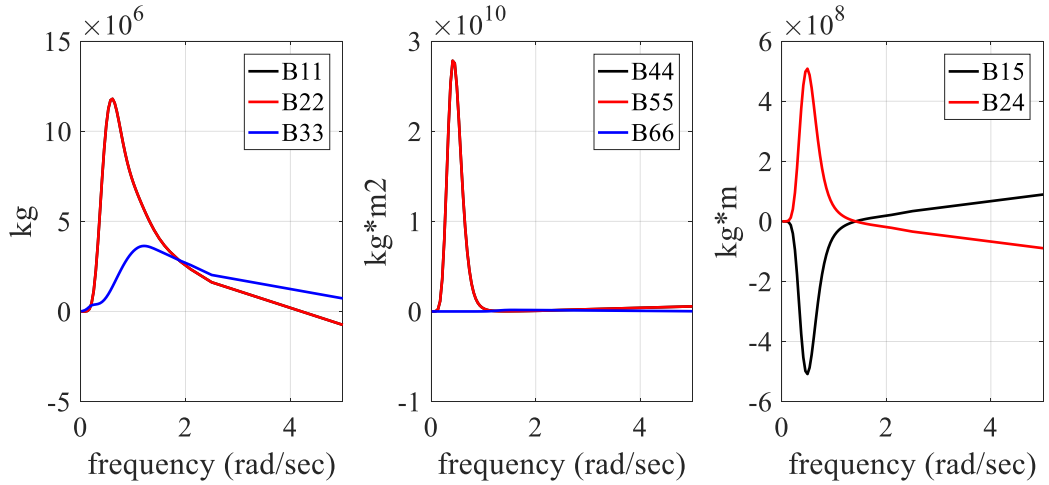

Figure 28. Dimensional radiation damping coefficients
(1: surge, 2: sway, 3: heave, 4: roll, 5: pitch, 6: yaw)

3.4.2 Free-decay test

The free-decay test was conducted to identify the entire system. A drag coefficient of 1.5 was selected for the square type column. Since the platform is symmetric in the x and y directions, the surge, heave, and pitch free-decay tests were conducted with initial displacements of 11.2 m, -1.64 m, and 0.2 rad., respectively. The natural frequencies of the entire system are tabulated in Table 9.

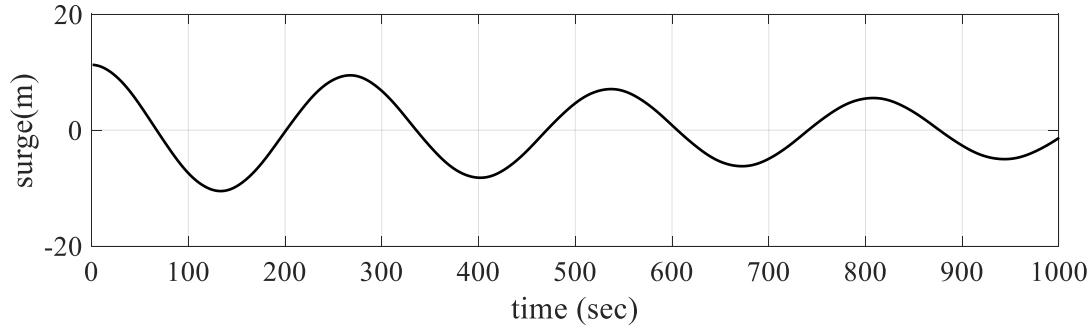

Figure 29. Surge free-decay test

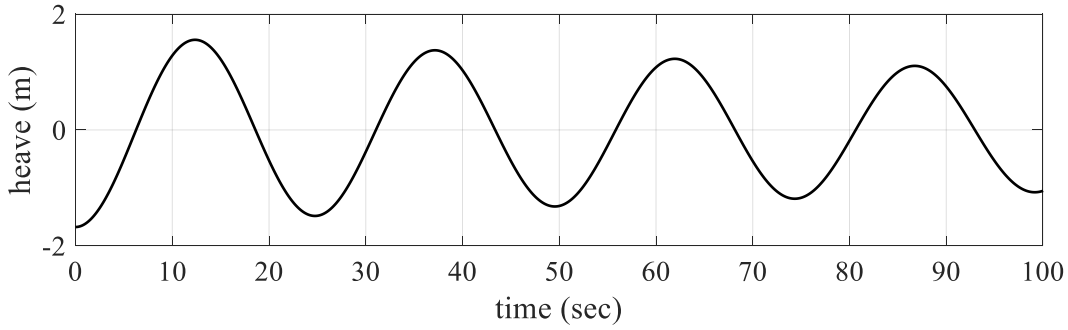

Figure 30. Heave free-decay test

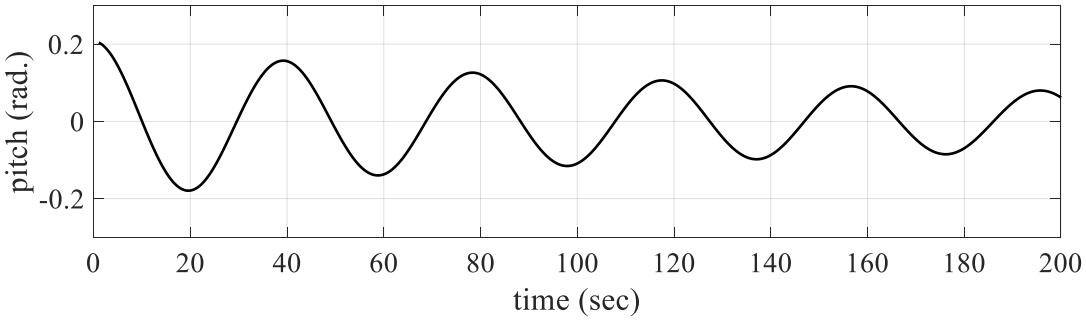

Figure 31. Pitch free-decay test

Table 9. Arctic Spar natural frequencies

	Period (sec)	Frequency (rad/sec)
Surge	272.3	0.0231
Heave	24.7	0.2513
Pitch	39.0	0.1571

3.4.3 Ice properties

The ice properties for the calculation of impact loading are tabulated in Table 10. According to ISO 19906, the range of the sea ice density is from 720 kg/m^3 to 920 kg/m^3 and above the waterline, and the density ranges from 840 kg/m^3 to 910kg/m^3 for first-year ice. Therefore, the density of 900 kg/m^3 was selected for the level ice in this simulation.

The downward breaking flexural strength for winter has typical values of 0.3 MPa to 0.5 MPa, whereas 0.2 MPa is typical for warmer conditions. Thus, the elastic modulus of 4 GPa was selected considering that those of design ice actions in natural ice sheets range between 2 GPa and 6 GPa.

Table 10. Level ice properties

Parameter	Value	unit
Flexural strength, σ_f	500	kPa
Ice thickness, h_i	2	m
Young's modulus, E	4	GPa
Friction coefficient, μ	0.1	-
Ice density, ρ_i	900	Kg/m^3

As a pre-processing step, the coefficient for the ice added moment of inertia was calculated with a potential theory. The rectangular shape with a width of 40m was considered. In the simulation, the coefficients for various ice thicknesses and breaking lengths were obtained. The interpolated values are shown in Figure 32.

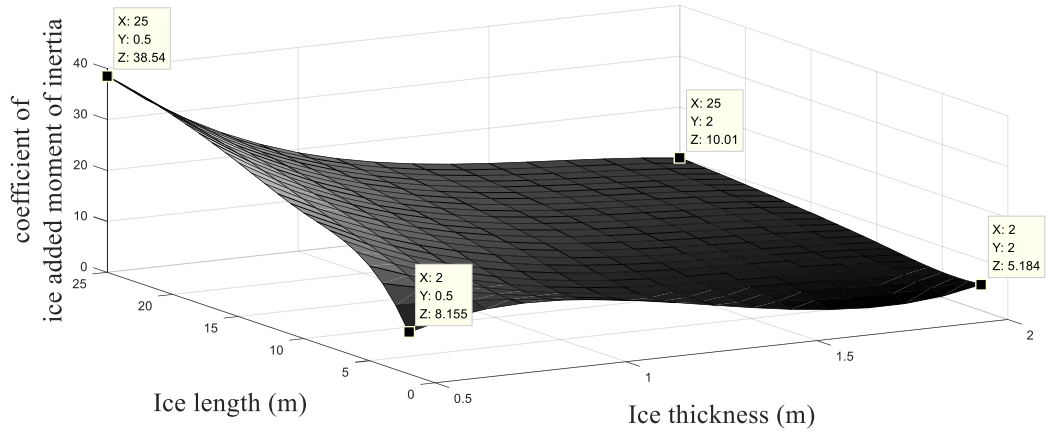

Figure 32. Ice added moment of inertia coefficient

3.5 Numerical Simulation Results and Discussions

3.5.1 Total ice load estimation

The total ice load in the 3-hour simulation shows a repeating pattern of load signals over a certain period. This period is determined by the breaking length and the drifting speed of the level ice as well as the interaction with the structure. With the given ice properties, level ice is very stiff, and thus it is broken in a very short time despite the small tip defection. The breaking force is a function of the sloped angle of the structure, which slightly varies in time due to the small pitch motions. After breaking, the broken ice rotates downward along the inclined structure surface. In the rotating phase, the simulation shows a peak at first and then the magnitude monotonically decreases until there is another peak from the initial contact (breaking phase) of the second broken ice sheet. The results reveal that the second breaking occurs immediately after the first breaking due to the large reaction forces at the contact point. Once the ice breaks into two parts, it rotates

sequentially until each piece is parallel to the structure. The rotating ice force in the surge direction decreases with an increased angle over time. The reduction of the angular velocity also contributes to the reduction of the drag-induced surge force. When the broken ice is parallel with the surface, there is a maximum buoyancy-induced contact force that corresponds to the peak of the sliding force.

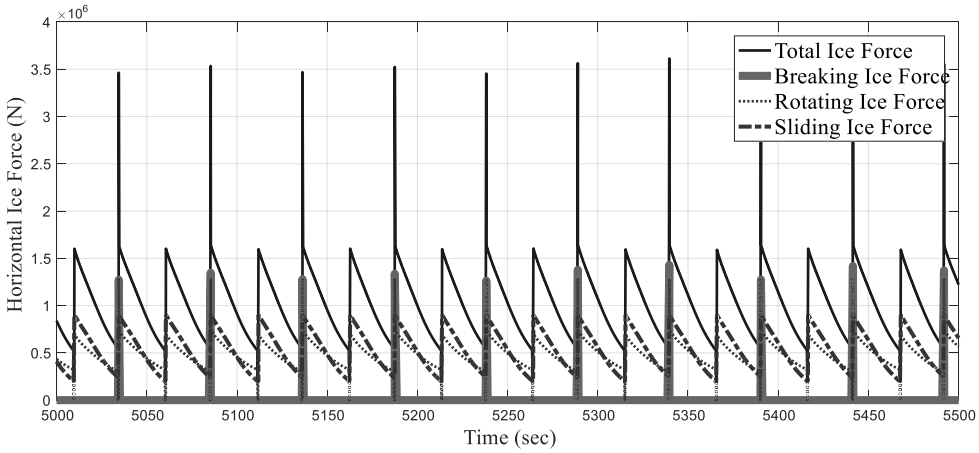

Figure 33. Ice load components in time domain with secondary breaking (h_{ice}=2m, v_{ice}=0.5m/s)

For comparison, two other methods are also selected. Croasdale (1978) initially considered a two-dimensional upward-slope fixed structure for level ice impact using the beam equation on the elastic foundation for the breaking force. He added the force contribution to push up the broken ice. Croasdale et al. (1994) further developed the equations including rubble effects. For the downward-slope floating structure, we assume that the rubble effects are negligible since a moored platform is moveable, which was also seen in Bruun el al. (2009). Thus, we considered only two components of the breaking

and ride-down force. By replacing the ice density with the difference of water and ice densities, the level ice force for a downward-sloping structure can be calculated as follows;

$$F_{horizontal} = 0.68B\sigma_f \sqrt[4]{\frac{\rho_w g h_i^5}{E}} \frac{\sin\theta + \mu\cos\theta}{\cos\theta - \mu\sin\theta} + BZh_i(\rho_w - \rho_{ice})g\left(\frac{(\sin\theta + \mu\cos\theta)^2}{\cos\theta - \mu\sin\theta} + \frac{\sin\theta + \mu\cos\theta}{\tan\theta}\right) \quad (21)$$

Ralston (1980) also studied the level ice impact acting on a conical structure. He derived the formula with contributions from radial and circumferential cracks, foundation reaction, deforming region, ride-up component and frictional dissipation. The details of the theory and equations are given in Ralston (1980). For comparison, the formulas given by the ISO standard are used with the Tresca yielding condition.

Since these two methods do not account for the ice-velocity effects, the simulated results are calculated with the ice drift speed of 0.5 m/s for comparison. In all cases, the ice load increases with increasing ice thickness. In this example, the simulation results are closer to those of the Croasdale method.

Table 11. Global ice load comparison

Ice Thickness (m)	0.5	0.8	1.0	1.3	1.5	1.8	2.0
Ralston (MN)	0.666	1.487	2.184	3.444	4.421	5.506	7.328
Croasdale (MN)	0.485	0.948	1.306	1.910	2.352	2.823	3.582
Simulation (MN)	0.475	0.938	1.304	1.927	2.400	3.139	3.689

The simulation results reveal that the breaking and sliding forces increase linearly with the ice thickness because these forces are proportional to the ice stiffness and volume. The rotating ice force also increases as the ice thickness become larger. The thicker level ice results in a longer ice breaking length which causes larger fluid interaction forces. In this simulation, the ventilation effect is neglected, assuming that the water would fill back in immediately after the ice rotation. It is also assumed that the width of the level ice pushing the platform is the same as the column width, which may be the case when cracks occur at both edges of the square column.

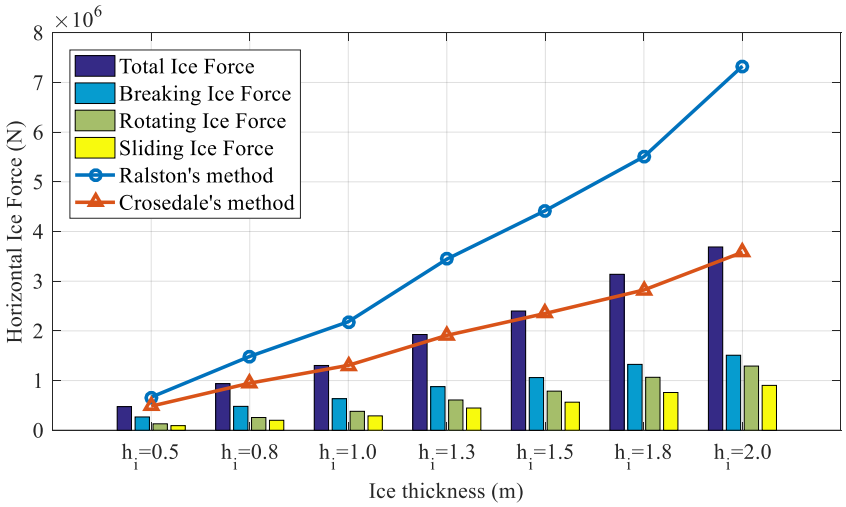

Figure 34. Ice force contribution of each phase with varying ice thickness (Maximum values)

3.5.2 Discussion about the breaking phase

In this simulation, the beam equation with axial and vertical loads on an elastic foundation are used (e.g., Hetenyi, 1946). For comparison, various cases under different conditions were investigated: 1) semi-infinite beam equation subjected to the vertical load

only, 2) semi-infinite beam equation subjected to both vertical and axial loads, and 3) finite beam equation subjected to the vertical load only. Figure 35 shows the simulation results. As the elastic modulus increases from 2GPa to 8GPa with an increment of ice thickness from 0.2m to 2.0m, having the axial compression component produces slightly higher breaking force. However, consideration of the finite length of level ice does not significantly influence the ice forces as long as the length of the level ice is over 100 m as in this case.

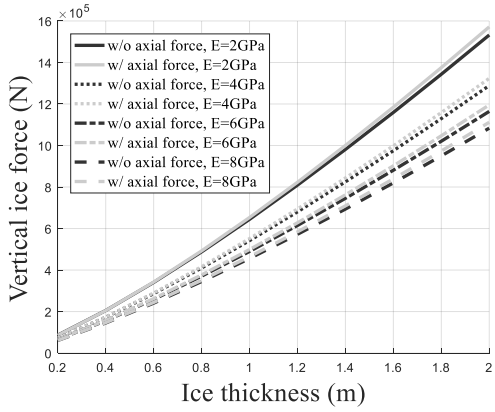

(a) Vertical ice load with thickness by varying elastic modulus

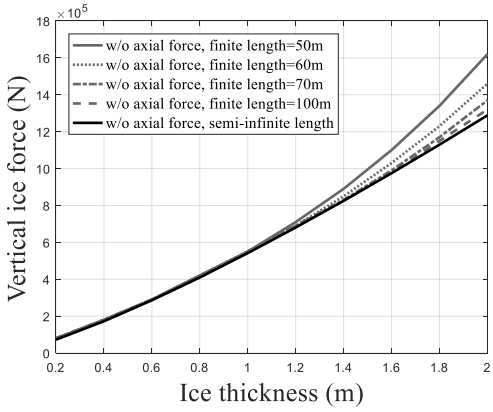

(b) Vertical ice load with thickness by varying finite level ice length

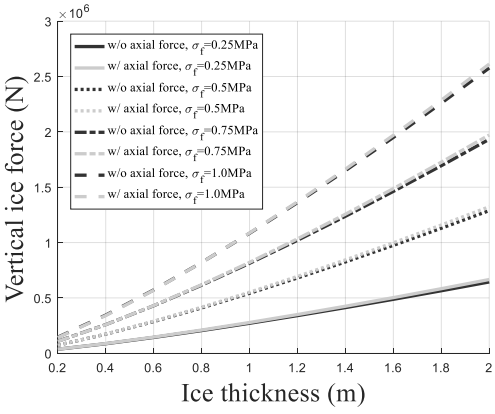

(c) Vertical ice load with thickness by varying flexural strength

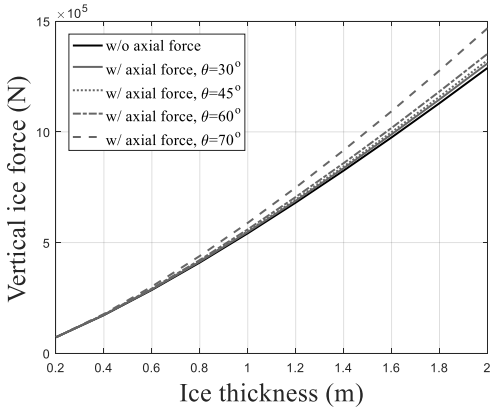

(d) Vertical ice load with thickness by varying inclined angle

Figure 35. Effects of variables on a beam theory

3.5.3 Second breaking scenario in the rotating phase

In the model test conducted by Matsuishi and Ettema. (1985), they observed that the ice interacting with the moored conical structure experienced secondary ice breaking. During the rotating phase in the current simulation model, the possibility of secondary ice breaking is checked by observing the bending moment distribution and local stress along the broken ice. The secondary breaking actually happened immediately after the first breaking (❷). Figure 36 shows the comparison of the numerical results between the cases w/ and w/o secondary breaking. Without secondary breaking, the ice loads monotonically decrease with time within one period. When secondary breaking occurs, there are two peaks in one period (❶). Once the intact ice breaks, the first breaking length of 25m is calculated, with about 12.7 times the ice thickness. The secondary breaking immediately follows the first breaking. The second peak after the half period in this case is due to the initial impact (breaking phase) of the second portion following the frontal part. Since it is assumed that the attachment length of the sliding ice sheets is fixed in the model, the buoyancy induced sliding force caused by the displaced volume of surface-contacting ice sheets starts to decrease with the rotation of the upper ice sheet. In the present modelling of the rotating phase, we neglects the ventilation effects since the upper surface of ice is immediately flooded by sea water. If ventilation effects are taken into consideration in the beginning of rotation, the relevant force is generally large and the pattern of ice loading can be quite different.

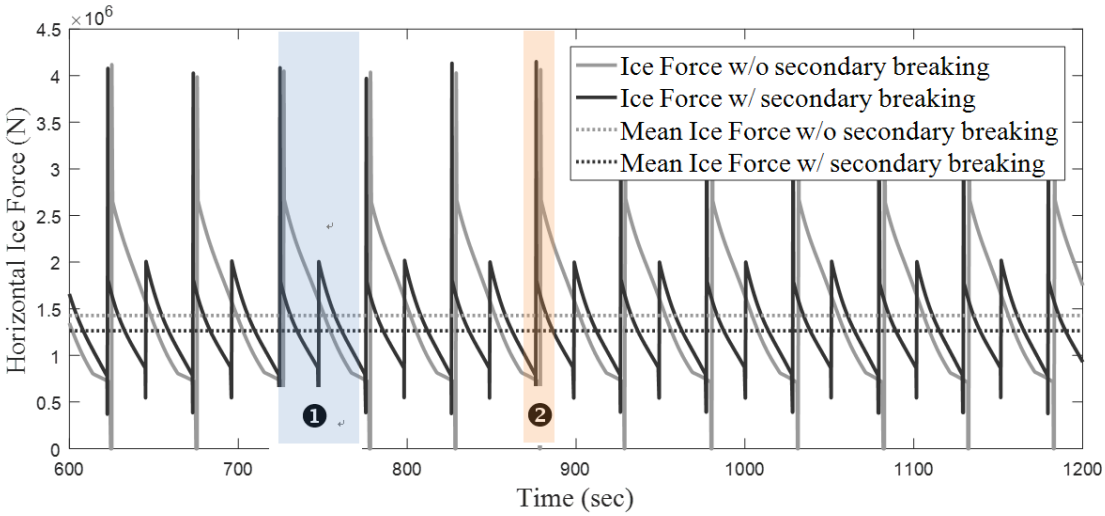

Figure 36. Total ice force behavior with and without second breaking (h_{ice}=2m, v_{ice}=0.5m/s)

In the field observation, the eventual ice breaking length varies in the range of approximately 3 to 10 times the ice thickness (ISO 19906, 2010). In the simulation, the first ice breaking length, which is the analytical solution by a beam equation, tend to be larger than the field observation. By applying the secondary ice breaking procedure, the breaking length is in the range suggested by ISO 19906.

Table 12. Average value of breaking length and ratio when including secondary breaking

Ice Thickness (m)	0.5	0.8	1.0	1.3	1.5	1.8	2.0
Mean breaking length (m)	4.47	6.36	7.53	9.17	10.22	11.72	12.69
Ratio	8.94	7.95	7.53	7.06	6.81	6.90	6.34

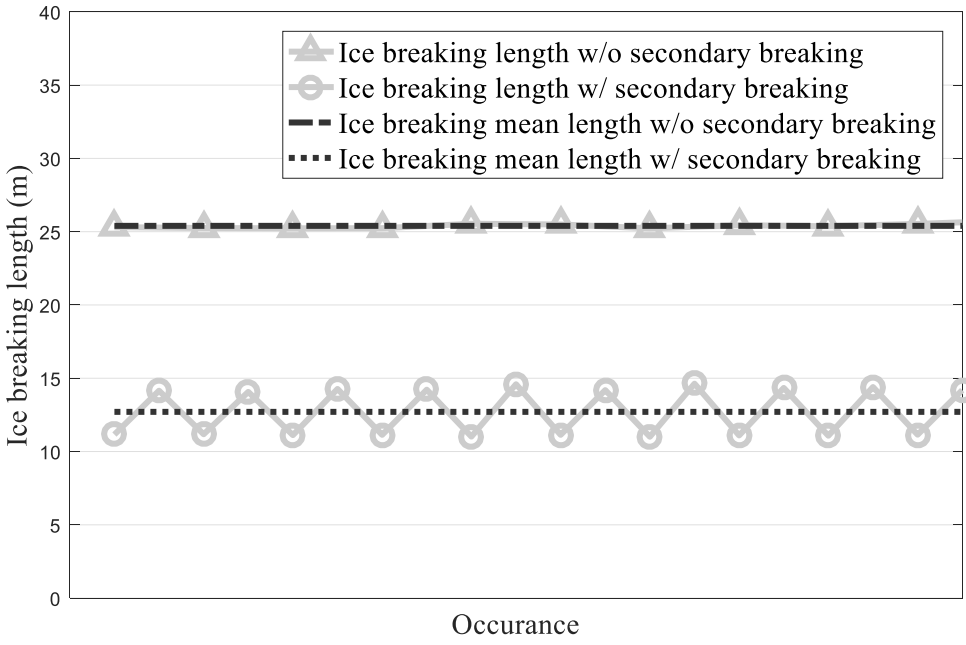

Figure 37. Breaking Length Comparison, (h_i=2m)

3.5.4 Platform motions

Since the present level ice load on a sloping structure is relatively smaller than the forces induced by the ridge ice or iceberg, the platform responses generally show small offset and oscillating motions. In the simulation, the negative relative velocity of the ice with respect to the platform implies that the sliding broken ice pieces are detached from the structure and drift away from the structure. As a result, zero force is applied on a structure from that portion. For the rotating broken ice, the detachment of the ice block can be found by geometrical consideration in each time step. Therefore, at a very low ice drift speed, detachment occurs when the platform moves faster than the level ice (❸). Thus, the maximum total ice force at the low drift speed is smaller than other cases. When the level ice moves fast enough so that ice is not detached from the structure, then the

structure exhibits small oscillating motions at its natural frequency. When the ice load frequency is close to the natural frequency of the platform, the response of the platform is amplified due to resonance. At ice drift speeds of 0.05 m/s and 0.1 m/s, the ice load energy is concentrated at the region close to the platform surge natural frequency of 0.02 rad/sec. The surge motion is strongly coupled with the pitch motion with a natural frequency of 0.16 rad/sec, when the ice drift speed is 0.3m/s.

Table 13. Statistics of platform surge motions with varying ice drift velocity (h_{ice} = 2m, 1000 sec~10000 sec)

Ice drift velocity	0.01	0.05	0.1	0.3	0.5	0.8	1
Max.	3.497	6.556	7.750	5.022	4.419	4.450	4.470
Min.	0.895	-1.368	0.306	3.280	4.044	4.054	4.149
Mean.	1.969	2.455	3.727	4.160	4.229	4.250	4.312
Std.	0.576	2.407	1.518	0.550	0.075	0.079	0.067

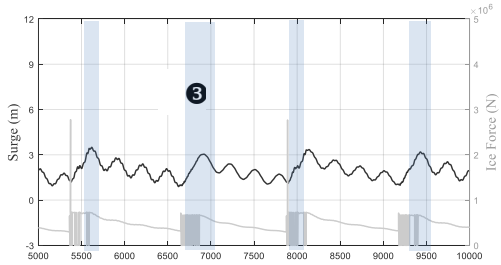

(a) v_{ice}=0.01m/s

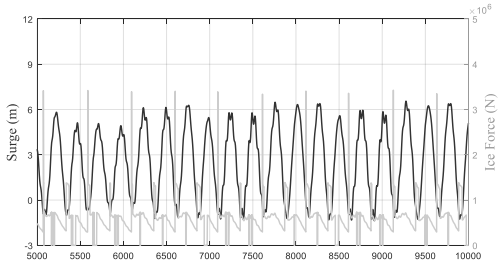

(b) v_{ice}=0.05m/s

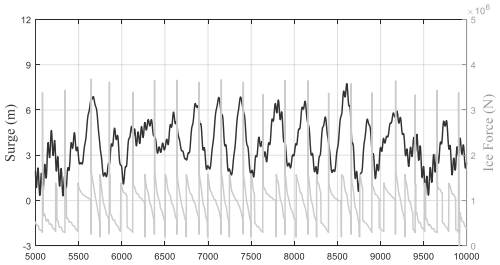

(c) v_{ice}=0.1m/s

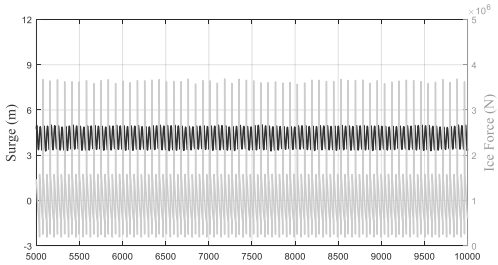

(d) vice=0.3m/s

Figure 38. Time series of platform surge motion (dark) and ice load (light) with varying drift velocity

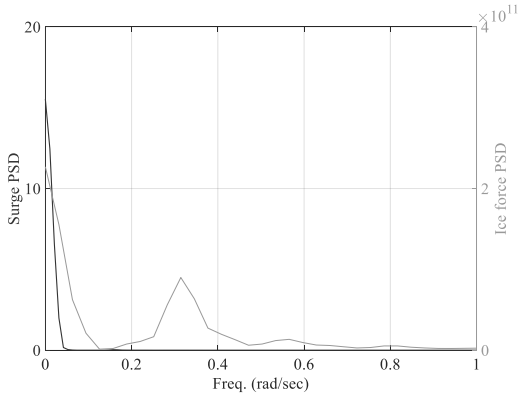

(a) v_{ice}=0.01m/s

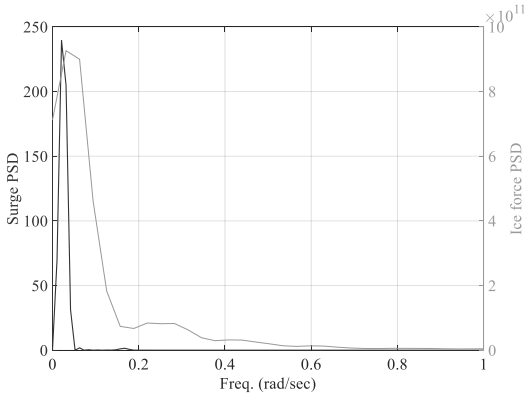

(b) v_{ice}=0.05m/s

Figure 39. Spectra of platform surge motion (dark) and ice load (light) with varying drift velocity

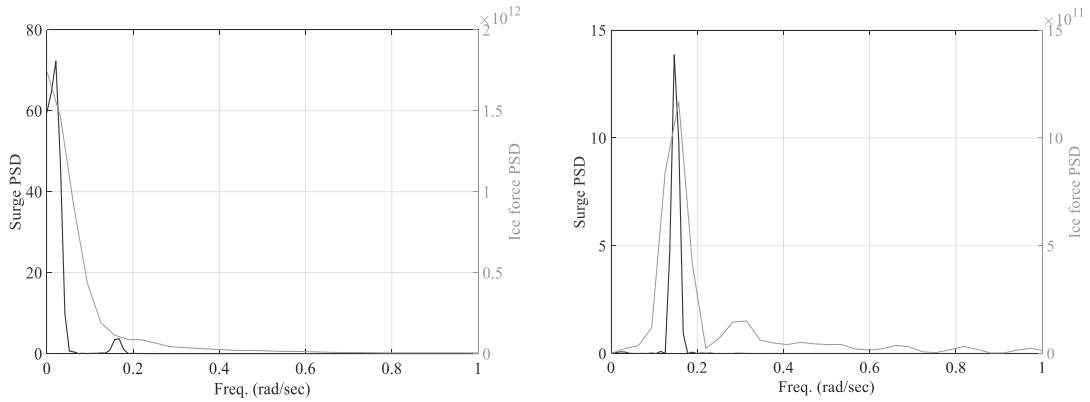

Figure 39. Continued

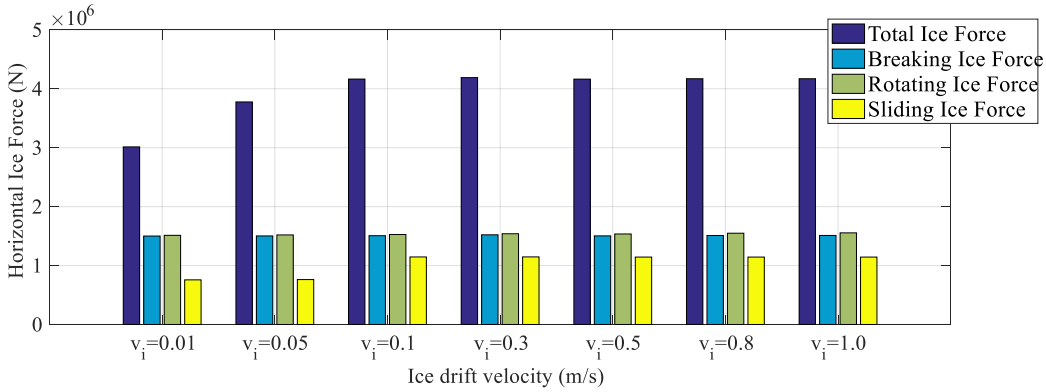

Figure 40. Ice force contribution of each phase with varying ice drift velocity (Maximum values, 1000 sec~10000 sec)

3.5.5 Mooring dynamics and statistics

The mooring forces are generally proportional to the platform surge motions. Therefore, the pattern and statistical results are similar to those of platform surge motions. At low drift speeds of about 0.1m/s, the mooring system experiences the largest forces, whereas the mean value drops slightly due to the interval of detachment between the ice and the platform.

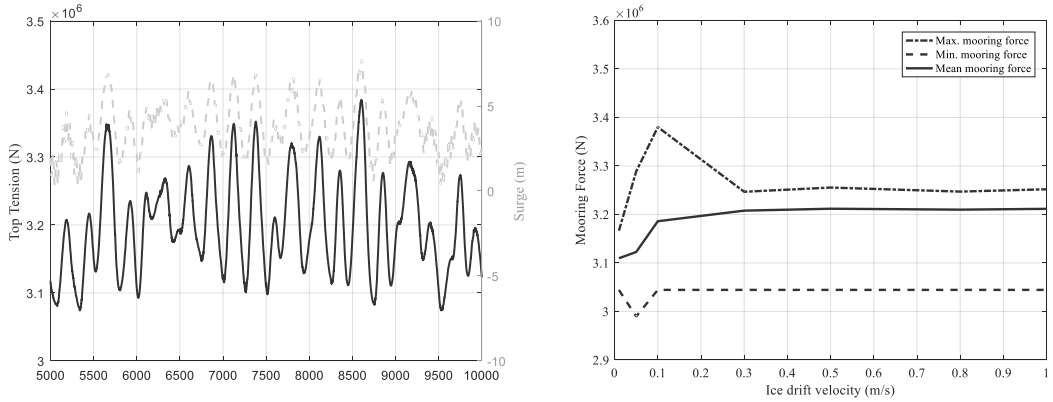

(a) Time-series of the line #8 top tension at the drift speed of 0.1 m/s (dashed line = surge, solid line = tension)

(b) Line #8 top tension statistics with varying drift speed

Figure 41. Mooring top tension results

3.6 Conclusions

The time-domain numerical simulation procedure for predicting the level ice load acting on the sloped floating structure and the interaction between them is investigated in this study. Three interacting phases are considered with analytical and theoretical formulas considering the relevant physics. In the breaking phase, the level ice is assumed to be a semi-infinite beam on an elastic foundation, and the corresponding solutions were adopted to calculate the breaking load and length. During the rotating phase, the fluid inertia and viscous forces are involved and by constructing the moment distribution curve, the secondary breaking was also simulated. When broken ice is parallel to the structure, the buoyant and frictional forces were obtained in the sliding phase. Through the numerical simulations, we can draw several conclusions.

- Generally, the global ice loads are repeated in a certain period, which is determined by the ice velocity and breaking length. The ice loads induced by bending failure are relatively smaller than other typical design loads under ice ridge, iceberg, or harsh wave conditions.
- The simulated maximum global forces are compared with the Ralston and Crosedale methods, and they were in reasonable agreement.
- Considering the presence of axial force, a slightly higher breaking force is obtained than that without it. Consideration of the finite level ice length does not show a big difference in the breaking loads as long as the length was larger than 100m.
- The secondary breaking occurs immediately following the first breaking, and it has a similar breaking length in the observed data, in the range of 3 to 10 times the ice thickness.
- The numerical simulation demonstrates the possibility of resonance between the ice loads and platform motions.
- Platform surge motions at low ice-drift speeds are larger as a result of the resonance between the ice loads and platform motions. At high drift speeds, the ice load frequency is far from the platform surge natural frequency and the resulting motions were small.
- The pattern of mooring tensions is similar to that of surge motions.

CHAPTER IV

LEVEL ICE AND FLOATING ARCTIC STRUCTURES INTERACTION USING THE COUPLED DISCRETE ELEMENT METHOD

4.1 Introduction

The discrete element method (DEM) is a numerical technique to construct or mimic the behaviour of particles and predict their characteristics. By using the DEM, level ice is modelled as the assembly of numerous particles. To solve the interaction of level ice and a floating platform with mooring lines, the open-source software, LIGGGHTS, is externally coupled with the in-house program, CHARM3D. In this section, a DEM analysis and LIGGGHTS are briefly introduced and discussed, and the method for an external coupling between CHARM3D and LIGGGHTS is presented. In the end of this chapter, case studies for a fixed structure and a floating Arctic Spar interacting with level ice are investigated.

4.2 Literature Review

The DEM is a computational method to compute the motion of a large number of small particles. It has been widely used in ice engineering to demonstrate ice phenomena

such as ice ridging (Hopkins, 1992, 1998), broken ice interaction (Loset, 1994; Liu and Ji, 2018), rubble pile-up (Paavilainen et al., 2011, 2015), and punch through tests (Polojärvi and Tuhkuri, 2009, 2013).

For the interaction between level ice and offshore structures, modeling of the realistic fracture behavior of level ice is required because there is a complex process of ice failure when an offshore structure is hit by level ice. Several researchers have used the parallel bonding method to model the ice fractures in DEM. It was first introduced and applied in a rock mechanics study by Potyondy and Cundall (2004) to model boding between granular particles. Several researchers have also widely used this method in ice engineering resulting in meaningful insights. Ji et al. (2014) studied the ice load on a fixed conical structure and compared it with experiment data performed in HSVA. They found that the ice loads increased with increasing ice-drift velocity, and the frequency of the ice load was well matched in both numerical and experimental data. Morgan et al. (2015) provided qualitative observations of an ice interaction with conical structures by numerically estimating the height of the rubble pile. Through multiple test cases, they found that thicker ice led to a rubble pile of greater height and depth, and the use of multiple layers of particles showed greater realism. Long et al. (2017) also simulated level ice approaching a vertical structure and measured ice local and global pressures during the crushing failure. They observed line-like high pressures zones on the middle line of the contact area, and the effect of the loading rate was discussed.

In this study, the interaction between level ice and offshore structures is numerically investigated using modified LIGGGHTS software, which is based on the DEM with a

parallel bonding model. Visual observations including the failure mode, broken ice pieces, cracks pattern, and the force transfer path are discussed based on case studies. Furthermore, this program is coupled with CHARM3D to analyze the fully-coupled level ice-floater-mooring dynamics.

4.3 DEM and LIGGGHTS

4.3.1 Dynamics of granular particles based on the DEM Analysis

The dynamic response of granular particles solved by the DEM is considered at the individual-particle level. The kinematics of individual particles are computed by integrating the particle equation of motion, and the trajectory of particles are tracked for the next integration.

$$\frac{dx_{p,i}}{dt} = v_i \tag{22}$$

where $x_{p,i}$ and v_i are the position and translational velocity of the i^{th} particle, respectively.

When the particle contacts and interacts with neighboring particles or walls, the contact force is applied on both sides, considering the material properties and relative kinematic characteristics. After constructing the force terms, the equations of the

translational and rotational motions in the DEM are represented by Newton's second law as follows:

$$m_i \frac{dv_i}{dt} = \sum_{j=1}^{N_c} (\mathrm{F}_{n,ij} + F_{t,ij}) + m_i g i$$
and
$$I_i \frac{d\omega_i}{dt} = \sum_{j=1}^{N_c} (\mathrm{T}_{\mathrm{t},ij} + M_{t,ij}) \quad (23)$$

where $\mathrm{F}_{n,ij}$ and $F_{t,ij}$ are the normal and tangential contact force, $m_i g$ is the gravitational force, $\mathrm{T}_{\mathrm{t},ij}$ is the tangential torque, $M_{t,ij}$ is the rolling friction torque, and N_c is the number of particles in contact with particle i.

Based on the Hertz contact model, the viscos-elastic model given in Eq. (24) is employed to calculate normal and tangential interacting forces. This model is comprised of a spring and a dashpot in both normal and tangential directions, whose interparticle forces depend on the normal and tangential overlap distances, $\delta_{n,ij}$ and $\delta_{\mathrm{t},ij}$, respectively.

$$F_{ij} = (k_n \delta_{n,ij} - \gamma_n v_{n,ij}) + (k_t \delta_{\mathrm{t},ij} - \gamma_t v_{\mathrm{t},ij}) \quad (24)$$

where k is the elastic constant, γ is the viscoelastic damping, v is the relative velocity of the two particles, and the subscriptions of n and t represent the normal and tangential

directions. The first and second terms are the normal and tangential force between the two particles, respectively. These parameters are defined with mass (m), radius (R), and the material properties of Young's modulus (Y), Poisson's ratio (υ), and coefficient of restitution (e) as follows:

$$
\begin{aligned}
&k_n = \frac{4}{3} Y^* \sqrt{R^* \delta_n}, \\
&\gamma_n = -2\sqrt{\frac{5}{6}} \beta \sqrt{S_n m^*} \geq 0, \\
&k_t = 8G^* \sqrt{R^* \delta_n}, \\
&\gamma_t = -2\sqrt{\frac{5}{6}} \beta \sqrt{S_t m^*} \geq 0
\end{aligned}
\tag{25}
$$

$$
\begin{aligned}
&S_n = 2Y^* \sqrt{R^* \delta_n},\ S_t = 8G^* \sqrt{R^* \delta_n}, \\
&\beta = \frac{\ln(e)}{\sqrt{\ln^2(2) + \pi^2}},\ \frac{1}{Y^*} = \frac{(1-\upsilon_1^{\,2})}{Y_1} + \frac{(1-\upsilon_2^{\,2})}{Y_2} \\
&\frac{1}{G^*} = \frac{2(2-\upsilon_1)(1+\upsilon_1)}{Y_1} + \frac{2(2-\upsilon_2)(1+\upsilon_2)}{Y_2} \\
&\frac{1}{R^*} = \frac{1}{R_1} + \frac{1}{R_2},\quad \frac{1}{m^*} = \frac{1}{m_1} + \frac{1}{m_2}
\end{aligned}
\tag{26}
$$

4.3.2 Parallel bond model

In this study, level ice is modeled by the number of particles connecting with each other based on the parallel bonding model by Potyondy and Cundall (2004). Two particles are linked by a bond model and the interacting forces are calculated based on the

deformation of an elastic bonding disk transferring forces including tension, compression, shear, twisting, and bending moments. These forces are computed with normal and tangential bonding stiffness.

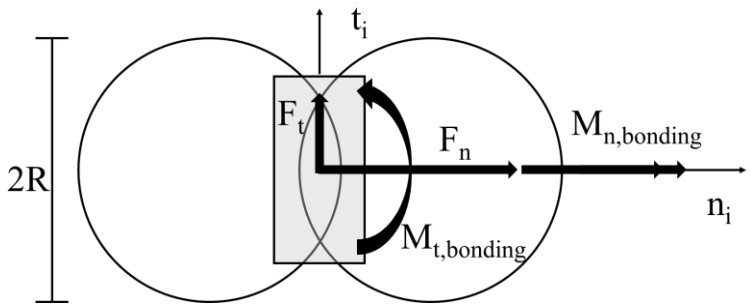

Figure 42. Parallel bonding model

$$\begin{cases} F_i = F_{n,bonding} n_i + F_{t,bonding} t_i = k^{nb} U^n + k^{sb} U^s \\ M_i = M_{n,bonding} n_i + M_{t,bonding} t_i = k^{sb} J \theta^n + k^{nb} I \theta^s \end{cases} \tag{27}$$

where $F_{n,bonding}$, $F_{t,bonding}$, $M_{n,bonding}$, $M_{t,bonding}$ are normal and tangential forces and moments acting on the bonding disk, and I and J are the moment of inertia and polar moment of inertia of the parallel bond cross-section, respectively. They are given by Eq. (28)

$$A = \pi R^2, \qquad J = \frac{1}{2}\pi R^4, \qquad I = \frac{1}{4}\pi R^4 \tag{28}$$

According to Potyondy and Cundall (2004), the normal and tangential bonding stiffness can be computed by Eq. (29), which is the function of the elastic modulus, Poisson's ratio, and particle diameter.

$$k^{nb} = \frac{E}{D}, \quad k^{sb} = \frac{G}{D} = \frac{E}{2(1+\upsilon)}\frac{1}{D} \tag{29}$$

The maximum tensile and shear stresses are calculated by Eq. (30) following the beam theory.

$$\sigma_b = \frac{\left|F_{n,bonding}\right|}{A} + \frac{\left|M_{t,bonding}\right| R}{I} < \sigma_{b\max}$$
and
$$\tau_b = \frac{\left|F_{t,bonding}\right|}{A} + \frac{\left|M_{n,bonding}\right| R}{J} < \tau_{b\max} \tag{30}$$

where σ_b and τ_b are the tensile and shear bonding stresses, $\sigma_{b\max}$ and $\tau_{b\max}$ are the maximum tensile and shear bonding stresses, and A is the area of the parallel bond cross-section. Once these stresses exceed the critical stress in either the normal or shear

directions, the bond between the particles breaks and the particles behave as an individual particle following Eq. (24) above.

4.3.3 Integration Method

With the equation of the particle's motion and computed forces, the kinematics of each particle are solved by a Velocity-Verlet integration scheme. A Velocity-Verlet algorithm is a numeric integration method that determines the positions of the particles. The position and velocity of the particles are determined by the following equation:

$$x(t+\Delta t) = x(t) + v(t)\Delta t + \frac{1}{2}a(t)\Delta t^2$$
$$v(t+\Delta t) = v(t) + \frac{a(t)+a(t+\Delta t)}{2}\Delta t \tag{31}$$

Compared to the basic Verlet algorithm (the central difference scheme), the Velocity-Verlet algorithm incorporates velocity explicitly, which means that the velocity and position are calculated at the same timestep. In particular, it uses the basic Verlet algorithm for the first timestep.

4.3.4 LIGGGHTS

LIGGGHTS stands for **L**AMMPS **I**mproved for **G**eneral **G**ranular and **G**ranular **H**eat **T**ransfer **S**imulations that is developed and distributed by DCS Computing and CF-DEM research (Kloss et al. 2012). It is an open source program for modelling granular materials,

and the extended version of LAMMPS (a molecular dynamic simulator), which is widely used in the field of molecular dynamics. LIGGGHTS is written in the computational language, C++, with object-oriented programing and massage passing interface (MPI) coding for the DEM.

LIGGGHTS has several advantages:

- The complex geometry can be imported from a computer-aided design (CAD) to a LIGGGHTS simulation, which enlarges the engineering applications to be solved.
- The parameters in the contact force formulations are described by the material properties of the granular material such as density, Young's modulus, Poison's ratio, and coefficient of restitution.
- It runs on a single processor or in parallel using message-passing parallelism. The computation for systems with only a few particles up to millions or billions can be efficient.
- LIGGGHTS is an open source code and is available for free with a well-documented manual. In addition, the Internet forums is actively used among a large user community to improve the software.

4.3.5 External coupling between CHARM3D and LIGGGHTS

CHARM3D is suitable to analyze a floating structure with mooring lines, considering the hydrodynamic effects and nonlinear wave forces. LIGGGHTS is also a useful and powerful software program to model level ice with multiple particles and estimate the ice

impact on the structures. By coupling the two programs, the interaction of a fully-coupled ice-floater-mooring is simultaneously resolved over time.

CHARM3D and LIGGGHTS have different programming approaches. First, CHARM3D and LIGGGHTS use different computational languages: Fortran77 vs. C++. Second, the programming methods are different: procedural programming (PP) vs. object-oriented programming (OOP). Thus, implementing one program with another requires considerable work. Therefore, the external coupling method is used for this study. The two programs run individually, but by sharing the data externally through the computer memory system, they feed and obtain the necessary data from/to each other.

To achieve external coupling between the two programs, a named pipe method (Figure 43) is employed. This inter-process communication (IPC) method is an extension of the traditional pipe concept. It links two separate processes using a filesystem in Unix so the two separate processes can access the named pipe at the same time and transfer the data to the other. The named pipe is also called first-in-first-out (FIFO), because it has the function of organizing and manipulating the data buffer. If one side of the program sends the data to the named pipe, none of the processes send the data anymore before the data in the named pipe is processed. Therefore, if the two programs are set to have the same time interval in the simulation, a time-marching algorithm for both programs is not necessary, because the named pipe itself provides the function of a data buffer.

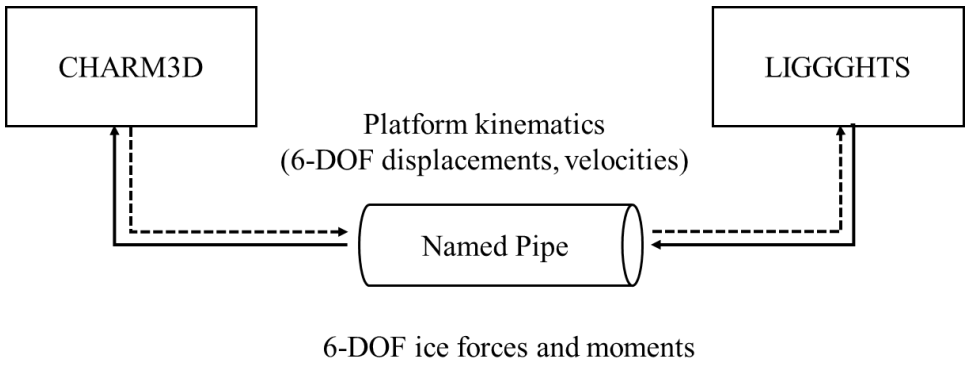

Figure 43. External coupling scheme (CHARM3D - LIGGGHTS)

Another coupling issue is MPI coding in LIGGGHTS. MPI stands for message passing interface, which allows the parallel computation of simulations with multiple processes. The primarily process moves data to another process to distribute the computation load, and the simulation runs in parallel. It is useful to simulate multiple particles by reducing the computation time efficiently. In LIGGGHTS, the spatial decomposition by many cores is made by splitting the entire simulation box into multiple parts. The particles in these subdomains are computed by individual MPI processes. By slightly extending the subdomains with halo regions, the particles close to the boundary of its neighboring process's subdomain are managed.

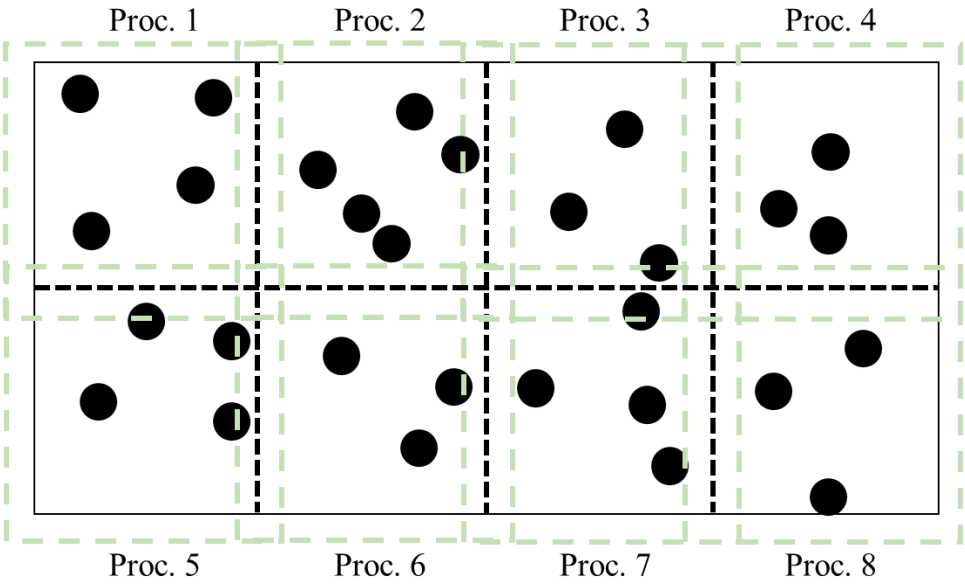

Figure 44. Spatial decomposition of simulation domain

The primary process (rank 0) receives the platform's kinematics data from CHARM3D, and distributes this information to other processes by using the call function, "MPI_Bcast." This communication occurs after the first integration step when the particle positions have been updated. The general schemes of communication between multiple processes is depicted in Figure 45. For this coupling, an open MPI library is used with C++.

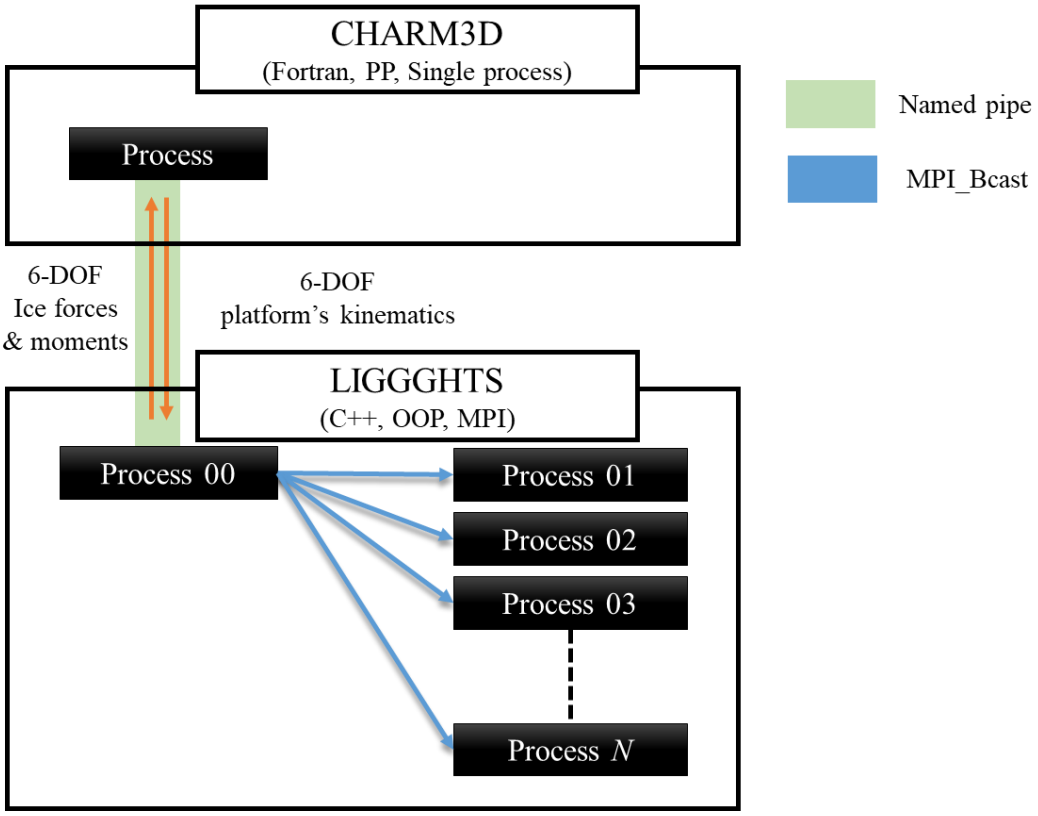

Figure 45. External coupling scheme between CHARM3D and LIGGGHTS using the named pipe and MPI coding

4.4 Numerical Simulation using the DEM

4.4.1 Ice properties in DEM

In the DEM, the ice is modeled with an assembly of multiple bonded spherical particles. All properties of the spherical particles follow the ice mechanical properties such as Young's modulus and Poisson's ratio. According to the ISO standard, the friction coefficient between the ice and ice is the value of 0.1. However, since the particle shape is spherical, and the surface of ice blocks is irregular, the friction coefficient of 0.3 is used. For the same reason, the friction coefficient between the structure and ice is set to be 0.3.

The restitution coefficient is a very low value of 0.1 in this simulation. For the entire ice block, a hexagonal closed-packing (HCP) pattern is used to avoid orthogonal cracks and maximize the occupied volume per unit cell where the atomic packing factor (APF) is 0.74, as depicted in Figure 46. The uniform particle diameter is used in the simulations. The effects of the particle size and size distribution are not included in this study, and will be investigated in a future scope.

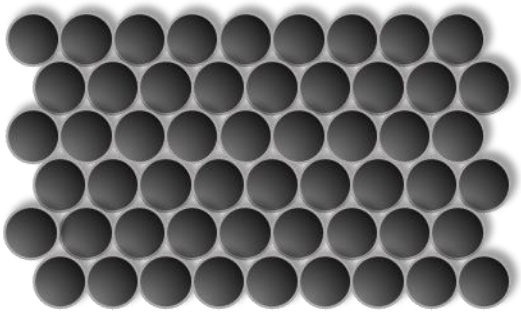

Figure 46. Hexagonal closed-packing of spherical particles

For a bonding parallel model, the bonding stiffness and strength are required. The normal and shear bonding stiffness between the bonded particles are determined with the elastic modulus and a diameter of the particle by Eq. (29), considering the effect of the particle size. The bonding strength, a conceptual parameter to mimic the bond between the particles, is significantly related to the critical force at the fracture because the fracture occurs when the bond breaks. To determine the bonding strength, a numerical three-point beam-bending test is conducted with a beam size of L x h x b = 30d x 4d x 4d with 933 particles, as shown in Figure 47 (d represents the diameter of particles). Two fixed ends

support the beam and a downward constant load F_{max} is applied on the middle of a beam. The flexural strength is the strength when the beam is subjected to the maximum loading (F_{max}) without the fracture, and can be determined by the following equation.

$$\sigma_f = \frac{3}{2}\frac{F_{\max} L}{bh^2} \quad \Leftrightarrow \quad F_{\max} = \frac{2}{3}\frac{bh^2}{L}\sigma_f = \frac{64}{45}d^2\sigma_f \tag{32}$$

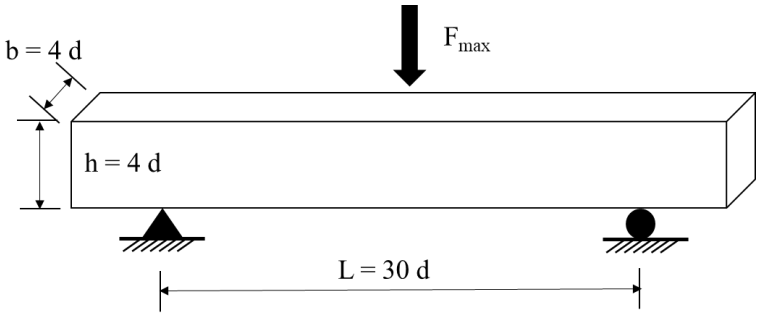

Figure 47. A numerical three-point beam bending test

With the given beam size and particle diameter as well as the ice flexural strength, the maximum force, F_{max}, can be defined by Eq. (32). By varying the bonding strength, a parametric study is conducted to check the bending failure of the beam.

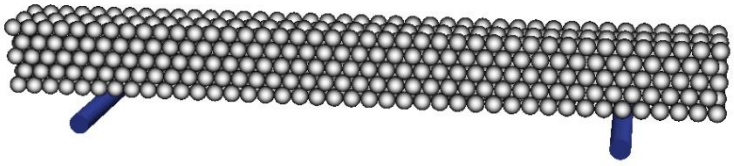

Figure 48. A numerical three-point bending test by the DEM

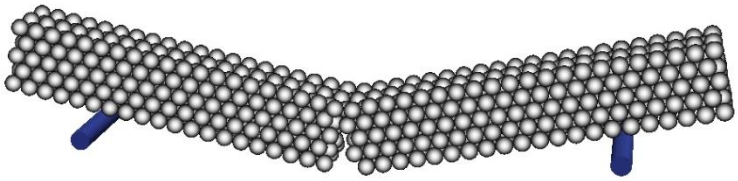

Figure 51. continued

Figure 51. continued shows the failure process of an ice beam simulated by the DEM. The results show that the fracture occurs in the middle of the beam due to the excessive tensile stress on the middle bottom particles, and the bonding strength corresponding to the fracture is used in the simulation

4.4.2 Simulation Configuration

In this study, the Rayleigh timestep in Eq. (33) is employed to determine the critical timestep (Δt_c) of numerical integration. It is assumed that all energy is transferred across the granular system through Rayleigh waves, which means that the energy cannot propagate immediately from a particle across the neighboring particles in a single timestep.

$$\Delta t_c = \frac{\pi R}{(0.1631\upsilon + 0.8766)}\sqrt{\frac{\rho}{G}} \tag{33}$$

where R is the particle radius, ρ is the particle density, G is the shear modulus, and ν is the Poisson's ratio. Due to the shape of the meshes and possibility of high particle

velocities, the conservative constant timestep of less than 20% of the Rayleigh timestep is chosen.

For efficiency of the computation, the boundary of the simulation domain is set to be non-periodic and fixed. Thus, if the particles move out of the simulation domain, the dynamics are no longer considered in the simulation. As a general setting, the gravity force is applied to all particles, while buoyancy and viscous forces are properly applied to demonstrate the fluid interaction below the waterline. To conserve the energy of the entire system, a NVE dynamic ensemble (the constant energy and volume) is employed for the numerical integration scheme. The general setting for DEM is summarized in Table 14.

Table 14. Simulation configuration for DEM

Parameter	Setting
Critical timestep	less than 20% of Rayleigh timestep
Boundary	non-periodic and fixed
Additional forces	gravity, buoyancy, and viscous forces
Integration type	NVE

4.4.3 Level ice and a fixed structure interaction with DEM

First, the validation of the ice model by the DEM is conducted for a fixed structure by comparing the experimental data before LIGGGHTS is coupled with CHARM3D. For comparison, the experimental data from the ice model test performed at NRC (Barker et

al., 2005; Gravesen et al. 2005) is used. The interaction of a conical structure (Figure 49) with a 55-degree angle with level ice is investigated.

The ice properties are given by the experimental test set-up as tabulated in Table 15. The thickness of the ice sheet is 0.023 m. Therefore, for a two-layer ice sheet with HCP, the diameter of the particle is determined to be 0.0123 m. The bonding strength of 70 kPa is determined by the numerical beam test described in the section above, corresponding to the flexural strength of 38 kPa. The ice width of 1.6 m is determined that the both sides of ice sheet cannot break. In addition, another simulation with a twice larger width (i.e. 3.2 m) shows the relatively similar extreme values of ice forces. The length of 2 m is chosen to observe multiple bending failures during numerical simulations. The ice drift velocities are 0.04, 0.08, 0.14, and 0.20 m/s.

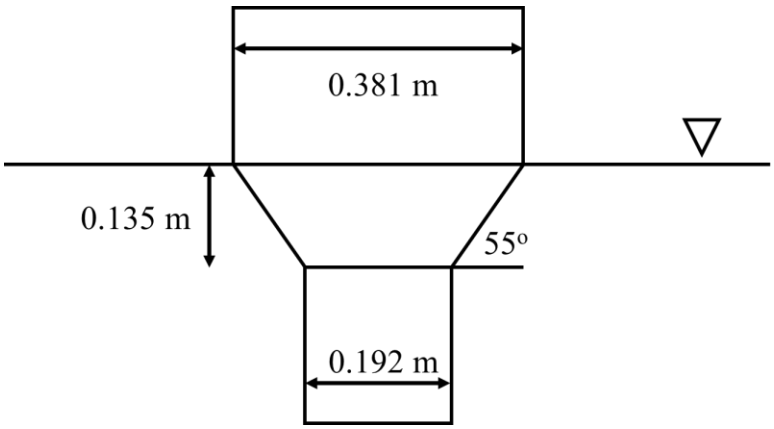

Figure 49. Configuration of a fixed-type downward conical structure

Table 15. Ice properties for DEM simulations

Parameter	Symbol	Unit	Value
Young's Modulus	E	GPa	0.1
Flexural Strength	σ_f	kPa	38
Frication coefficient (ice-ice)	μ_{ii}	-	0.3
Frication coefficient (ice-structure)	μ_{is}	-	0.3
Restitution coefficient	e_{ii}	-	0.1
Bonding normal stiffness	K^{nb}	GPa/m	E/d
Bonding tangential stiffness	K^{sb}	GPa/m	E/2(1+ν) d
Maximum tensile bonding strength	σ_{bmax}	kPa	70
Maximum shear bonding strength	τ_{bmax}	kPa	70
Ice thickness	h_i	mm	22
Ice density	ρ_i	kg/m^3	900
Water density	ρ_w	kg/m^3	1000

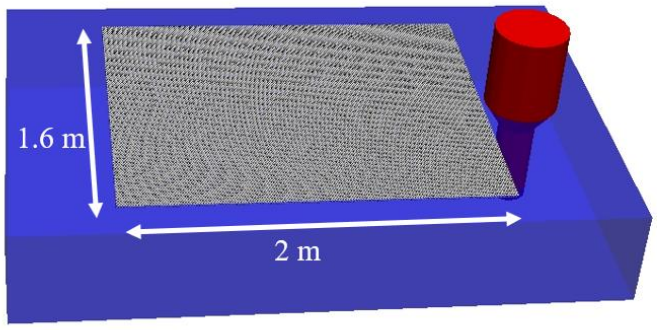

Figure 50. Numerical test setup for DEM simulations

Figure 51 represents the snapshots of the ice-structure interaction with the ice drift velocity of 0.2 m/s. From the visual observation, continuous bending failures are observed,

forming multiple wedge-shaped broken ice. Due to the relatively low drift velocity, the rubble ice accumulated in front of the structure is observed with the thickness 3~4 times greater than an ice thickness.

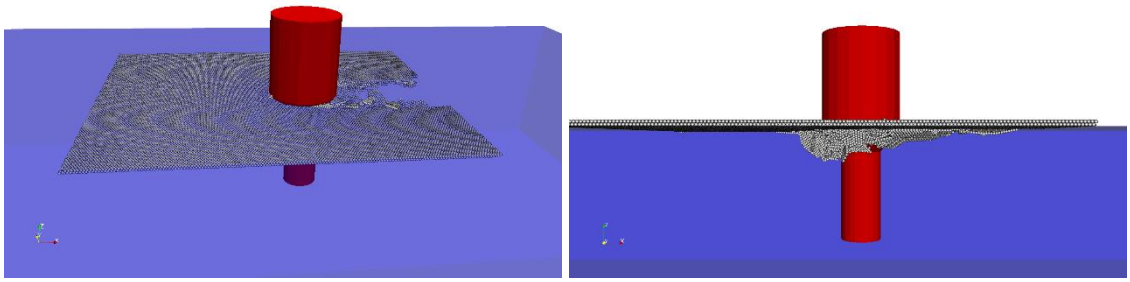

(a) (b)

Figure 51. Snapshots of the ice-structure interaction with the ice drift velocity of 0.2 m/s in (a) general view and (b) side view

Figure 52 shows the ice force acting on the inverted conical structure in the x direction. Due to the flexural bending failure, the “saw-tooth” pattern in the time history is observed. When the intact ice sheet hits the structure, it is deflected underneath the sloped surface of the structure. Once the internal stress between the particles exceeds the boding strength in either the normal or shear direction, the ice sheet bending fails, having a large peak force, as shown in Figure 52. After the fracture of the ice sheet, the ice force suddenly decreases, and the broken ice pieces are submerged under the structure and finally cleared away from the structure. During this procedure, the ice force fluctuates considerably due to multiple collisions among the broken ice pieces interacting with the structure.

Since these are 3D simulations, the ice force in the y direction is also obtained from the numerical simulation as depicted in Figure 53. The notable pattern of the ice force in the y direction is not observed because the structure is symmetrical in the y direction and the ice sheet only moves in the x direction. Sometimes, the large force occurs simultaneously when the intact ice sheet fails.

The ice force statistics obtained by the numerical simulations are compared with the model test measurements, as shown in Figure 54. The numerical simulation results of the ice force in the x direction show that the ice force increases with increasing ice drift velocity. The maximum force of 45.3 N and the mean value of 8.5 N at the ice drift velocity of 0.20 m/s is twice and 1.8 times greater than those at 0.04 m/s, respectively. The maximum value is approximately 5 times greater than the mean value. In the y direction, the maximum forces as well as the standard deviations are smaller than those in the x direction. Due to the symmetrical geometry of the structure, the mean values of all cases are close to zero. Considering the complex mechanism of the fracture interaction between ice and structure, the numerical simulation results are reasonably well matched with the experimental data in both x and y directions. The ice force statistics are summarized in Table 16.

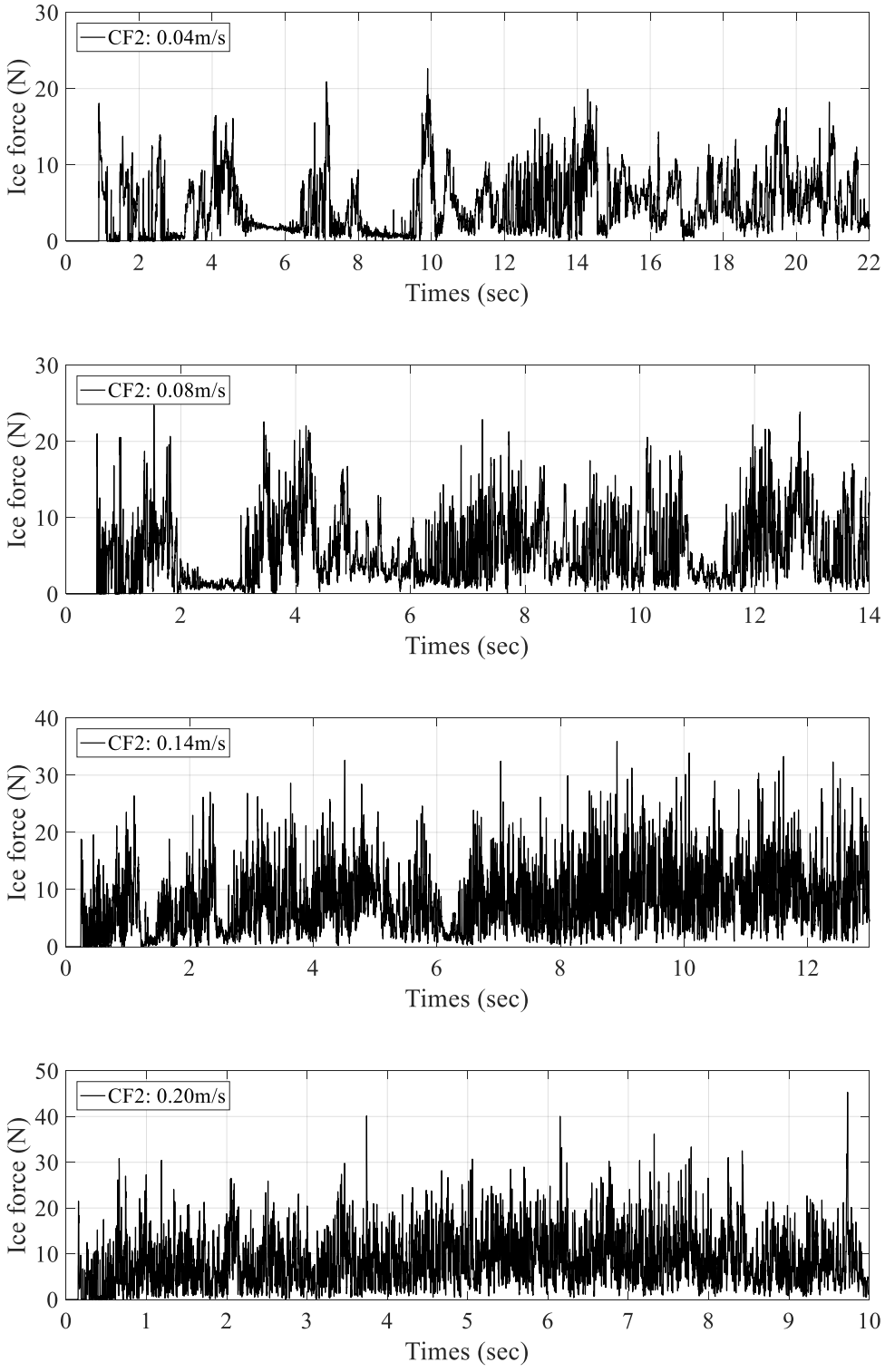

Figure 52. Ice force time-series in the x direction with varying ice drift velocities

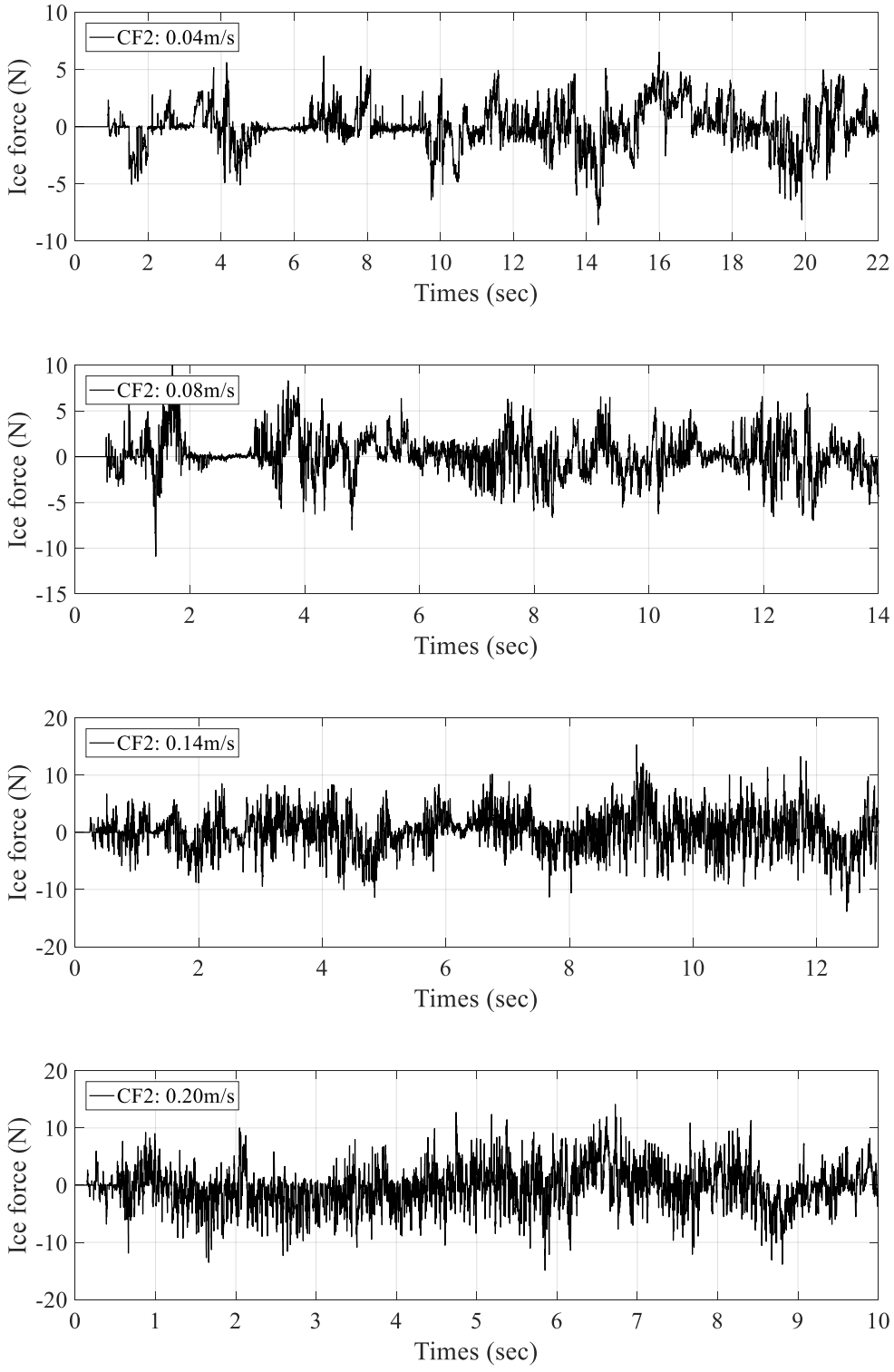

Figure 53. Ice force time-series in the y direction with varying ice drift velocities

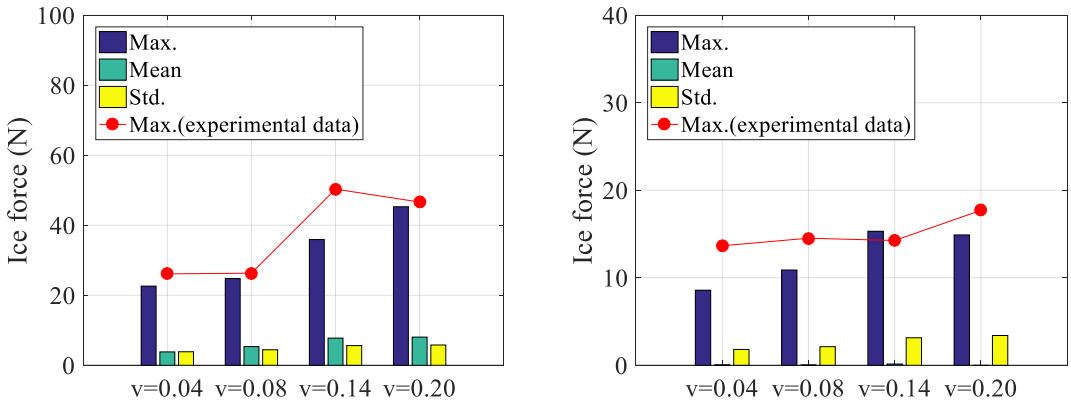

Figure 54. Ice force statistics in the x and y direction with varying ice drift velocities

Table 16. Ice forces statistics on a fixed structure by the DEM (unit: N)

	v = 0.04 m/s		v = 0.08 m/s		v = 0.14 m/s		v = 0.20 m/s	
	Fx	Fy	Fx	Fy	Fx	Fy	Fx	Fy
Max.	22.618	6.519	30.229	9.969	35.915	15.314	45.299	14.124
Min.	-0.230	-8.581	0.011	-10.887	0.064	-13.840	0.031	-14.896
Mean	4.629	0.041	5.860	0.041	8.083	0.166	8.451	-0.437
Std.	3.769	1.852	4.446	2.172	5.583	3.249	5.705	3.493

The ice force frequency is investigated with the PSDs of the time-series of the ice forces. The dominant frequencies corresponding to the ice drift velocity are marked in Figure 55. In the experiment, the linear relation between the ice drift velocity and the ice force frequency is approximated with a ratio of 62.9, while the numerical simulation has the ratio of 59.8. In general, the experimental and numerical results are in good agreement.

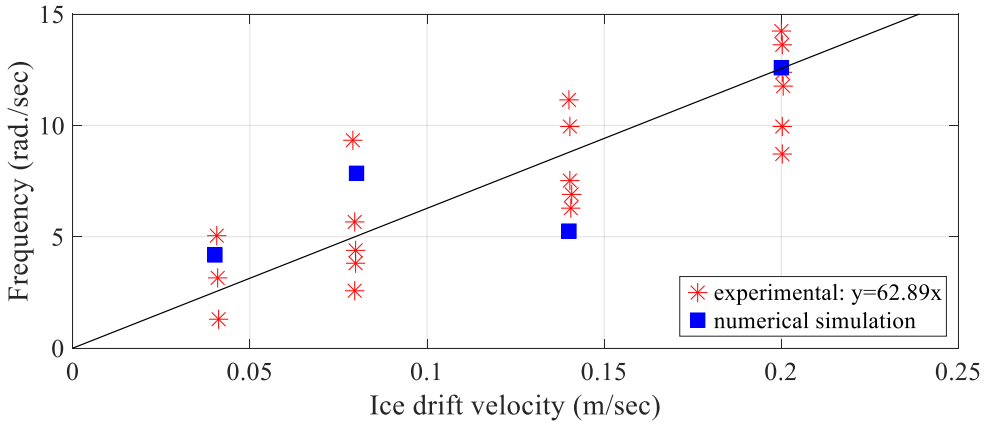

Figure 55. Ice force frequencies with varying ice drift velocities

4.4.4 Level ice and the square-shaped Arctic Spar interaction with DEM

The floating offshore structures of Arctic Spar (Figure 56) with a sloped surface around the waterline are modeled to investigate the interaction with level ice using the DEM. The hull is square-shaped and the properties of the entire system are the same as those of the Arctic Spar model used in Chapter III. The characteristics of Arctic Spar and mooring lines are summarized in Table 7 through Table 9 in Chapter III.

To maintain the same configuration of the numerical simulation with the one in Chapter III, the same ice properties given in Table 10 are directly adopted for the DEM simulations here. Since the simulation in Chapter III assumes that the ice-width is equal to the width of the hull at the waterline, the ice width is set to be 40 m, and the length varies from 400 m ~ 1600 m depending on the ice drift velocity. The ice thickness of 2 m is modeled with two layers of spherical particles whose diameter is 1.071 m, following HCP. The bonding strength is determined by the numerical 3-point beam test as described in 4.4.1. The ice properties used in the DEM are summarized in Table 17.

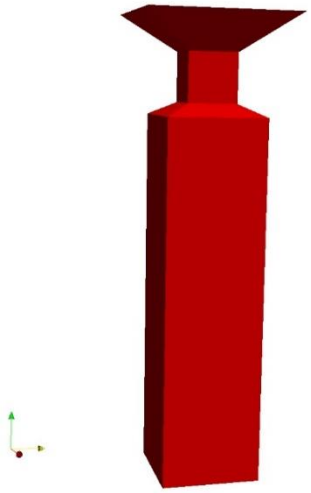

Figure 56. Arctic Spar Model for DEM simulations

Table 17. Ice properties of level ice interacting with Arctic Spar

Parameter	Symbol	Unit	Value
Particle diameter	d	m	1.071
Poisson's ratio	ν	-	0.3
Young's Modulus	E	GPa	4
Flexural Strength	σ_f	kPa	500
Frication coefficient (ice-ice)	μ_{ii}	-	0.3
Frication coefficient (ice-structure)	μ_{is}	-	0.3
Restitution coefficient	e_{ii}	-	0.1
Bonding normal stiffness	K^{nb}	GPa/m	3.732
Bonding tangential stiffness	K^{sb}	GPa/m	1.435
Maximum tensile bonding strength	σ_{bmax}	MPa	2.2
Maximum shear bonding strength	τ_{bmax}	MPa	2.2
Ice thickness	h_i	m	2
Ice density	ρ_i	kg/m^3	900
Water density	ρ_w	kg/m^3	1025

Figure 57 represents the dynamic interaction of an Arctic Spar with level ice. It is observed that the moving level ice generally fails in bending by either hitting the Arctic Spar or rubble ice under the Arctic Spar. After considerable breaking, the broken ice pieces accumulate in front of the structure, as shown in Figure 57(b). The maximum thickness of the rubble ice is approximately 3~4 times the ice thickness. These accumulated rubble ice pieces push the structure, and the structure in an oscillating motion in surge. Because the intact ice sometimes breaks by hitting the rubble ice, cracks that form on the intact ice sheet are not parallel to the structure width, but have a random pattern.

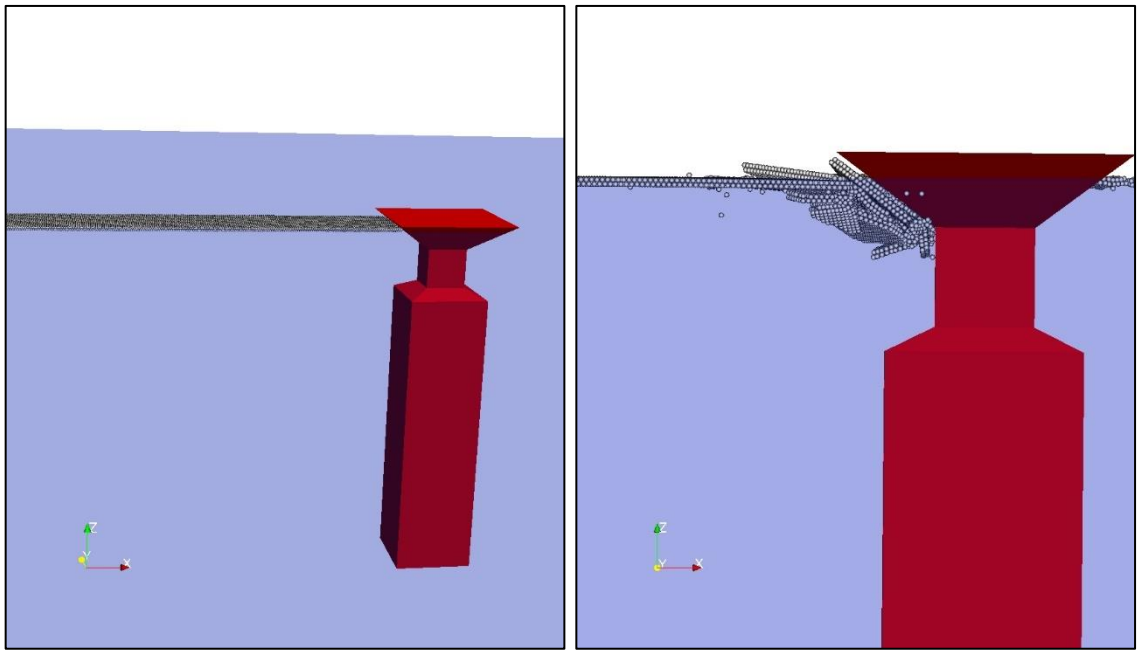

(a) (b)

Figure 57. Snapshots of the ice-structure interaction with the ice drift velocity of 1 m/s in (a) general view and (b) close view

Figure 58 ~ Figure 60 show the surge/heave ice forces and corresponding surge motion with varying ice velocity. The rate of the ice forces increases as the ice drift velocity increases. In all cases, rubble pile-up along the sloped surface is observed, and the ice forces have positive values over time. At the low ice drift velocity of 0.1 m/s, the ice force gradually increases with the structure motion. At the velocity of 0.3 m/s, the resonance of the Arctic Spar in the surge direction is observed, and the period of the ice force is close to that of the surge motion oscillating with a large amplitude (Figure 59). It can be more clearly seen in Figure 61 that the ice force peak frequency in the PSD plot is located at 0.03 rad/sec which is very close to the surge natural frequency of 0.02 rad/sec. At the high velocity of 1.0 m/s, the ice continues breaking with a random pattern, and the structure motion converges to an equilibrium position with a small amplitude. In general, the ice force frequency increases with increasing ice drift velocity. However, when the ice velocity is higher, the ice force becomes non-periodic and random, as shown in Figure 61.

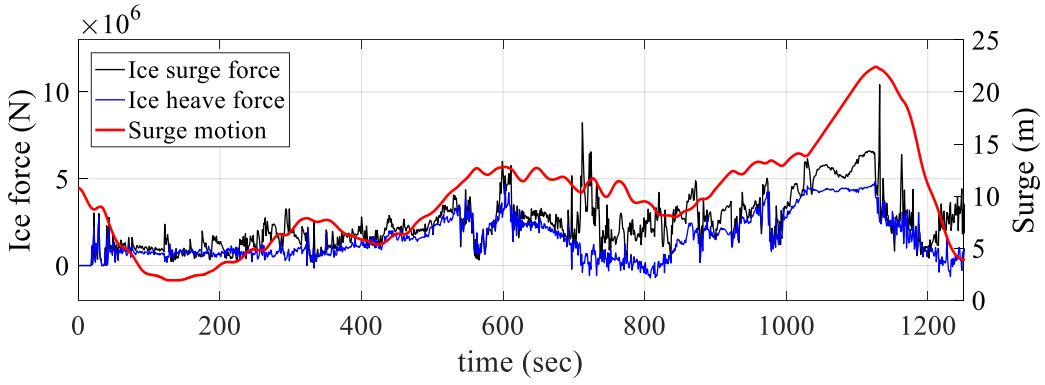

Figure 58. Ice force and surge motion in surge (v_ice = 0.1 m/s)

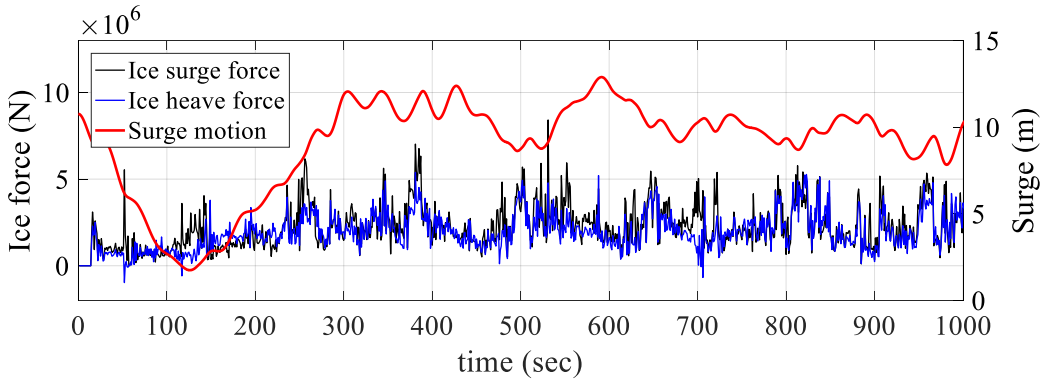

Figure 59. Ice force and surge motion in surge (v_ice = 0.3 m/s)

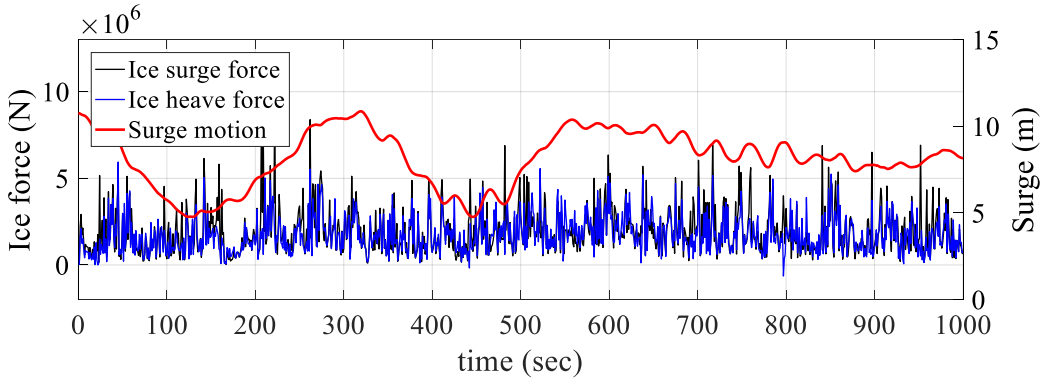

Figure 60. Ice force and surge motion in surge (v_ice = 1.0 m/s)

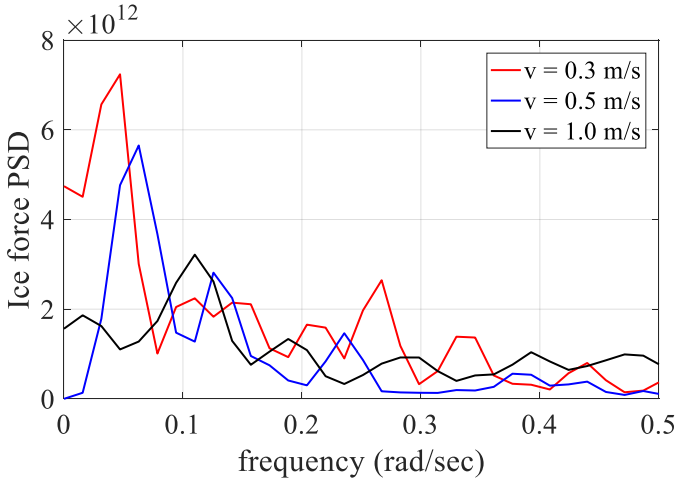

Figure 61. Ice force PSD with varying ice drift velocity

In Chapter III, the rubble effect is ignored, and rubble effect terms in the theoretical methods are excluded in the calculation of the ice forces. However, from visual observation using the DEM, rubble with a thickness of approximately 3~4 times the ice thickness is observed, when the level ice interacts with the square-shaped Arctic Spar. the factor of 3 is used to account for the rubble ice thickness in Ralston's method, while the theoretical method by Croasdale (Eq. (21)) is extended as follows:

$$F_H = H_B + H_P + H_R + H_L + H_T \tag{34}$$

where F_H is the horizontal ice force, H_B is the breaking force, H_P is the force required to push the sheet ice through the ice rubble, H_R is the load to push the ice blocks up the slope though the ice rubble, H_L is the force required to lift the ice rubble on top of the advancing ice sheet, and H_T is the force to turn the ice block at the top of the slope. Since the ice width is the same as that of the structure, the factor for 3D effect is not considered in the calculation. The detailed equations for each term can be found in ISO 19906 A.8.2.4.4.3.

Based on these considerations, the ice forces of 10.3 MN and 7. 4 MN are computed using Ralston's and Croasdale's methods, respectively, which are about 3 ~ 4 MN greater than those in Chapter III. Therefore, the hull shape effect plays the significant role in the formation of rubble pile-up as well as the maximum ice force. The maximum ice forces using numerical simulations are in a range between the forces used in Croasdale's and Ralston's methods.

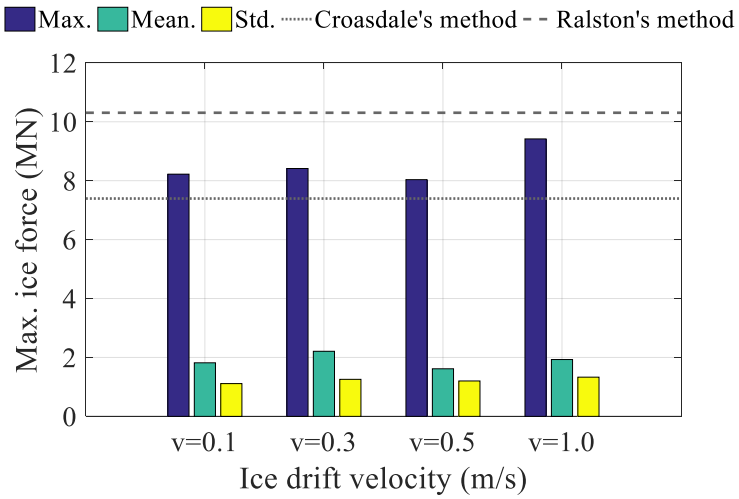

Figure 62. Statistics of ice forces

4.4.5 Level ice and the round-shaped Arctic Spar interaction with the DEM

In the previous section, a 2D simulation with a square-shaped Arctic Spar is simulated in level ice with the same width as the structure width at the waterline. In this section, the ice-structure interaction is simulated under more realistic conditions without any assumptions. To consider the 3D effect, a round-shaped hull Arctic Spar is modeled. For computation efficiency, the ice width is determined to be 300 m so the sheet ice at both sides cannot break. Different lengths of ice sheet varying from 400 m to 800 m are carefully determined depending on the ice drift velocity for computation efficiency. The same ice properties given in Table 17 are used here.

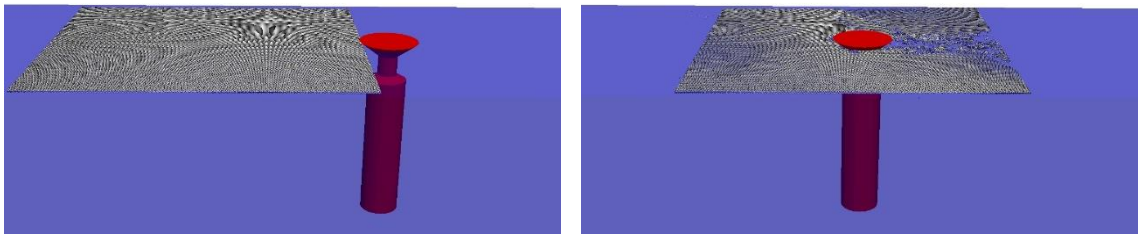

(a) (b)

Figure 63. Snapshots of ice-structure interaction at (a) t = 0 sec and (b) t = 200 sec with ice drift velocity of 1 m/s

Figure 63 shows the snapshots of a round-shaped Arctic Spar interacting with level ice at different times. When ice approaches and hits the structure, the ice sheet is bent downward and bending fails, as shown in Figure 64. It is observed that after the radial crack, a circumvention crack forms and the ice sheet breaks into small wedge-shaped pieces with lengths ranging from 3 to 12 times the ice thickness. This is a similar ratio to that presented in ISO 19906 stating that the ratio of the broken ice piece length to thickness is 3~10. Underneath the structure, there are multiple collisions among broken ice pieces including the structure. Unlike a square-shaped Arctic Spar, an accumulation in front of the structure is rarely observed. The momentum of the broken ice pieces leads them to pass along both sides of the structure.

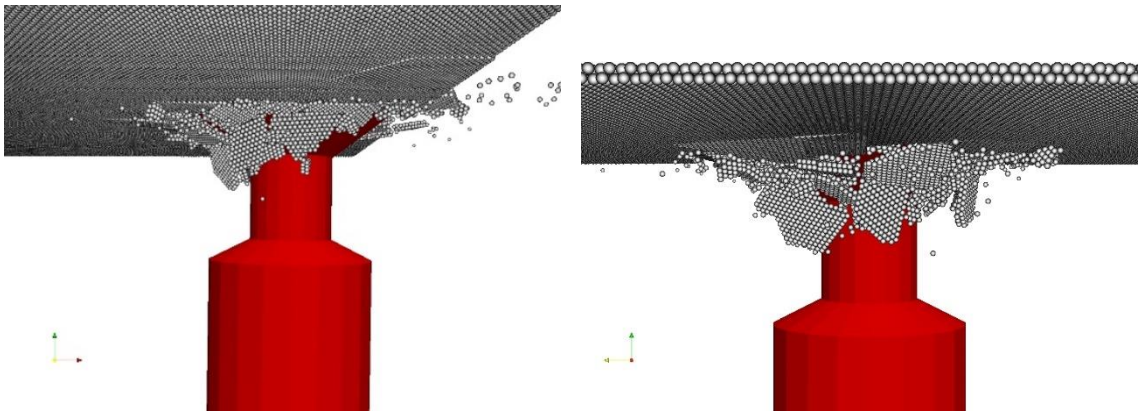

(a) (b)

Figure 64. Snapshots of ice bending failure from (a) side view and (b) front view

As shown in Figure 65 representing the distributed force diagram of an ice sheet, the interaction force between the particles is transferred through the edge or the area of the contact between the ice and the structure. It also found that after the initial bending breaking, the size of the ice pieces become much smaller due to the consecutive ice breaking. The excessive interaction force between the broken ice pieces is applied in the particles, and they lose their bond and become detached.

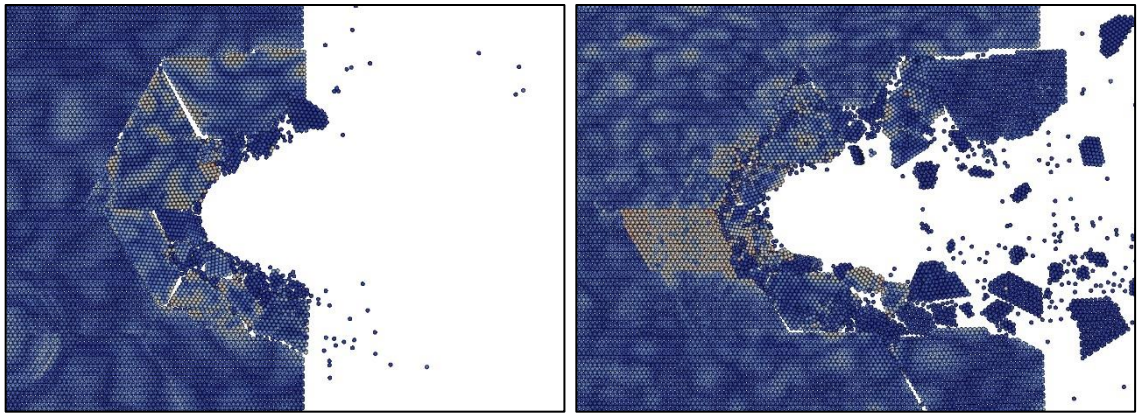

(a) t= 40 sec (b) t= 80 sec

Figure 65. Snapshots of ice failure propagation at different times

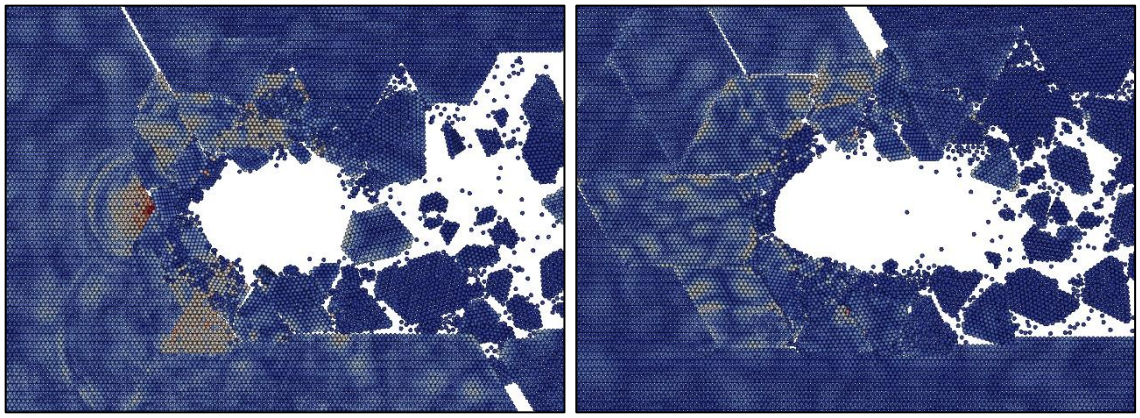

(c) t= 120 sec (d) t= 160 sec

Figure 67. Continued

Figure 66 ~ Figure 68 show the ice surge and heave forces, and the corresponding surge motion at the ice drift velocities of 0.1, 0.3 and 1.0 m/s. As a result, the three distinct structure motions are observed in three different cases. At the low velocity of 0.1 m/s, the ice force and structure surge motion show a similar trend. The structure drifts away with the moving ice sheet in the same direction. After the bending failure, the ice force suddenly decreases, and the structure moves back to the original location while experiencing multiple collisions with the ice sheet. Once the kinetic energy of the structure dissipates and becomes zero, then the structure drifts again with increasing ice force. At the velocity of 0.3 m/s, the structure shows sinusoidal motion with the surge natural frequency. Multiple peak ice forces are observed in one cycle of the surge motion. When the structure and ice move in the same direction, the submerged ice pieces in front of the structure increase the ice forces gradually. After ice bending failure, the impact force acting on the structure increases the structure velocity larger than that of the intact

ice sheet, and the ice force suddenly decreases due to the detachment. As a result, the broken ice pieces move away from the structure. When the structure moves forward by the mooring restoring forces and hits the ice sheet, multiple other peak ice forces are observed by ice bending failure. At the high ice velocity of 0.1 m/s, the surge motion shows a very small amplitude. The time-series of the corresponding ice forces becomes more random with a nearly constant variance over all of the force frequencies, as shown Figure 69. Due to the high ice drift velocity, the ice pile up below the structure is scarcely observed. In general, due to the 45-degree slope of the hull at the waterline, similar dynamic signals of the surge and heave ice forces with a similar magnitude are observed in three cases.

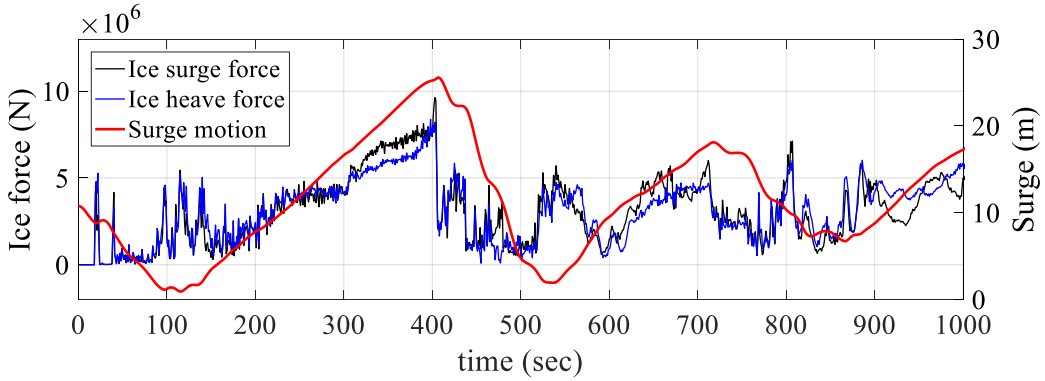

Figure 66. Ice force and surge motion in surge (v_ice = 0.1 m/s)

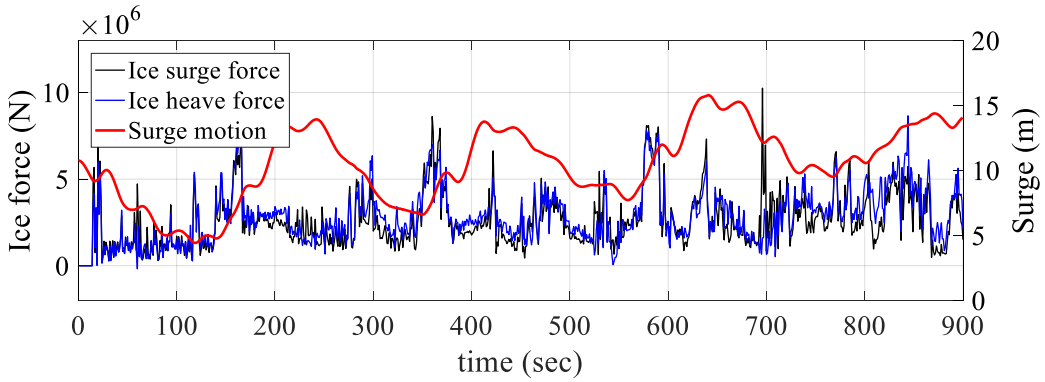

Figure 67. Ice force and surge motion in surge (v_ice = 0.3 m/s)

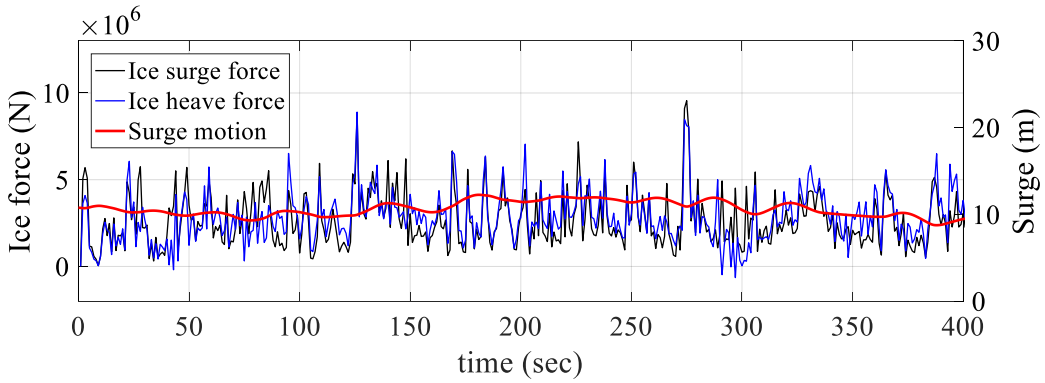

Figure 68. Ice force and surge motion in surge (v_ice = 1.0 m/s)

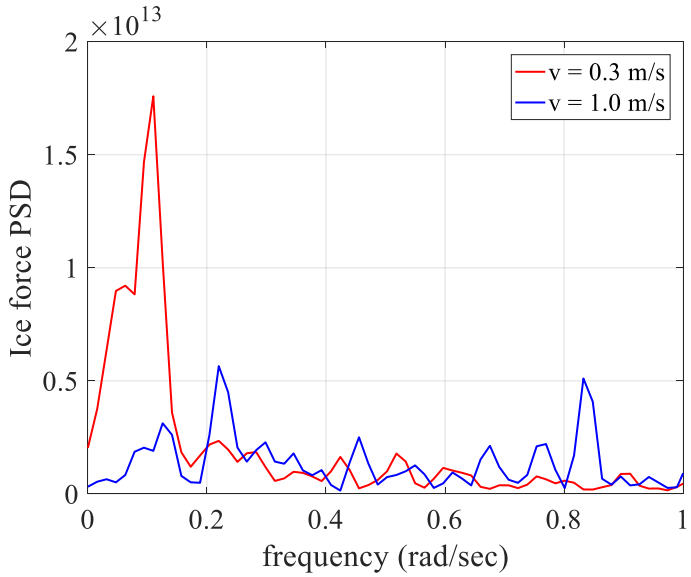

Figure 69. PSD of surge ice force at v_ice = 0.3 m/s and v_ice = 1.0 m/s

A comparison of the maximum, minimum, and standard deviation of surge ice forces is depicted in Figure 70, and tabulated in Table 18. The ice forces using analytical methods are calculated based on the equations by ISO 19906 with visual observation of numerical simulations using the DEM. The broken ice slides up to 12 m and pile-up rubble is not observed. Therefore, the factor of 1 is used for the rubble thickness in Ralston's method, whereas 40 degrees is used for the rubble angle in Croasdale's method. Since level ice interacting with a round-shaped Arctic Spar has a wide width to account for the 3D, the factor for the 3D effect in Croasdale's method is used. Compared to the analytical methods, the maximum ice force interacting with the floating Arctic Spar using the DEM is generally greater than those using the analytical methods because: 1) the analytical methods are derived for a fixed-structure which does not include the relative momentum of the structure and ice; 2) the structure angle increases during the interaction due to the pitch motion, which results in the increase of the ice force; and 3) the ice contact area with the structure increases when the heave motion is negative. The velocity effect on the ice force is rarely observed and the maximum forces in all of the cases have similar values.

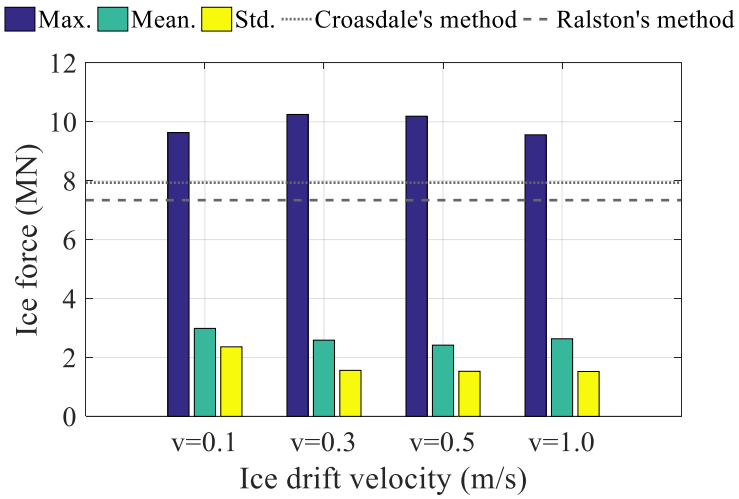

Figure 70. Ice force Statistics by varying the ice velocity

Table 18. Statistics of the ice force interacting with a round-shaped Arctic Spar

Ice velocity (m/s)	Max. (MN)	Mean (MN)	Std. (MN)
0.1	9.632	2.986	2.361
0.3	10.249	2.587	1.562
0.5	10.189	2.417	1.537
1.0	9.558	2.634	1.524

By taking advantage of a 6-DOF analysis, the 6-DOF ice forces and platform motions are depicted in Figure 71. The statistics of the 6-DOF platform motions are summarized in Table 19. Because contact between the level ice and the structure takes place asymmetrically and non-simultaneously, sway, roll, and yaw motions are observed. Since the ice moves in the surge direction, an almost positive pitch motion is recorded. Due to the eccentric forces on the structure, relatively large yaw motions are observed, compared

to the roll and pitch motions. The mean values of sway, roll, and yaw motions are almost equal to zero.

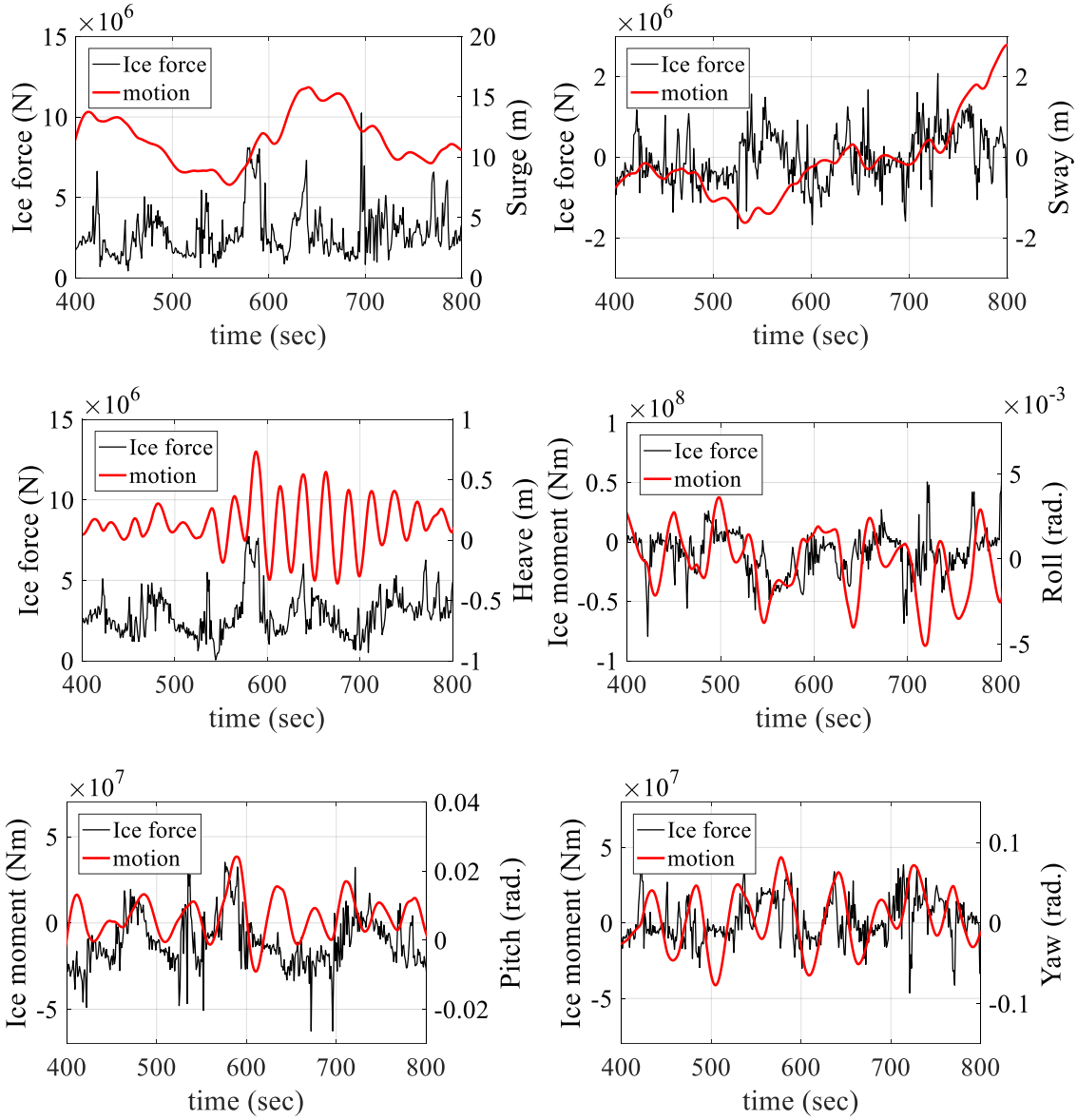

Figure 71. Time-series of the 6-DOF ice force and Artic Spar motions at v_ice = 0.3 m/s

Table 19. Statistics of the 6-DOF motions of a round-shaped Arctic Spar

Ice drift velocity (m/s)		Surge (m)	Sway (m)	Heave (m)	Roll (deg.)	Pitch (deg.)	Yaw (deg.)
0.1	Max.	25.564	2.382	1.718	0.314	1.054	4.792
	Min.	0.909	-1.041	-2.006	-0.259	-0.258	-4.028
	Mean.	11.393	-0.189	0.118	0.008	0.431	0.030
	Std.	6.590	0.691	0.332	0.087	0.308	1.292
0.3	Max.	15.793	2.788	1.718	0.225	1.388	5.196
	Min.	4.425	-1.937	-2.006	-0.319	-0.573	-4.842
	Mean.	10.433	-0.224	0.133	0.003	0.356	-0.055
	Std.	2.838	0.949	0.336	0.117	0.337	2.032
0.5	Max.	15.433	2.035	1.775	0.391	1.277	5.583
	Min.	6.833	-1.879	-2.006	-0.354	-0.493	-3.894
	Mean.	10.088	-0.391	0.109	0.013	0.342	0.127
	Std.	2.068	0.721	0.500	0.133	0.308	2.125
1.0	Max.	12.260	2.388	1.926	0.302	0.943	4.644
	Min.	8.755	-0.316	-2.006	-0.372	-0.183	-4.239
	Mean.	10.660	0.650	0.130	-0.026	0.363	0.284
	Std.	0.863	0.766	0.597	0.118	0.221	1.727

The mooring top tension of mooring line #8 is presented in Figure 72. At the low ice velocity, a large mooring force is observed, which is caused by the large surge motion (Figure 66). Due to the smaller motion at high velocity, the variation of mooring forces is also small. The mean force is almost identical over all of the velocities.

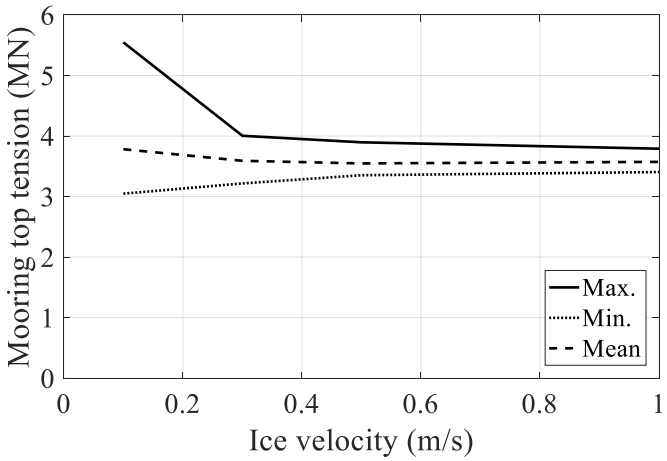

Figure 72. Mooring top tension of line #8 with varying ice velocity

4.5 Conclusion

The fully-coupled ice-structure-mooring interaction is numerically investigated by coupling the two programs, LIGGGHST and CHARM3D. The DEM method is used to model level ice with an assembly of multiple spherical particles, and the fracture of level ice is modeled by employing the parallel bonding method. The 6-DOF ice forces obtained by the DEM are inputted into CHARM3D to solve the 6-DOF platform motions and mooring dynamics. To determine the ice bonding strength, a numerical 3-point beam test is performed with the given ice flexural strength. Through the simulations of a fixed-type downward conical structure in level ice, the estimated ice force by the DEM is systematically validated through comparisons with the experimental data. Two Arctic Spar models are numerically simulated by varying the ice drift velocity, and the results

are visually and statistically discussed. The numerical simulations reveal the following conclusions:

- The numerical 3-point beam bending test using the DEM is performed to determine the bonding strength between particles. The pre-calculated force corresponding to the ice flexural strength is applied on the middle of the beam. Due to the deflection of the beam, considerable tension is applied on the bottom and substantial compression is applied on the top. After the internal stress of the particles on the middle of beam exceeds the bonding strength, the beam fails by bending.
- The ice forces using the DEM and the experiments are reasonably well matched, showing a similar magnitude and frequency. The time-series of the surge ice force shows a typical "saw-tooth" pattern by bending failure. Due to the symmetrical shape of the structure, a zero-mean value of the ice force is observed in the sway direction.
- A square-shaped Arctic Spar is simulated under the same conditions as in Chapter III. The ice-structure interaction shows similar behavior to that in Chapter III in that the intact ice sheet fails in bending, and the broken ice rotates and slides downward along the sloped structure. However, due to the large width of the structure and the square shape of the hull, the broken ice pieces are stacked in front of the structure, making the rubble pile. This rubble effect increases the ice force significantly. Therefore, = modified theoretical methods are used to compare the ice force. The results show that they are reasonably well matched.

- A round-shaped Arctic Spar is simulated under more realistic conditions without any assumptions. Based on the visual observations, the broken ice length is 3 to 12 times the ice thickness, which is in a similar range to ISO 19906. A radial crack is first formed, and a citrullination crack follows. Consecutive ice breaking of the broken ice pieces is observed, after intact ice breaking. Unlike a square-shaped Arctic Spar, rubble pile-up is not observed.
- Three distinct motions of a round-shaped Arctic Spar are observed. At a low ice velocity, the structure slowly drifts in the same direction as the moving ice. The time-series of the surge motion shows a similar trend to that of the ice force, which indicates a quasi-static response. At the velocity of 0.3 m/s, the structure motion is amplified by the corresponding ice forces. The structure interacting with fast-moving level ice shows small motions due to the random ice force from the continuous breaking.
- The maximum mooring top tension decreases as the ice drift velocity increases. The variation also decreases with increasing ice velocity. At the low ice velocity of 0.1 m/s, the largest maximum tension induced by the large surge motion is observed.

CHAPTER V

NONLINEAR TIME-DOMAIN SIMULATION OF ARCTIC SPAR AND MATHIEU INSTABILITY

5.1 Introduction

One of the greatest challenges in developing the Arctic region is the severe environmental conditions caused by the presence of ice. To reduce the impact of ice, researchers have introduced a sloping wall concept, which allows the ice to fail in a flexural mode. For deeper Arctic water, a new Spar platform design, called Arctic Spar, has been proposed in various publications. (Chernetsov et al., 2006, 2008; Murray et al., 2009; Bruun et al., 2009, 2011; Sablok et al., 2011, Jochmann and Evers, 2014). Arctic Spar is characterized by its conical shape around the mean water level and a mooring/riser system that can be disconnected to avoid the impact of extreme ice. Because of the irregular hull shape at the waterline, the nonlinear effect becomes significant when there is either considerable platform motion or steep waves. These effects could result in nonlinear platform behavior with large amplified motion from resonance.

In a conventional Spar, the water plane area along the hull is a constant and the linear analysis is applicable to evaluate the global performance of a conventional Spar. However, in the case of an Arctic Spar, the nonlinear effects from its irregular hull shape would be significant if there is either a large amplitude floater motion or steep wave conditions.

Therefore, in this study, the nonlinear effects of an Arctic Spar are numerically investigated by introducing a partially nonlinear time-domain model that considers the time dependent hydrostatic restoring coefficient (HC) and Froude-Krylov (FK) forces. During the simulation, the part of the structure underneath the instantaneous wave elevation is gridded in every time step, considering the platform's 6-DOF motions. In addition, the corresponding nonlinear HC and FK forces are computed for an instantaneous submerged structure. Through numerical simulations under multiple regular and irregular wave conditions, the nonlinear behavior of the Arctic Spar is clearly observed, but it is not shown in the linear analysis. In particular, it is found that because of the conical shape near the waterline, the nonlinear FK force plays an important role when the wave frequency is close to the heave natural frequency. In addition, the nonlinear HC causes the structure's unstable motion at a half of heave natural period, which is Mathieu instability. For comparison, the equations of the motion in the heave and pitch directions are derived as a form of the Mathieu equation. The numerical results are discussed by varying the wave parameters and are compared to the theoretical stability diagram. At the end, the dynamic performance of Arctic Spar under a 100-year storm condition is discussed.

5.2 Literature Review

The effect of nonlinear hull shape on the performance of Arctic Spar has been researched by many researchers. Dalane et al. (2012) presented an exact analytic

expression for the metacentric height in the open water condition without waves and calculated the coupled hydrostatic pitch restoring moments for shallow draught conical floaters. The nonlinearity effect on a floater's motion was investigated by free-decay tests and compared to linear and Haslum's hydrostatic modelling. Cao et al. (2010) presented a nonlinear numerical method for arbitrary hull shapes. They accessed the three types of offshore platforms (a cylindrical buoy, a conical arctic buoy, and FPSO) in regular waves as examples, and a significant nonlinear effect was observed. Guerinel et al. (2011) developed a numerical algorithm to take nonlinear HC and FK forces into account and investigated a freely floating cone-shaped structure. They found that in both regular and irregular wave tests, the total wave forces and corresponding motions clearly showed nonlinearity. They also compared the results to the one obtained by the linear analysis and found that there were considerable differences. Kumar and Nallayarasu (2016, 2017) performed both numerical and experimental tests for various hull shape Spars including a buoy-form Spar.

This nonlinear hull geometry may cause significant instable motions of the floater. One of the well-known instable phenomena is Mathieu instability induced by the time-varying stiffness. In the linear analysis, the fundamental motion equation is derived from a constant equilibrium position, and all dynamic parameters such as mass, damping, stiffness, and force are linearized, thus this nonlinear phenomenon cannot be captured. Therefore, the nonlinear analysis is necessary to demonstrate the nonlinear behavior of a floating platform.

The nonlinear behavior of a classic Spar has been investigated numerically and experimentally by many researchers. They have observed unstable pitch motion of Mathieu-type instability, where the pitch natural period was twice that of the heave natural period. Previous literature about Mathieu instability has presented many insightful findings for a classic Spar. In particular, Koo et al. (2004) conducted numerical tests for a classic Spar with different damping models and concluded that the additional damping plays an important role in suppressing Mathieu instability. Jingrui et al. (2010) derived the heave/pitch coupled equation of motion for a conventional Spar and found that nonlinear motion may occur at the wave period close to the sum of heave and pitch natural frequencies. Yang et al. (2015) investigated the parametric instabilities of Spar platforms in irregular waves and provided several suggestions to avoid the parametric pitch resonance.

The effect of various hulls of Spar platforms on Mathieu instability has also been investigated. Haslum et al. (1999) studied the five alternative hull shapes and observed the heave and pitch instability using simplified methods. Wan et al. (2015) performed experimental tests under survival conditions for a Spar-type floating offshore wind turbine equipped with a torus-shape wave energy converter (WEC). When the torus was locked to the Spar at the mean water level, the heave-induced pitch instability occurred at the wave period equal to half of the pitch natural period. Nallayarasu and Kumar (2017). also conducted numerical and experimental tests and compared three Spar models under regular wave tests. However, the last two papers above only considered the Mathieu

instability in the pitch direction but not the heave direction, caused by the irregular hull shape near the waterline.

5.3 Numerical Approach

5.3.1 Nonlinear hydrostatic stiffness model

In a linear analysis, restoring stiffness is linearized about the mean water level with the assumption that the body motion is small, and the waterplane area is constant along the hull near the waterline. However, with large wave heights and body motions, the effect of time-varying nonlinear restoring stiffness is significant. Furthermore, for Arctic Spar, the waterplane area changes a lot with heave motions, which means time-dependent HC with respect to the instantaneous body position needs to be used. We adopt the method used by Guerinel et al. (2011) and extend it to the 6-DOF floater motions. Then, the time dependent HC can be defined as:

$$
\begin{aligned}
C(3,3) &= \rho g \sum_{i=1}^{N} \left(n_{3,i} S_{w,i}(t) \right) \\
C(3,4) &= \rho g \sum_{i=1}^{N} \left((x_{2,i}(t) - x_{0_2}(t)) n_{3,i} S_{w,i}(t) \right) \\
C(3,5) &= -\rho g \sum_{i=1}^{N} \left((x_{1,i}(t) - x_{0_1}(t)) n_{3,i} S_{w,i}(t) \right) \\
C(4,4) &= \rho g \sum_{i=1}^{N} \left((x_{2,i}(t) - x_{0_2}(t))^2 n_{3,i} S_{w,i}(t) \right) + \rho g \forall(t) x_{b_3}(t) - mg x_{g_3}(t) \\
C(4,5) &= -\rho g \sum_{i=1}^{N} \left((x_{1,i}(t) - x_{0_1}(t))(x_{2,i}(t) - x_{0_2}(t)) n_{3,i} S_{w,i}(t) \right) \\
C(4,6) &= -\rho g \forall(t) x_{b_1}(t) + mg x_{g_1}(t) \\
C(5,5) &= \rho g \sum_{i=1}^{N} \left((x_{1,i}(t) - x_{0_1}(t))^2 n_{3,i} S_{w,i}(t) \right) + \rho g \forall(t) x_{b_3}(t) - mg x_{g_3}(t) \\
C(5,6) &= -\rho g \forall(t) x_{b_1}(t) + mg x_{g_1}(t)
\end{aligned}
\tag{35}
$$

where

$$
\forall(t) = \sum_{i=1}^{N} \left((n_{j,i}(x_{j,i} - x_{0_j}(t)) S_{w,i}(t) \right)
$$

$$
x_{b_j}(t) = \frac{-1}{2\forall(t)} \sum_{i=1}^{N} \left(n_{j,i}(x_j - x_{0_j})^2 S_{w,i}(t) \right)
$$

where $S_{w,i}(t)$ is the area of the wetted surface panel, N is the total number of wetted surface panels, $x_{j,i}$ and $n_{j,i}$ are the centroid and normal vectors, x_{0_j} is the origin of a body coordinate, x_{b_j} is the center of buoyancy, x_{g_j} is the center of mass, m is the mass of a structure, g is the gravitational acceleration, $\forall(t)$ is the submerged volume, ρ is the density of water, i denotes the ith panel, and j denotes the x-, y-, and z-dimensions.

5.3.2 Partially nonlinear wave forces

The nonlinear wave forces on Arctic Spar are considered throughout the time-domain numerical simulation. The wave force is divided into three components as follows.

$$F_{wave} = F_{linear\_diff} + F_{nonlinear\_FK} + F_{nonlinear\_drag} + F_{convolution} \tag{36}$$

where F_{wave} is the total wave force, F_{linear_diff} is the linear diffraction force caused by disturbed incident waves, $F_{nonlinear\_FK}$ is the nonlinear FK force, $F_{nonlinear\_drag}$ is the nonlinear viscous drag force, and $F_{convolution}$ is the radiation damping force. The linear diffraction force is calculated based on the first-order 3D diffraction/radiation potential theory. During the time-domain simulation, the diffraction force remains linear. The nonlinear FK Force caused by undisturbed incident wave's pressure is calculated, considering the instantaneous submerged structure position. The structure mesh is re-gridded using the Euler angles method at every time step, considering the instant body translations and rotations. Then, the nonlinear FK force is evaluated by integrating the incident-wave pressure on the instantaneous submerged-body surface. The equation of the nonlinear FK wave force is as follows:

$$
\begin{aligned}
&F_{nonlinear\_FK}(t) = -\sum_{i=1}^{N} p_i n_{j,i} S_{w,i}(t) \qquad j = 1,2,3 \\
&M_{nonlinear\_FK}(t) = -\sum_{i=1}^{N} p_i (r \times n)_{j-3,i} S_{w,i}(t) \qquad j = 4,5,6 \\
&\textit{where} \\
&p_i = \begin{cases} \rho \dfrac{\partial \varphi_0}{\partial t} & \textit{for } x_{3,i} \le 0 \\ p_i(x_{3,i} = 0) & \textit{for } x_{3,i} > 0 \end{cases}
\end{aligned}
\tag{37}
$$

where p_i is the pressure by incident waves, r is the position vector from the body origin to the centroid of the i^{th} panel, and φ_0 is the velocity potential for incident waves. Above the mean water level, the dynamic pressure is evaluated using the vertical stretching method such that the pressure above the mean water level is equal to the pressure at the waterline.

The nonlinear viscous drag force is evaluated by the Morison's equation in Eq. (38).

$$
F_{nonlinear\_drag} = \frac{1}{2} C_d \rho A (u - \dot{x}) |u - \dot{x}| \tag{38}
$$

where C_d is the drag coefficient, A is the projected area, u and $\dot{x}$ are the instantaneous wave particle and body velocities normal to the projected area at the instantaneous body position. The nonlinear forces and moments induced by the viscous drag are calculated by integrating the forces on the discrete elements using the 6-point Gaussian quadrature

integration. The fourth component $F_{convolution}$ is associated with radiation (wave-making) damping and explained in the next sub-section.

5.3.3 Hydrodynamic coefficients in the time-domain

The hydrodynamic coefficient is first calculated from the frequency-domain 3D diffraction/radiation panel program and the results are converted to the form used in time-domain simulation. Based on the Kramers–Kronig relationship, the radiation damping force can be expressed using the convolution integral form. The added mass at infinite frequency is a function of the retardation function and remains constant as follows:

$$
\begin{aligned}
F_{convolution}(t,\dot{x}) &= -\int_{-\infty}^{t} R(t-\tau)\dot{x}(\tau)d\tau \\
R(t) &= \frac{2}{\pi}\int_{0}^{\infty} b(\varpi)\cos(\varpi t)d\varpi \\
M_{add}(\infty) &= M_{add}(\varpi) - \int_{0}^{\infty} R(t)\cos(\varpi t)dt
\end{aligned}
\qquad (39)
$$

where $F_{convolution}$ is the radiation damping force, $\dot{x}$ is the 6-DOF velocities of the floating body, $R(t)$ is the retardation function, $b(\varpi)$ is the linear radiation damping matrix at frequency, ϖ, and $M_{add}(\infty)$ is the added mass at infinite frequency.

5.3.4 Equation of Arctic Spar 6-DOF motions

The time dependent hydrostatic stiffness matrix, $C_{hydro}(t)$, is considered and the nonlinear wave force is separated into the linear diffraction, nonlinear FK, nonlinear

viscous drag, and convolution damping forces. Then, the equation of motion can be written as:

$$[M + M_{add}(\infty)]\ddot{x}(t) + \left[C_{hydro}(t) + K_{mooring} \right] x(t) = F_{linear\_diff}(t) + F_{nonlinear\_FK}(t) + F_{drag}(t) + F_{convolution}(t) \quad (40)$$

To solve the 6-DOF dynamic equation of motion, a combination of the Adams-Bashforth and Adams-Moulton methods is used with a constant time step for numerical integration.

The present approach is called the body-nonlinear method with nonlinear FK force. The fully nonlinear computation including fully nonlinear free-surface and body-surface conditions is extremely complex and time consuming since the instantaneous free surface and large-size matrix equation need to be updated and solved at each time step. Therefore, the present approach is not fully nonlinear but the most important body nonlinearity is included to investigate the resulting MI phenomenon.

5.4 Analytical Investigation for the Mathieu Equation in Heave and Pitch Motions

For floating structures, the waterplane area (A_w), mainly contributes to the heave restoring stiffness, represented by $\rho g A_w$. For Arctic Spar, the time varying restoring coefficient in heave can be calculated based on the time dependent water plane area, which

changes with heave displacements. For the 45-degree slope case, the waterplane area can be calculated as follows:

$$\rho g A_w = \rho g \pi \left((r_o - (x_3(t) - \eta(t))^2 - r_i^2 \right) = \rho g \pi (r_o^2 - r_i^2 + 2 r_o \eta(t) - 2 r_o x_3(t) + (x_3(t) - \eta(t))^2) \quad (41)$$

where r_o and r_i are the outer and inner radius of the water plan area, respectively, $x_3(t)$ is the heave motion, and $\eta(t)$ is the wave elevation. Since the heave motion and wave elevation are relatively small compared to the radius of the waterplane area, the last high-order term is ignored for simplicity. Then, with the assumption of a sinusoidal wave elevation, $\eta(t) = \bar{\eta} \cos \omega t$, the equation of heave motion can be written as:

$$(M + M_{added}) \ddot{x}_3 + C_{33} \dot{x}_3 + \rho g \pi (r_o^2 - r_i^2 + 2 r_o \bar{\eta} \cos \omega t) x_3 - 2 \rho g \pi r_o x_3^2 = 0 \quad (42)$$

where C_{33} is the damping coefficient, and $\bar{\eta}$ is the amplitude of the wave elevation. This is the form of a nonlinear Mathieu equation including the quadratic term. For the range of incident wave frequencies considered here (0.28-0.45 rad/s), the phase of heave response is 180-degree out of phase of that of incident wave. Then, the last two terms of Eq. (42) can be combined as

$$(M + M_{added}) \ddot{x}_3 + C_{33} \dot{x}_3 + \rho g \pi (r_o^2 - r_i^2 + 2 r_o (\bar{\eta} + \bar{x}) \cos \omega t) x_3 = 0 \quad (43)$$

Similarly, the pitch motion equation coupled with the heave motion can be derived by considering the time-varying displaced volume, ∇ and metacentric height, $\overline{GM}$. A detailed derivation of the coupled pitch equation of motion is given in the paper by Koo et al. (2004).

$$(I_{55} + A_{55})\ddot{x}_5(t) + C_{55}\dot{x}_5(t) + \rho g \nabla(\overline{GM}_0 - \frac{1}{2}\bar{x}_3 \cos \omega t) x_5(t) = 0 \qquad (44)$$

where $\overline{GM}_0$ is the metacentric height when the platform is at rest.

The parameters in the form of Mathieu's equation are defined in Table 20. For simplicity, the linear Mathieu equation is considered for the stability diagram for the heave motion. Hill's infinite determinants method is applied to obtain the boundaries of the instability regions with parameters, α and β. α is defined as the square of a ratio between the natural frequency of motions and the encounter wave frequency. If β increases, the possibility of the system being unstable increases. Therefore, with larger heave motion, the possibility of Mathieu instability increases more. Koo et al. (2004) described the damping effect, which shifts the critical line to the upper level and enlarges the stable regions, as shown in Figure 73. Among the series of unstable regions, the primary unstable region is less affected by damping, which means that the instability most likely occurs when α is equal to 0.25. In Figure 73, the last quadratic term of Eq. (43) is not included in the Hill's stability analysis.

Table 20. Parameters in Mathieu's equation

	Heave motion equation	Pitch motion equation
α	$\frac{\rho g\pi(r_o^{\,2}-r_i^{\,2})}{(M+M_{added})\omega^2}=\frac{\omega_3^{\,2}}{\omega^2}$	$\frac{\rho g\nabla\overline{GM}}{(I_{55}+A_{55})\omega^2}=\frac{\omega_5^{\,2}}{\omega^2}$
β	$\frac{2\rho g\pi r_o(\overline{\eta}+\overline{x})}{(M+M_{added})\omega^2}$	$\frac{0.5\rho g\nabla\overline{x}_3}{(I_{55}+A_{55})\omega^2}$
c	$\frac{C_{33}}{(M+M_{added})\omega}$	$\frac{C_{55}}{(I_{55}+A_{55})\omega}$

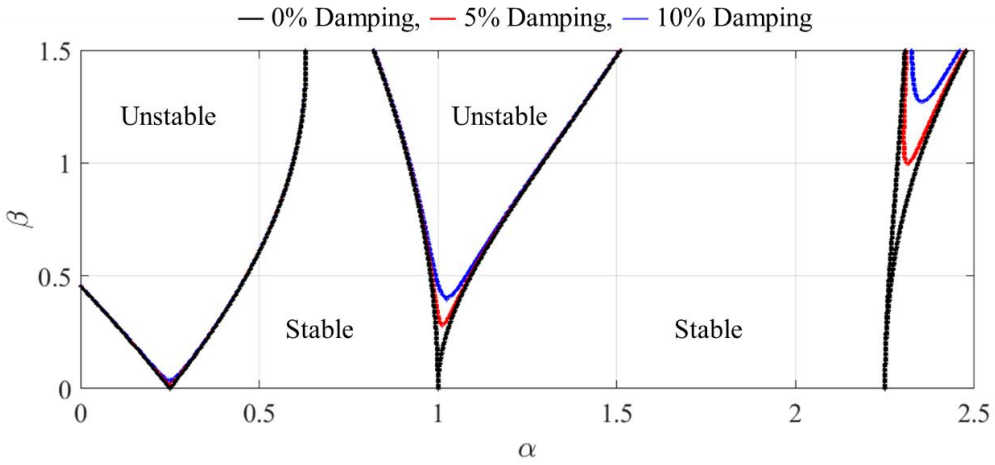

Figure 73. Mathieu instability diagram with damping

5.5 Arctic Spar Model for Case Studies

The Arctic Spar model is adopted from Murray et al. (2009). It is a floating Spar with a conical shape near the waterline. In their work, the total mass includes the moonpool mass for simplicity. However, in this study, since the entire exact structure should be modeled for the calculation of the nonlinear HC and FK force, the system parameters of the Arctic Spar is modified accordingly so the moonpool mass can be excluded. Because

of the open bottom, the total heave mass including the added mass in the new model is smaller than the original Spar model, whereas the total surge and pitch mass are the same. The Helmholtz frequency for the moonpool resonance is about 1.17 rad/sec, which is out of the typical peak frequency in a random sea state. Therefore, the influence of the moonpool on the hydrodynamic of the structure is ignored. The structural properties are tabulated in Table 21. The dimension of the Spar is the same as the original platform, as depicted in Figure 74.

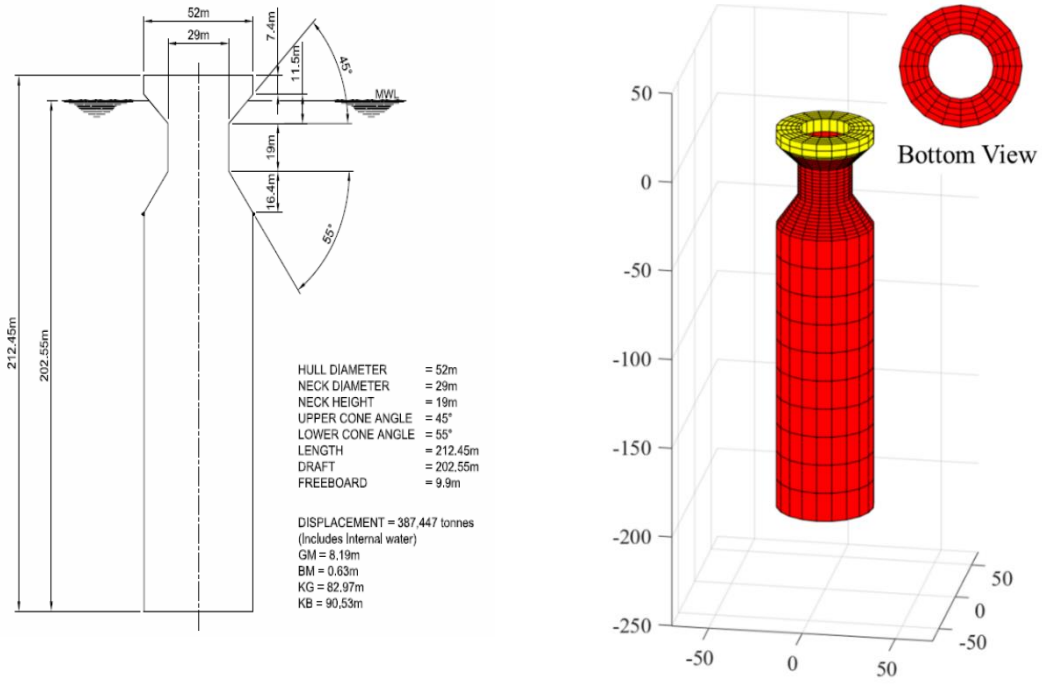

(a) Prototype Arctic Spar Model (Murray et al. (2009))**

(b) Numerical Arctic Spar Model

Figure 74. Arctic Spar geometries for study

** Figure 74 (a) is reprinted with permission from "Model Tests on a Spar in Level Ice and Ice Ridge Conditions" by Murray et al., 2009. 28th International Conference on Ocean Offshore and Arctic Engineering., Copyright [2009] by ASME

The viscous drag along the hull is modeled by Morison members and heave plates. The Arctic Spar is vertically divided into three Morison members for the horizontal drag force. The vertical drag forces on the bottom and sloped surfaces are modeled as Morison plates. For simplicity, the drag coefficients for Morison members and plates are chosen as 1.0 and 5.0, respectively. The inertia coefficient is set to zero because its contribution is already accounted for in the added mass in Eq. (39).

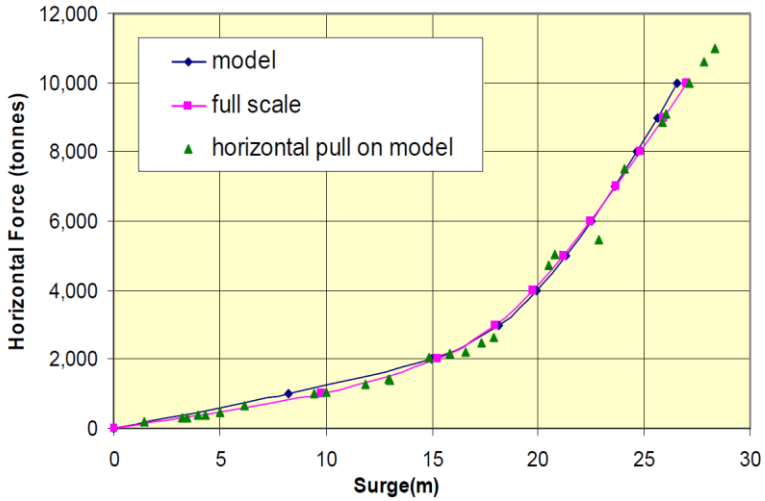

Figure 75. Surge restoring force by mooring lines (Murray et al. (2009))***

*** Figure 75 is reprinted with permission from "Model Tests on a Spar in Level Ice and Ice Ridge Conditions" by Murray et al., 2009. 28th International Conference on Ocean Offshore and Arctic Engineering., Copyright [2009] by ASME

Table 21. Arctic Spar properties

	Unit	Original Platform	Platform without Moon pool mass
Heave (M)	kg	3.87E+08	2.61E+08
Heave (M+A)	kg	4.37E+08	3.06E+07
Pitch (I)	$kg*m^2$	1.95E+12	1.45E+12
Pitch (I+IA)	$kg*m^2$	2.77E+12	-
ryy	m	70.93	74.64
KB	m	90.53	85.72
KG	m	82.97	74.11
Water Plane Area	m^2	1.13E+03	1.13E+03
Displacement	N	3.80E+09	2.56E+09
Origin of Body Coordinate	-	(0, 0, -119.58)	(0, 0, 0)

Mooring lines are modeled with a 6x6 stiffness matrix. Static-offset tests performed by Murray et. al. (2009) are utilized to calculate the components in the mooring stiffness matrix. In the surge, the horizontal mooring force linearly increases up to 15 m displacement. After that, the force exponentially increases with increasing displacement, following the approximated equation;

$$y = 272.47\exp(0.1472x) \tag{45}$$

One can obtain the mooring stiffness by differentiating Eq. (7). Therefore, the mooring stiffness in the surge and sway is a constant of 1.3 MN/m up to 15 m off-set. If the surge or sway motion exceeds 15 m, the time-varying mooring stiffness is considered,

following Eq. (7). The mooring moment for the roll and pitch is 490MN/rad given by Murray et. al. (2009). Since this paper aims to investigate the nonlinear effect of hull geometry, the location of the fairlead is shifted to the center of gravity so the harmonic motion can be obtained in the free decay tests. The heave and yaw mooring stiffness is ignored in this study. Since there is no information about the heave restoring stiffness, it is assumed to be small and negligible. The linear mooring stiffness with respect to the body origin is given in Eq. (46).

$$K_{mooring} = \begin{pmatrix} 1.307MN/m & 0 & 0 & 0 & -155.6MN/rad & 0 \\ 0 & 1.307MN/m & 0 & 155.6MN/rad & 0 & 0 \\ 0 & 0 & 0 & 0 & 0 & 0 \\ 0 & 155.6MN \cdot m/m & 0 & 19.0GN \cdot m/rad & 0 & 0 \\ -155.6MN \cdot m/m & 0 & 0 & 0 & 19.0GN \cdot m/rad & 0 \\ 0 & 0 & 0 & 0 & 0 & 0 \end{pmatrix} \quad (46)$$

5.6 Numerical Results and Discussion

In this study, the numerical test in the time domain is achieved by extending the existing program, CHARM3D. The program is capable of simulating the fluid-structure interaction, considering the nonlinear mooring and viscous effects. The hydrodynamic coefficients (added mass, radiation damping, and diffraction wave force) are obtained by the 3D diffraction/radiation panel method and input into this program. The current development of nonlinear HC and FK forces are updated in every time step.

Three different analyses are conducted in the time domain. The first analysis (NA1) is the linear analysis, which means that all dynamic components (mass, damping, stiffness, and force) are derived based on the linear theory. The second analysis (NA2) includes the time-varying nonlinear HC and FK forces. In the third analysis (NA3), only the nonlinear HC is considered without nonlinear FK force compared to the second approach. Since the parametric resonance is caused by the sinusoidally-varying stiffness coefficient, it is expected that the second and third analyses show the Mathieu instability.

Table 22. Numerical analysis cases

	NA1	NA2	NA3
Restoring force	Linear	Nonlinear	Nonlinear
Foude-Krylov force	Linear	Nonlinear	Linear
Waterplane Area	Constant	Varying	Varying

5.6.1 Nonlinear Coupled Restoring Stiffness

Nonlinear coupled restoring stiffness under the open water condition is investigated by static analysis. In Figure 76, the nonlinear heave restoring stiffness significantly changes with the heave displacement due to the large change in the water plan area while the linear restoring stiffness remains constant. The influence of a pitch motion on the heave restoring stiffness is not significant. Figure 77 shows a nonlinear relationship of the pitch restoring moment against the heave and pitch motions. The more coupling effect by the heave motion in pitch restoring stiffness is more clearly observed than that by the pitch motion in the heave restoring stiffness. Since the upper part of an Arctic Spar has more

volume than the lower part, the change in the pitch restoring moment becomes much larger when the platform moves downward. In the heave and pitch restoring stiffness, the stiffness hardens as the platform moves down and softens with the positive platform's heave displacement. These results are in good agreement with those presented in previous papers. (Mulk et al., 1994; Cao et al., 2010; Dalane et al., 2012). To validate the numerical algorithm, the heave restoring stiffness is compared to the exact solution by varying the heave motion. For simplicity, the pitch angle is set to 0 radian. As a result, the two types of restoring stiffness are well matched, as shown in Figure 78. The HC is compared to the one by linear analysis, and it is observed that the differences increase with the heave motion. In the time-domain simulation, these two types of stiffness are expected to be very nonlinear due to the instantaneous wave elevation effects.

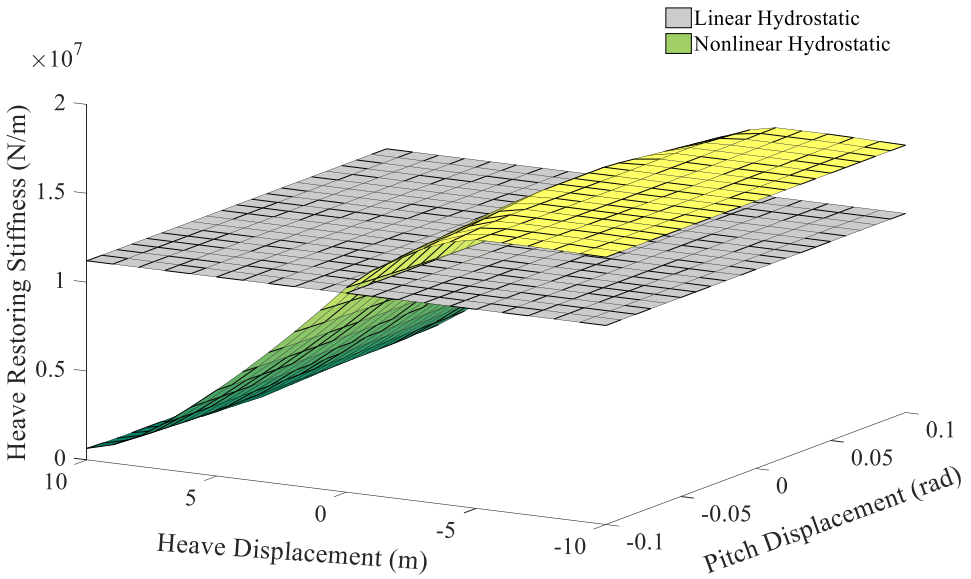

Figure 76. Heave restoring stiffness (Open water, No wave)

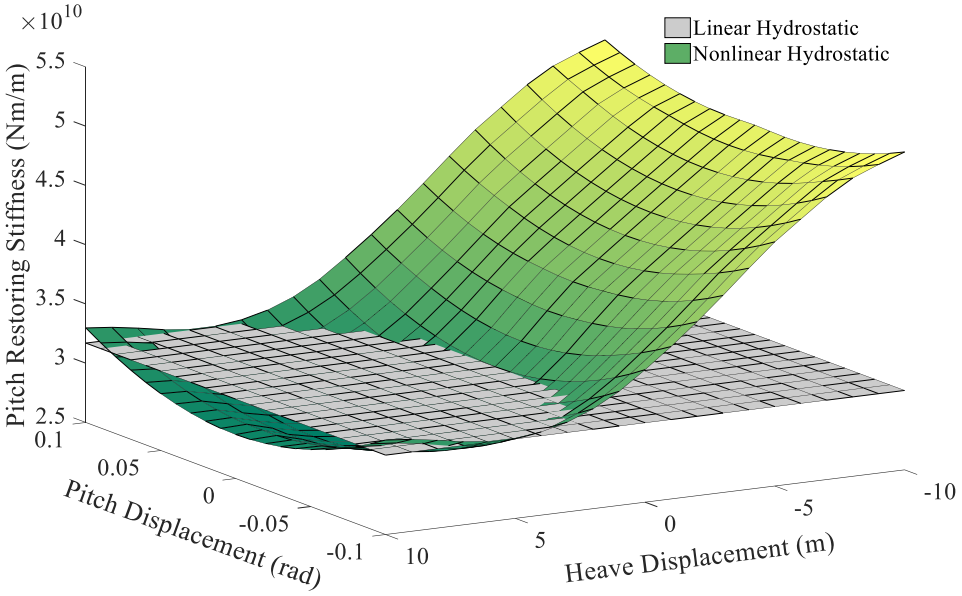

Figure 77. Pitch restoring stiffness (Open water, No wave)

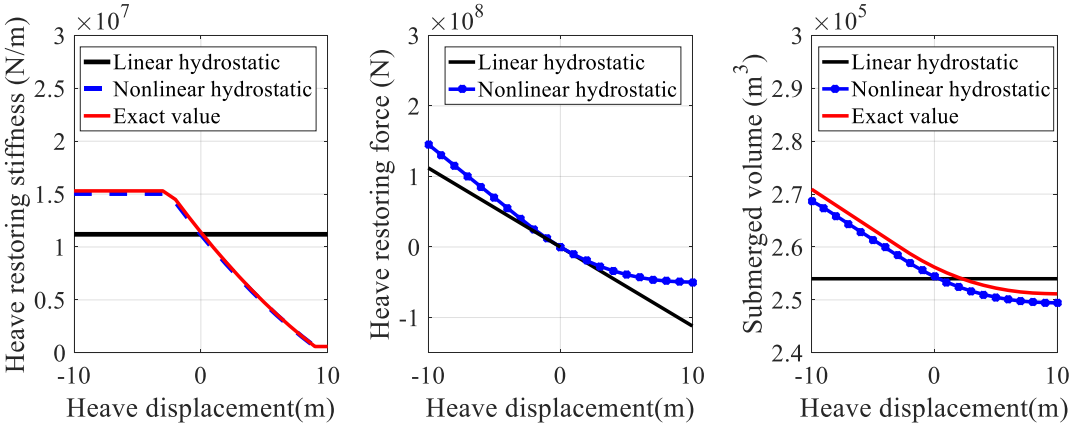

Figure 78. Heave restoring stiffness, force and volume
(0^0 pitch angle, Open water, No wave))

5.6.2 Hydrodynamic Coefficients

The added mass, radiation damping, and diffraction forces are calculated based on the first-order velocity potential theory using the WAMIT program. The convergence test is conducted to determine the optimized number of panels for the simulation. The 1 wave heading of 0 degrees and 28 wave frequencies ranging from 0.01 rad/sec to 5 rad/sec are considered. The added mass for 6-DOF is presented in Figure 79. Note that the rotational inertia is calculated with respect to the origin of the body coordinate (0, 0, 0).

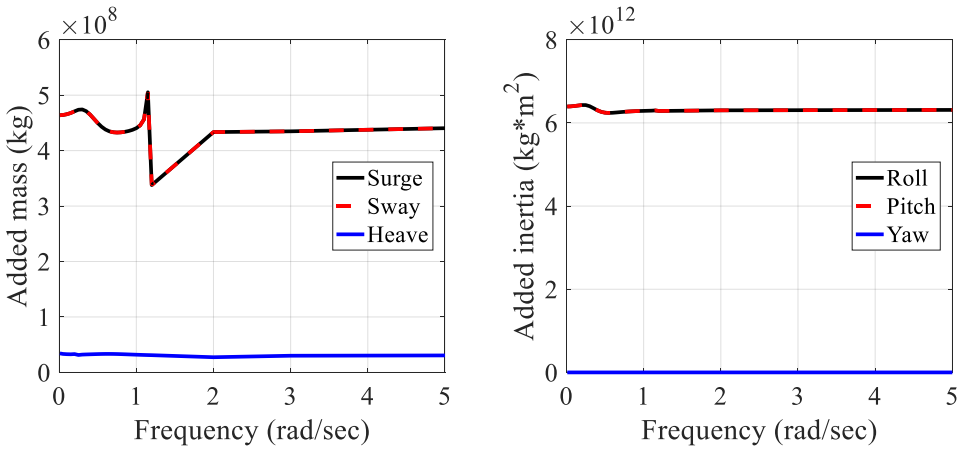

Figure 79. Added mass in frequency domain

5.6.3 Free Decay Tests

Numerical free decay tests are performed to identify the natural frequency and damping ratio of the entire system. The structure is initially translated into 15 m, 7 m, and 0.1 radian in the surge, heave, and pitch free decay tests, respectively. The drag coefficient of 1.0 is applied for the hull in the horizontal direction, and that of 5.0 is used for the bottom plate and sloped surfaces in the vertical direction.

Figure 80shows the time-series of the free-decay test results. Generally, since the wave force is not considered in the free-decay test, the analysis configurations for NA2 and NA3 are exactly the same, which results in the same time-series. In surge, the motions in the three cases are identical with the same natural frequency because the stiffness and total mass are the same in the surge direction. In heave, NA1 decays over time with the same period of 32 sec. However, NA2 and NA3 show a nonlinear decaying motion due to the inverted conical shape around the mean water level. When the heave displacement is large, the natural period is larger, which means the heave stiffness softens with increasing displacement. As the displacement decreases and the number of oscillations increases, the nonlinearity becomes insignificant and, in the end, the decaying period converges to the same decaying period of NA1, as shown in Table 23. In the pitch direction, NA1, NA2, and NA3 show a similar trend and natural periods. The slight difference in pitch is attributed to a change in the center of buoyancy and nonlinear restoring moment. The pitch stiffness hardens with increasing pitch motion. However, the nonlinear effect due to the inverted conical hull shape is not more significant than that in the heave case. To calculate the damping ratio, the logarithmic decrement method is employed. Table 24 indicates the damping ratio for the three cases: surge, heave, and pitch directions.

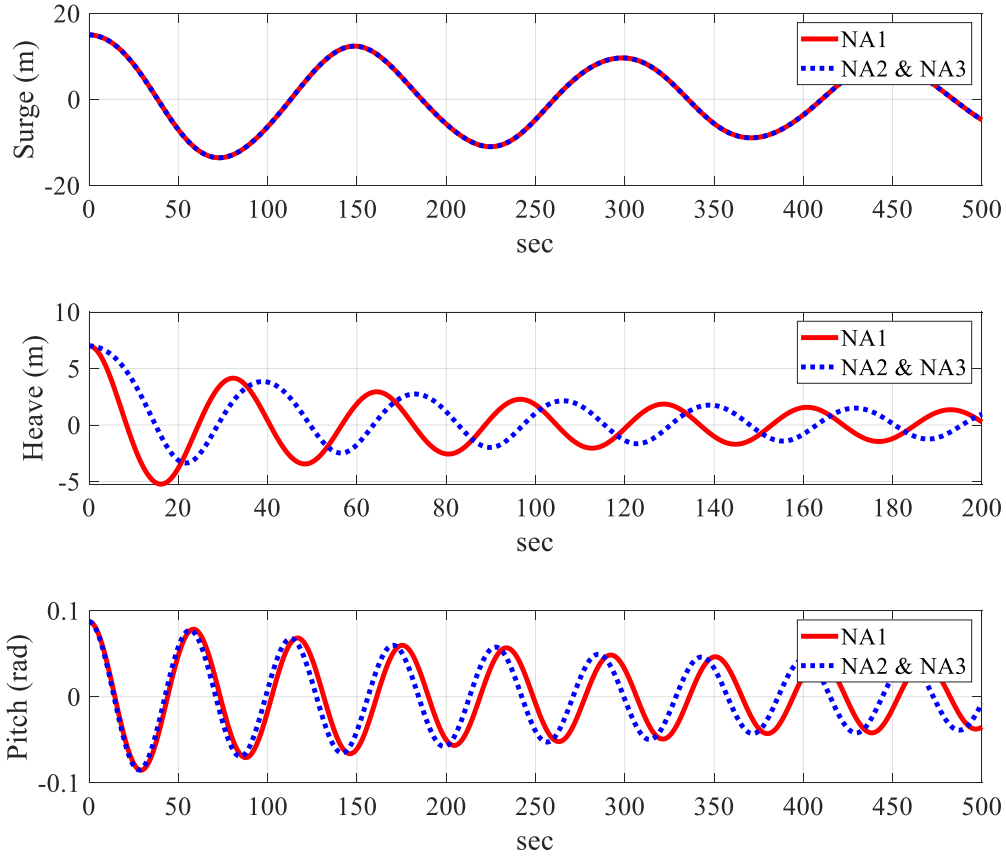

Figure 80. Free decay tests in surge, heave, and pitch (Cd=1.0, Cz=5.0)

Table 23. Decaying periods in heave and pitch free decay tests

# of Oscillation		1	2	3	4	5	6
Surge	NA1	148.50	150.00	147.00	151.50	146.50	151.50
	NA2 & NA3	148.50	150.00	147.00	151.50	146.50	151.50
Heave	NA1	32.25	32.19	32.16	32.13	32.12	32.12
	NA2 & NA3	38.90	34.11	33.21	32.80	32.60	32.46
Pitch	NA1	58.50	58.20	58.70	58.35	58.45	58.55
	NA2 & NA3	56.45	56.55	57.25	57.35	57.55	57.75

Table 24. Damping ratio with Cd=1, Cz=5

	Total damping (%)		Viscous damping (%)		Non-viscous-drag damping (%)	
	NA1	NA2 & NA3	NA1	NA2 & NA3	NA1	NA2 & NA3
Surge	3.05	3.05	2.64	2.64	0.41	0.41
Heave	6.23	6.71	6.15	6.53	0.08	0.18
Pitch	1.84	1.89	1.47	1.77	0.37	0.12

5.6.4 Regular Wave Tests

A series of regular wave tests is conducted under multiple wave conditions. The wave height ranges from 1~6 m and the period is from 10~70 sec, where the heave and pitch natural frequency are included. To maintain steady state motions, the conservative simulation duration is determined as 10000 sec. During the ramping time of 1500 sec, the regular wave force graudally increases to prevent the large trasient response of a platform.

Table 25. Regular wave test condition

Item	Unit	Value
Wave Height, H	(m)	1 ~ 3
Wave Period, T	(sec)	10 ~ 70
Simulation duration	(sec)	20000
Ramping time	(sec)	1500

5.6.4.1 Wave height = 1, 3 m, Wave period = 32 sec

Two different wave heights of 1 m and 3 m with a 32 sec period, which is the heave natural period, are applied for the regular wave tests. The surge and pitch motions in the three cases have similar statistics with the similar extreme values, whereas the statistics in heave motions of the three cases are quite different. The heave motion in NA1 is the largest followed by those in NA3 and NA2, as shown in Figure 81. First, the heave motion in NA1 is amplified and shows the resonance motion. However, in NA2 and NA3, a smaller heave motion than that in NA1 is observed due to the nonlinear effects related to stiffness with the increasing heave motion. Furthermore, the nonlinear FK force makes the heave motion in NA2 even smaller. The incident wave force applied on NA1 and NA3 is a sinusoidal function and the PSD plot has one peak at the frequency equal to the wave frequency. However, due to the sloped hull shape, the nonlinear FK force becomes non-sinusoidal with double frequency, as shown in Figure 84. In the corresponding PSD plot for NA2, two peak frequencies are observed. Consequently, the wave force amplitude at the original wave frequency is reduced, and thus the corresponding heave amplitude is also reduced, as observed in Figure 82.

Table 26. Statistics of an Arctic Spar platform under the regular wave (H = 3 m, T = 32 sec)

	NA1				NA2				NA3			
	Max.	Min.	Mean	Std.	Max.	Min.	Mean	Std.	Max.	Min.	Mean	Std.
Surge (m)	1.77	-1.77	-0.01	1.25	1.82	-1.68	0.07	1.24	1.79	-1.75	0.02	1.25
Heave (m)	4.78	-4.79	-0.01	3.39	1.75	-1.08	0.37	1.00	3.45	-2.38	0.74	2.07
Pitch (deg.)	0.29	-0.30	0.00	0.21	0.41	-0.36	0.03	0.27	0.31	-0.28	0.02	0.21

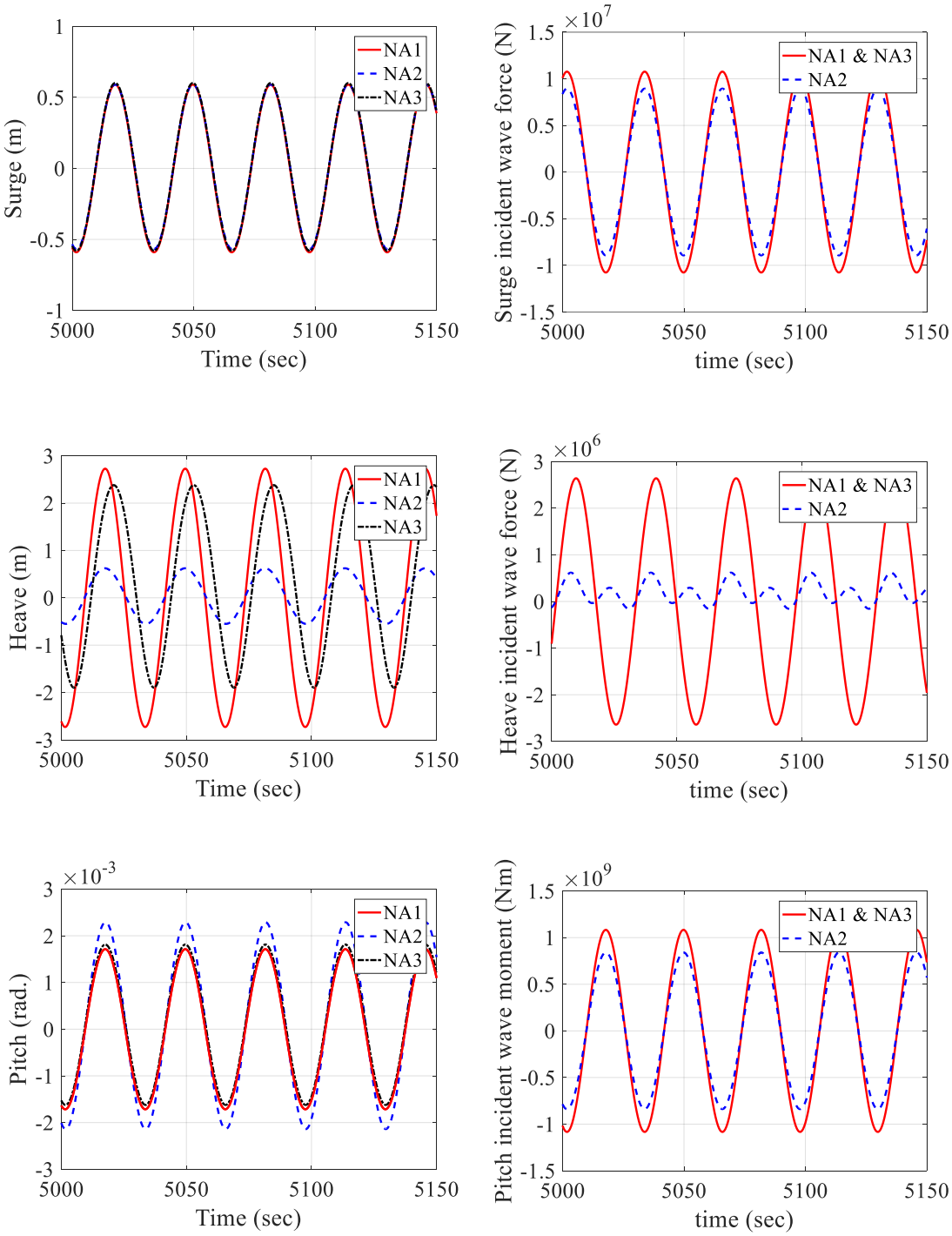

Figure 81. Time series of surge/heave/pitch motion and total wave forces (H = 1 m, T = 32 sec)

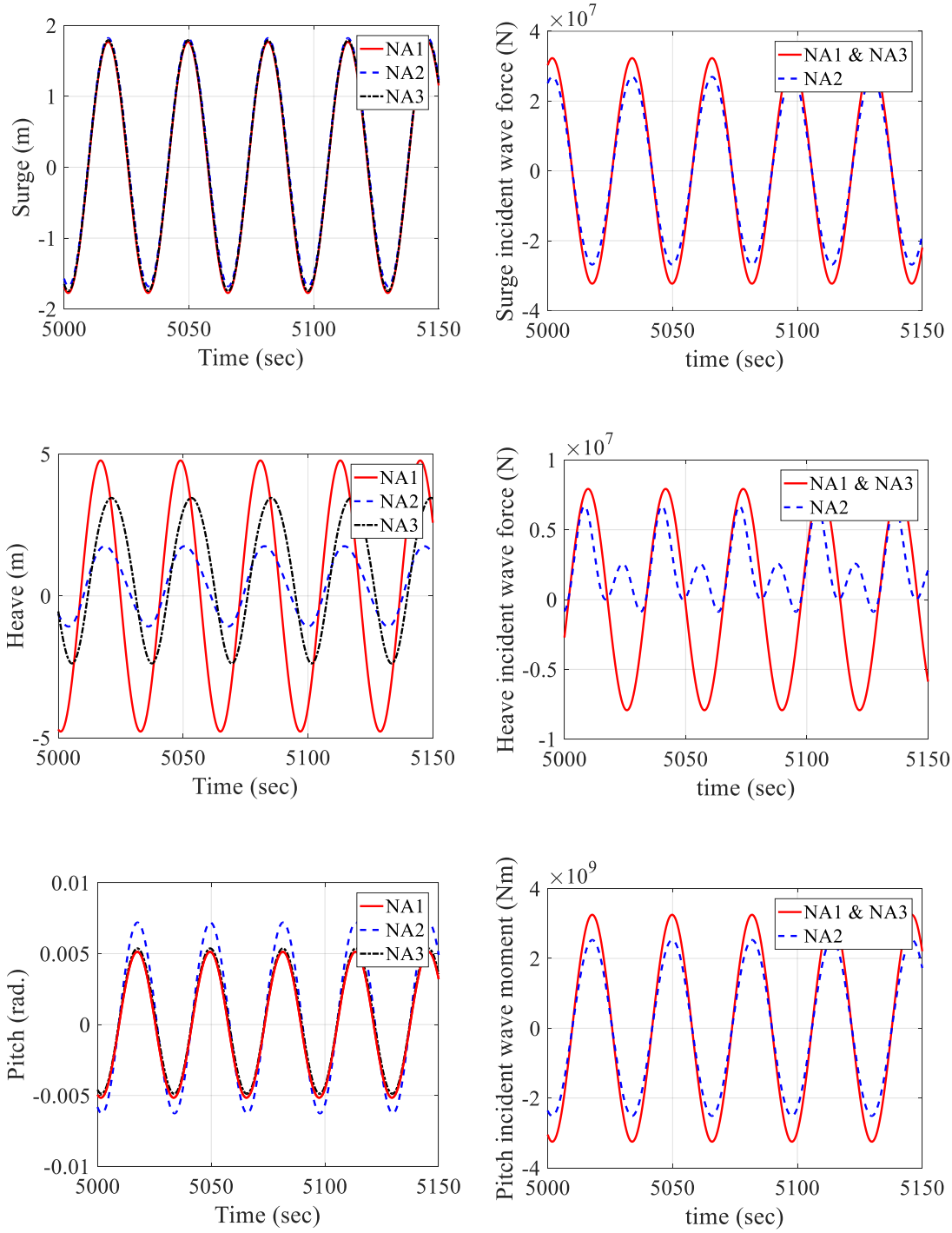

Figure 82. Time series of surge/heave/pitch motion and incident wave forces (H = 3 m, T = 32 sec)

The reason that the total force of NA2 has irregular time-series can be explained by the effect of the nonlinear FK force interacting with the heave motion. The nonlinear FK force in the heave is mostly induced by the pressure on the inverted conical shape near the waterline, since the dynamic pressure decays exponentially with increasing depth. In addition, the upper part of the cone-shaped hull influences the variation of the FK force more than the lower part because the upper part has more area interacting with the fluid.

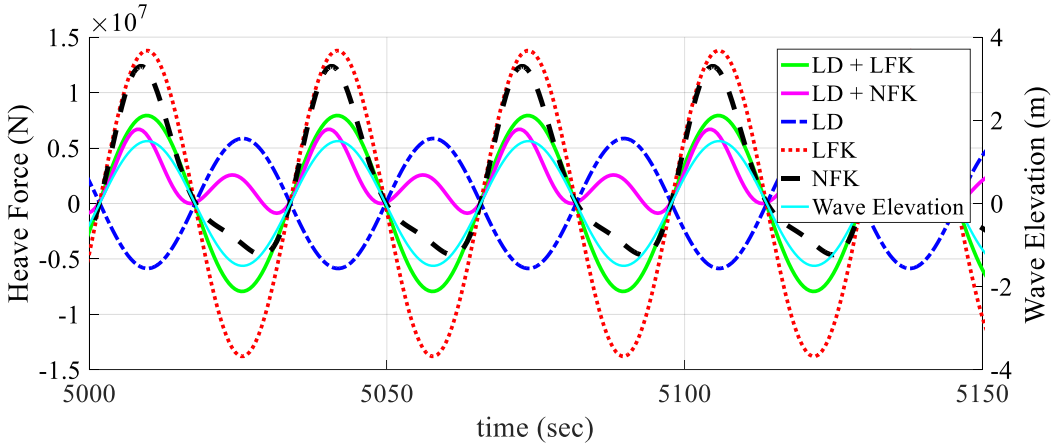

Figure 83. Time series of total wave heave forces (H = 3 m, T = 32 sec)

The black dotted line in Figure 83 represents the nonlinear FK force applied in NA2. At the wave crest, the relative distance from the platform to the wave crest is positive and the upper part of the cone is submerged, which results in a large impact on the FK force in the heave. At the wave trough, the submergence of the cone-shaped surfaces decreases and is relatively less affected by the FK force than the case at the wave crest. Therefore, the nonlinear FK force has a large amplitude at the wave crest and vice versa at the wave trough. Therefore, the summation of the linear diffraction force and nonlinear FK force

gives an irregular wave force signal, as shown in Figure 83. This irregular wave force has two excitation frequencies: the wave frequency and twice the wave frequency. These double frequencies in NA2 result in the suppression of the resonance response in the heave.

On the other hand, the peaks of the three cases in the pitch PSD plot are located at the frequency equal to the wave excitation frequency. This result implies that none of the three cases exhibits heave-to-pitch Mathieu instability with a wave height of 3 m and a period of 32 sec, because they do not satisfy the instability conditions. This example typically shows that even though heave motion is large, if its half frequency does not coincide with the pitch natural frequency, pitch MI does not occur. On the contrary, the next section shows that even if the heave motion is not large, if its half frequency coincides with the pitch natural frequency, pitch MI happens and it results in large pitch/roll motions at the half frequency of heave and wave. In this regard, the MI resembles the phenomenon of sub-harmonic parametric excitation.

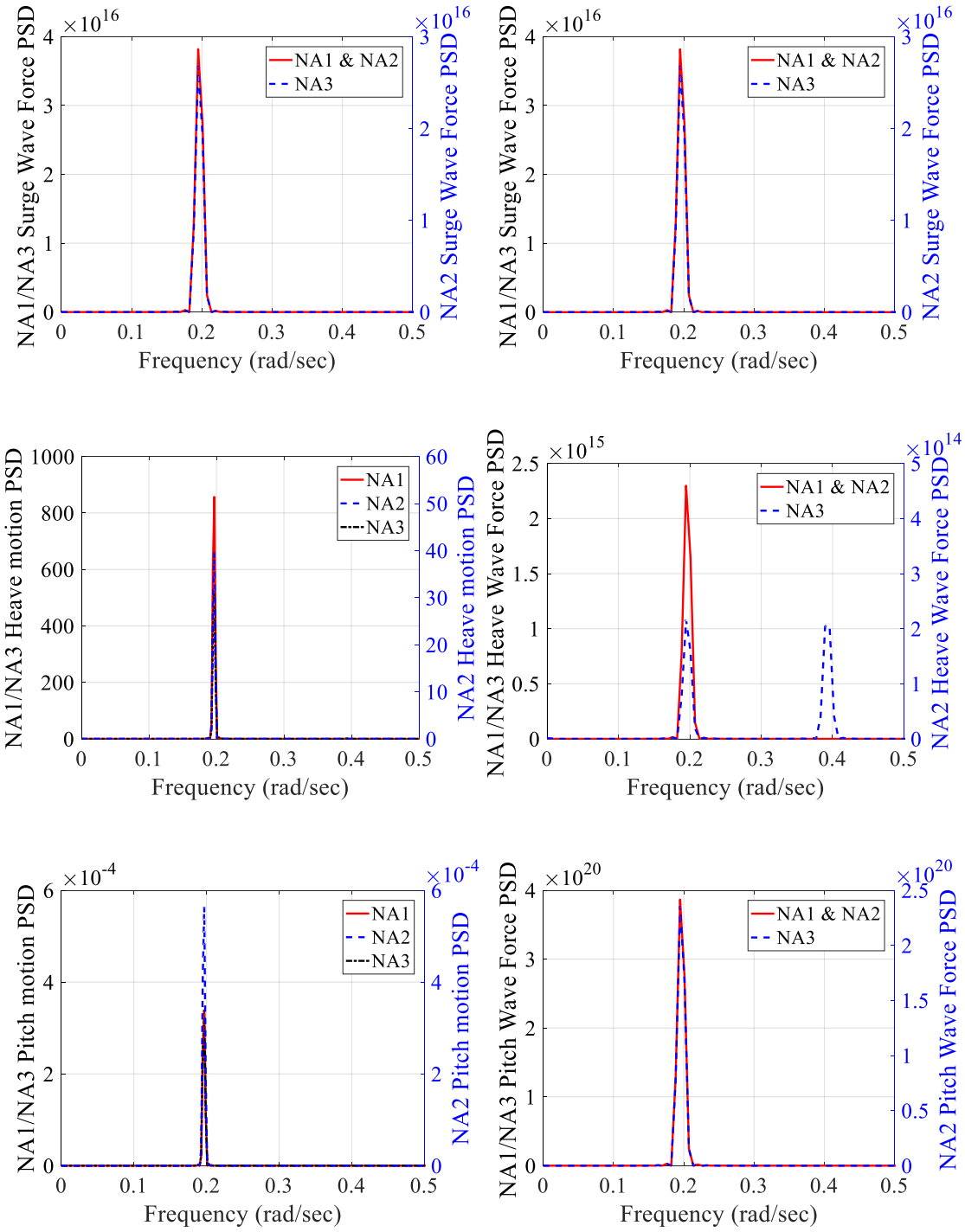

Figure 84. PSD of motions and total wave forces in of heave/pitch directions (H = 3 m, T = 32 sec)

5.6.4.2 Wave height = 3 m, Wave period = 29 sec (Pitch/Roll Mathieu Instability)

In the next simulation, a slight change in the wave period to 29 sec is made so that the ratio of the pitch natural frequency to the wave frequency, α-factor, can be close to 0.25. Compared to the previous case, the wave frequency is more distanced away from the heave natural frequency and the resulting amplitudes of heave motions are generally smaller in all cases. However, in NA2 and NA3, due to the nonlinearity, large pitch motions at the half frequency clearly appear at the later stage of simulation due to Mathieu-type instability. Figure 85 shows the corresponding time-simulation results. Up to 2700s, ordinary wave-frequency pitch motions can be observed. However, from the 2700 sec, the pitch motion in NA3 is suddenly amplified, and the greatly increased pitch motions at the half of wave frequency continue as a result of Mathieu instability. The initially growing motion by MI is limited later by nonlinearity to have stable motion amplitude and period. Similar phenomenon also happens in NA2 at the delayed time of after 3800 sec. In both cases, the peaks in the pitch PSD are not located at the wave frequency but at its half frequency, as evidenced in Figure 86 and Figure 89, close to the pitch natural frequency, which implies resonant motion. Interestingly, up to 2700s, all the 3 cases produced very similar pitch motions. Since roll equation of motion is very similar to that of pitch (Eq. (44)), the same Mathieu instability also happens, as evidenced by Figure 85b in the roll mode. On the other hand, in Figure 86, we do not observe any Mathieu instability in heave motions.

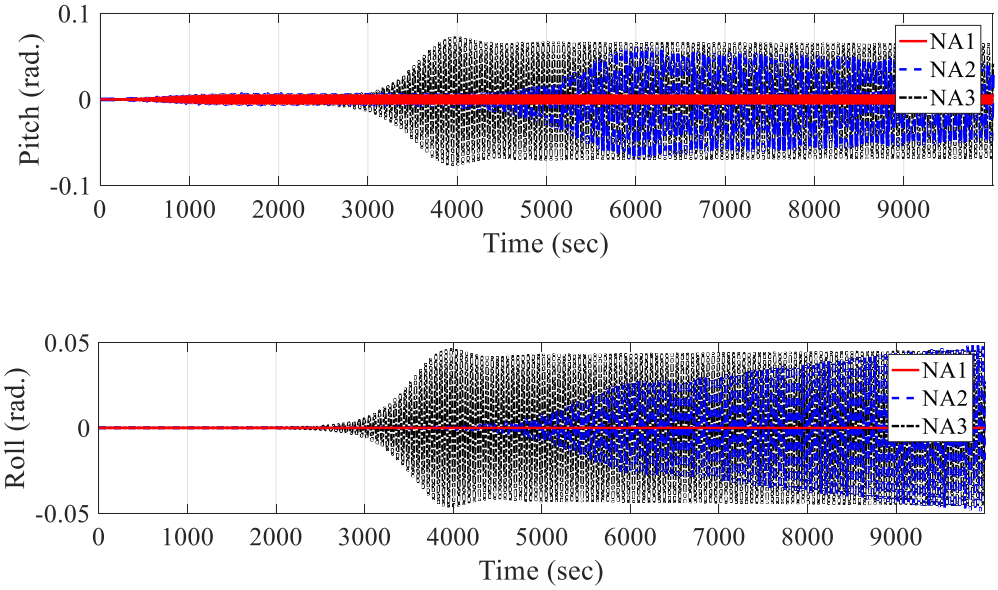

Figure 85. Time series of pitch (a) and roll (b) motions for 10000 sec (H = 3 m, T = 29 sec)

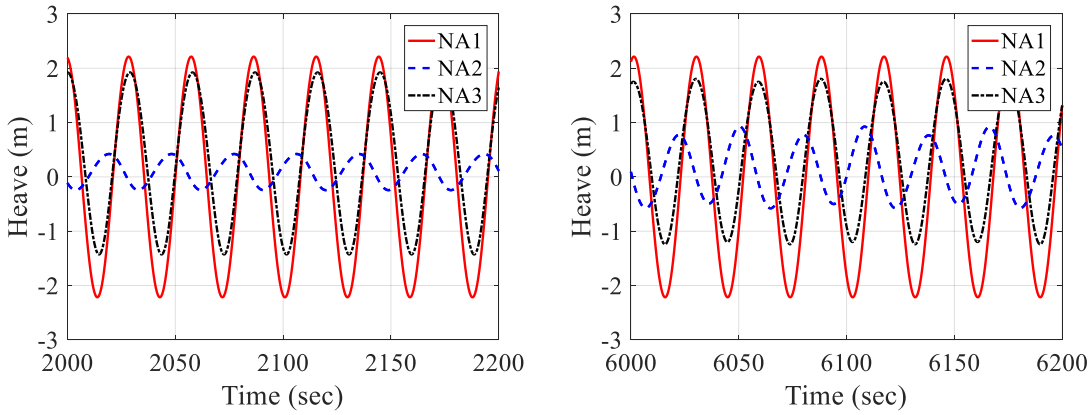

Figure 86. Time series of heave motions (H = 3m, T = 29 sec)

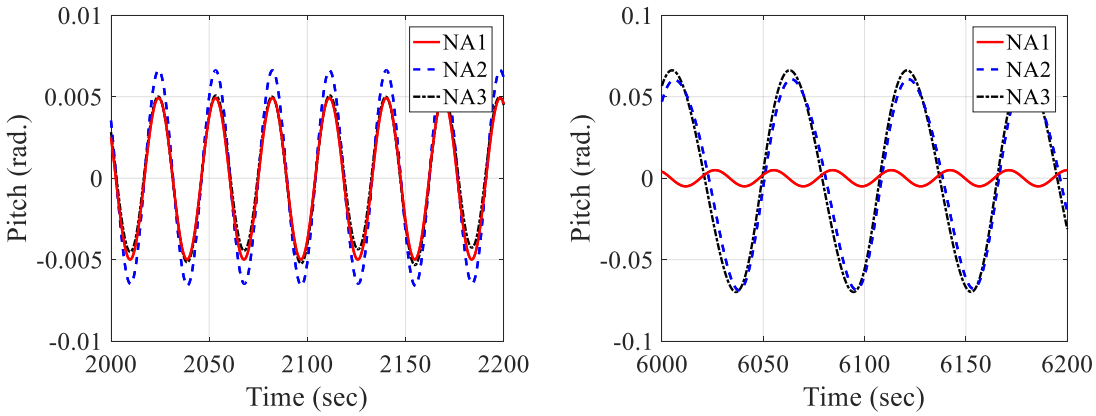

Figure 87. Time series of pitch motions (H = 3m, T = 29 sec)

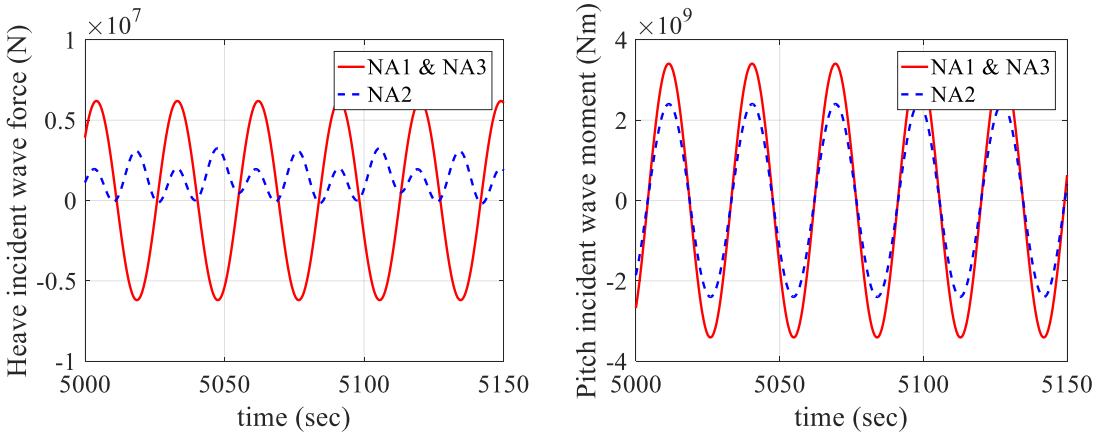

Figure 88. Time series of heave and pitch wave forces (H = 3m, T = 29 sec)

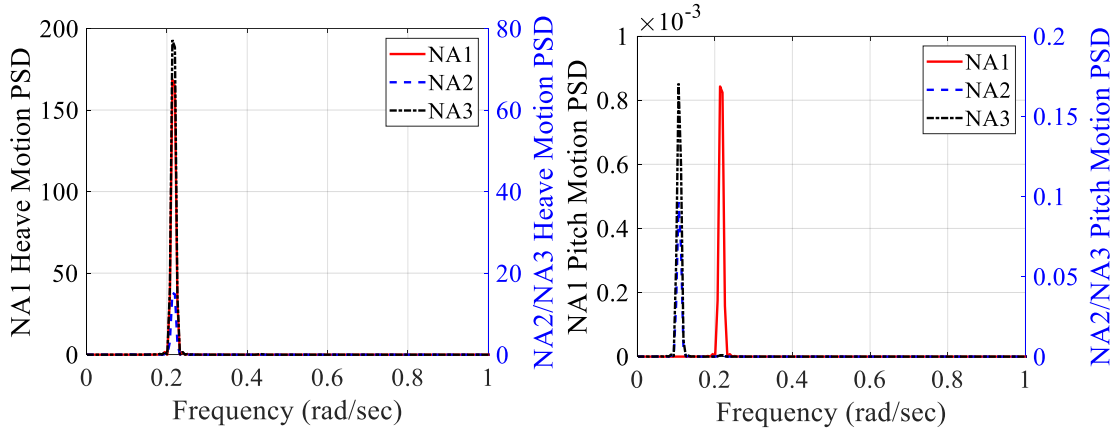

Figure 89. PSD of heave and pitch motions (H = 3m, T = 29 sec)

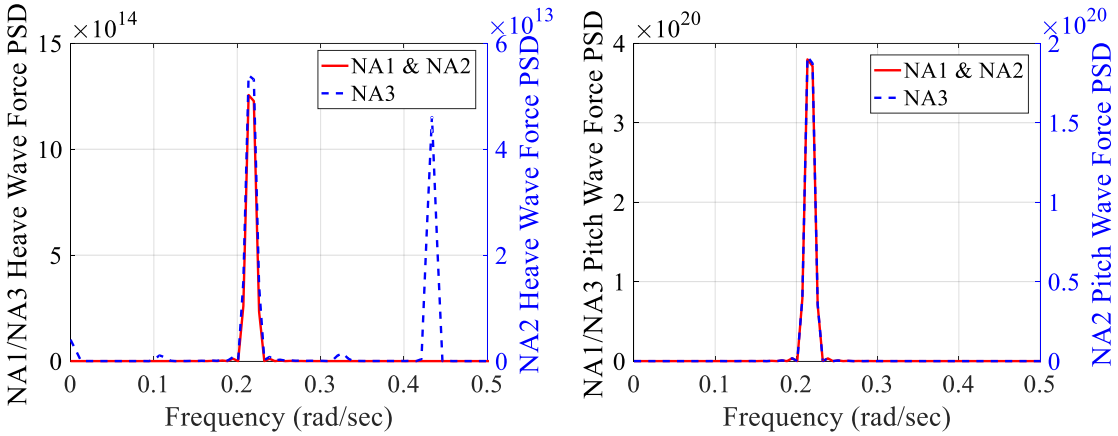

Figure 90. PSD of heave and pitch wave forces (H = 3m, T = 29 sec)

Table 27. Statistics of an Arctic Spar platform under the regular wave (H = 3 m, T = 29 sec)

	NA1				NA2				NA3			
	Max.	Min.	Mean	Std.	Max.	Min.	Mean	Std.	Max.	Min.	Mean	Std.
Surge (m)	1.58	-1.61	-0.01	1.13	6.87	-8.41	0.04	4.29	7.70	-8.65	0.02	5.44
Sway (m)	0.00	0.00	0.00	0.00	5.47	-5.48	0.00	2.77	5.12	-5.11	0.00	3.53
Heave (m)	2.22	-2.22	0.00	1.57	0.93	-0.58	0.14	0.45	1.81	-1.24	0.34	1.06
Roll (deg.)	0.00	0.00	0.00	0.00	2.80	-2.79	0.00	1.42	2.61	-2.62	0.00	1.80
Pitch (deg.)	0.28	-0.29	0.00	0.20	3.48	-3.94	0.01	2.13	3.83	-4.04	0.01	2.73
Yaw (deg.)	0.00	0.00	0.00	0.00	0.02	-0.02	0.00	0.01	0.00	0.00	0.00	0.00

As the wave height increases, the Mathieu instability in NA2 and NA3 occurs earlier. With the wave height of 5 m, the instability is initiated at 2000 sec in NA3, which is 700 sec earlier than the case of H = 3 m. Similarly, although the heave motion in NA2 is still small, resonance-type behavior in the pitch motion is observed. Since the heave motion increases with the wave height, more heave energy is transferred to the pitch motion. In addition, the parameter, β, in Table 20 increases linearly with the heave motion, which means the structure is more likely to be located in the unstable region in Figure 73.

In this comparison, the linear analysis cannot capture nonlinear phenomena such as Mathieu instability because it assumes that the metacentric height (GM) and the restoring stiffness are constant throughout the simulation. However, the nonlinear analysis with the time-varying restoring stiffness clearly shows the nonlinear behavior of Arctic Spar. In the previous studies examining the nonlinear phenomena of structures, some researchers (Haslum, 2000; Dalane et al., 2012) have presented a simplified method to approximate the time-varying GM, and others (Haslum et al., 1999; Koo et al., 2004; Jingrui et al., 2009) have derived an analytic pitch equation of motion coupled with the heave motion and wave elevation. In the current study, we grid the instantaneous submerged body and calculate the exact HC. By taking advantage of computing the time-varying nonlinear HC in a numerical simulation, we find the time series and PSD of the pitch restoring coefficients, as presented in Figure 91. The restoring coefficients in NA2 and NA3 show irregular signals with multiple frequencies. The dominant frequency at 0.21 rad/sec in the PSD plots is the same as the wave frequency, and this corresponds to the α-factor of 0.25, which is the first principal unstable region of Mathieu instability.

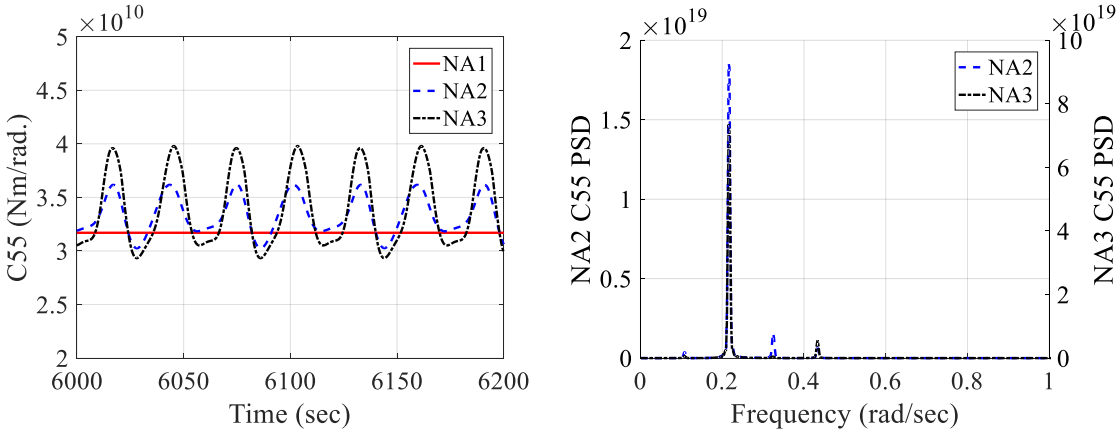

Figure 91. Times series and PSD of the pitch restoring coefficient, C55 (H = 5m, T = 29 sec)

The initial heave motion influences not only the pitch motion but also the roll motion by transferring the energy internally, as is pointed out in Figure 85. Therefore, when Mathieu instability occurs, the spar tends to have conical-pendulum-like behavior including both pitch and roll. Figure 92 indicates the trajectory of the horizontal motion (a) and the phase plane trajectory of the roll motion (b). Over time, the roll motion increases, and the sway motion develops correspondingly. This is because the equation of the roll motion is also coupled with the heave motion in the form of the Mathieu equation as the pitch equation of motion. However, the roll motion generally requires a longer time than the pitch case to fully develop and reveal the Mathieu instability.

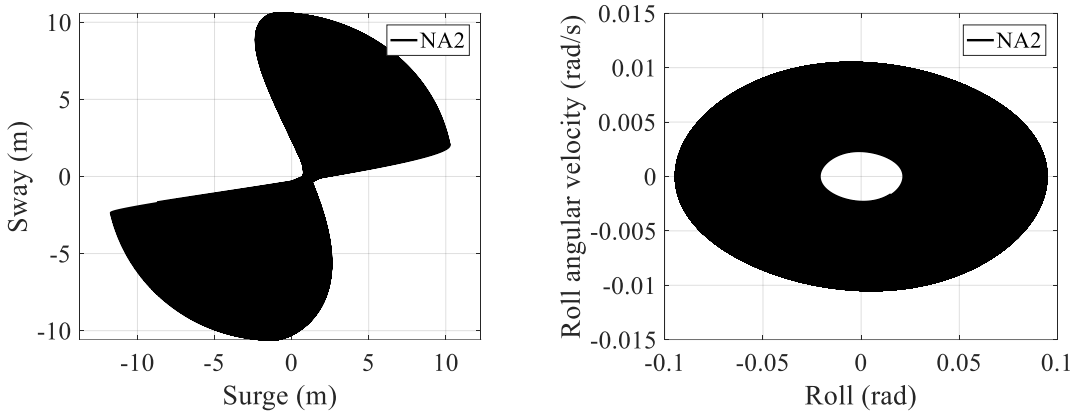

Figure 92. (a) Horizontal motion trajectory and (b) phase plane trajectory
(H = 5m, T = 29 sec, time: 0~10000 sec)

The Mathieu stability diagram is also investigated theoretically and numerically. The theoretical diagram is drawn using Hill's infinite determinants method in Figure 93 for NA3. The markers are the results from the time-domain simulations corresponding to the wave heights of 1 m, 3 m, and 5 m and periods of 25 sec, 27 sec, 29 sec, 31 sec, and 33 sec. The theoretical line is computed based on the simplified equation of the pitch motion without a damping term, Eq (44). The damping slightly elevates the bottom cusp. Since the pitch damping is relatively small in the present case, the given line is the reasonable measure of MI occurrence. When comparing the theory and actual nonlinear numerical simulations, it is seen that the equation predicts the unstable regions well.

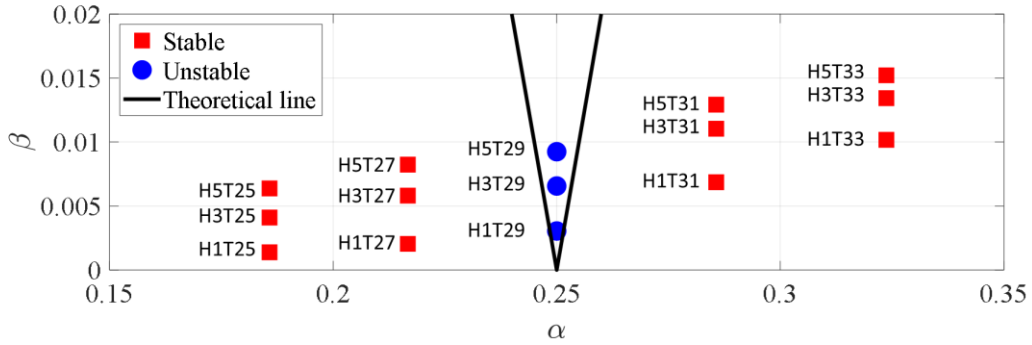

Figure 93. Pitch stability diagram for NA3

5.6.4.3 Wave height = 3 m, Wave period = 14 sec

In the regular wave test with a 3 m wave height and 14 sec period, which is close to half of the heave natural frequency, the heave and pitch motions in the three cases are very small and oscillated with the wave excitation frequency of 0.455 rad/sec. The small motions are obvious because the wave period of 14 sec is out of the range of the natural frequencies. The results in NA1 and NA3 are almost identical in all directions. The difference of NA2 in the heave is attributed to the nonlinear wave forces applied on the sloping wall. When the structure moves downward, the submerged part of sloping surfaces increases and hence a larger nonlinear FK force is applied on the structure more than when it moves upward. Therefore, the mean heave position in NA2 is a positive value. Although the nonlinear effect is observed under this condition, there is no Mathieu instability.

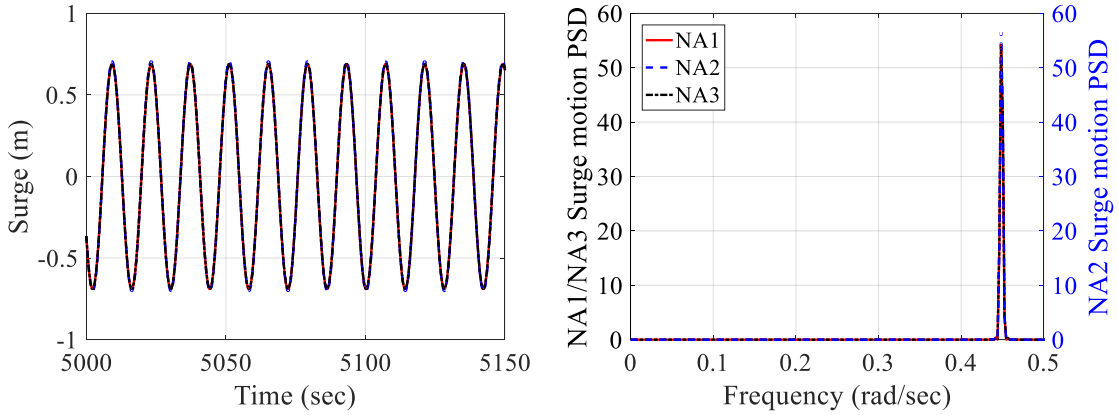

Figure 94. Time series and PSD of surge motions (H = 3 m, T = 14 sec)

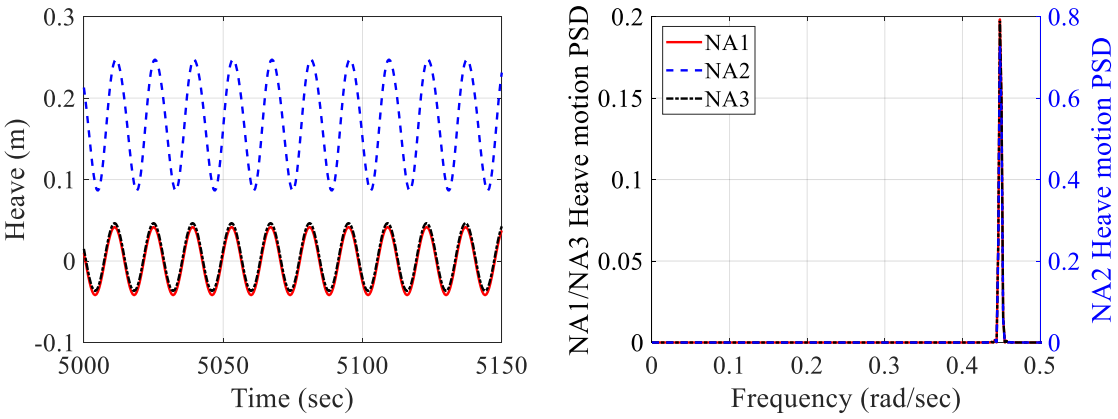

Figure 95. Time series and PSD of heave motions (H = 3 m, T = 14 sec)

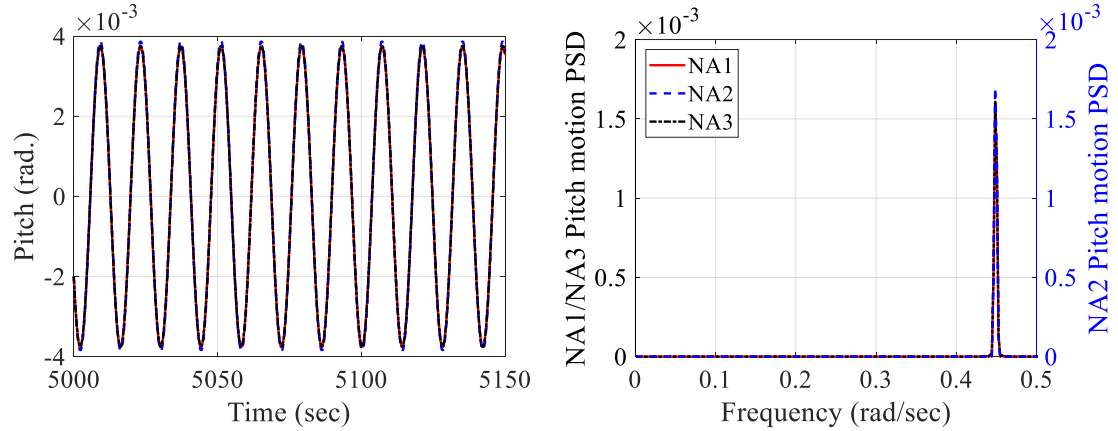

Figure 96. Time series and PSD of pitch motions (H = 3 m, T = 14 sec)

Table 28. Statistics of an Arctic Spar platform under the regular wave (H = 3 m, T = 14 sec)

	NA1				NA2				NA3			
	Max.	Min.	Mean	Std.	Max.	Min.	Mean	Std.	Max.	Min.	Mean	Std.
Surge (m)	0.69	-0.69	0.00	0.49	0.71	-0.70	0.00	0.50	0.69	-0.69	0.00	0.49
Heave (m)	0.04	-0.04	0.00	0.03	0.25	0.09	0.17	0.06	0.05	-0.04	0.01	0.03
Pitch (deg.)	0.21	-0.22	0.00	0.15	0.22	-0.22	0.00	0.16	0.22	-0.21	0.00	0.15

Since the motion has a 180-degree phase difference from the wave elevation, the maximum relative distance from the body to the wave elevation occurs at the wave crest. As discussed above, the upper part of the cone shape has a larger impact on the nonlinear FK force than the lower part, which results in a larger amplitude of the force at the wave crest than at the wave trough. In addition, the hydrostatic restoring stiffness becomes hardened when the relative distance between the body and wave elevation increases, and the body moves downward. Consequently, when the body moves upward, it experiences a large upward vertical force as well as stiffness softening, and the mean heave position in NA2 is not equal to zero, but it is a positive value. As the wave height increases, the nonlinear effects become larger, showing an asymmetric force amplitude and an increased positive offset in the heave direction.

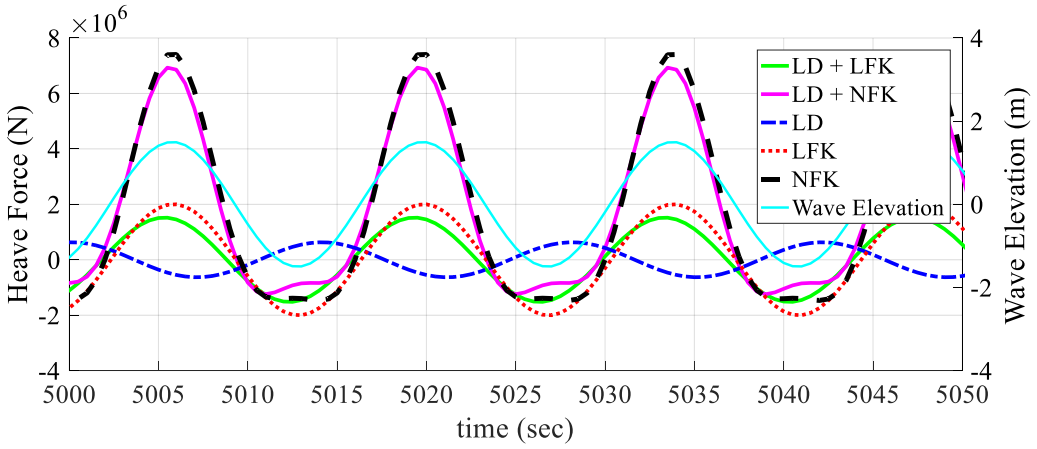

Figure 97. Time series of total wave heave forces (H = 3 m, T = 14 sec)

5.6.4.4. Wave height = 3 m, Wave period = 16 sec

At the wave period of 16 sec i.e. half of the heave natural period, Mathieu instability in the heave motion is observed in NA2 and NA3. Since the restoring stiffness of NA1 is constant throughout the simulation, the heave motion in NA1 shows a harmonic motion, and the frequencies of the heave and pitch motions are the same as the incident wave frequency. In contrast, the heave motions in NA2 and NA3 show greatly amplified motions at the half of wave frequency (=heave natural frequency), starting at 1100 sec and 2300 sec, respectively (Figure 98). The PSD plot in Figure 99 also indicates that this behavior occurs at the heave natural frequency. It is also seen that the nonlinear FK enhances the magnitude of MI through enlarged heave motions. In another simulation example of wave height 1 m, although not shown here, Mathieu instability also occurs in the heave direction in both NA2 and NA3 cases. Figure 100 shows that we do not have such MI phenomenon for pitch mode. As far as authors know, the time-domain nonlinear simulation results showing this kind of heave-to-heave MI caused by the inclined surface

near the waterline were not published in the open literature. The 16 sec wave period is very close to the peak period of the typical 100-yr storm, so this phenomenon may be of significant practical importance, which will be investigated in the next section.

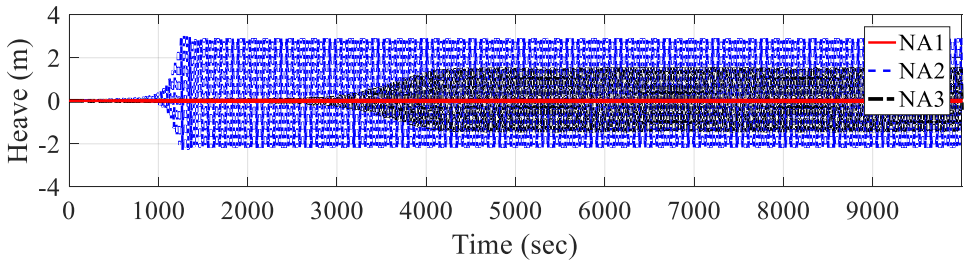

Figure 98. Time series of heave motions for 10000 sec (H = 3 m, T = 16 sec)

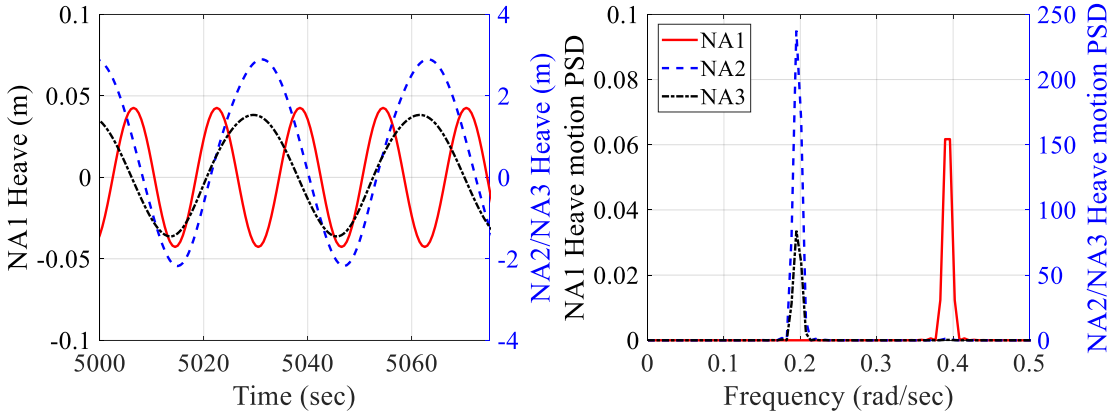

Figure 99. Time series and PSD of heave motions (H = 3 m, T = 16 sec)

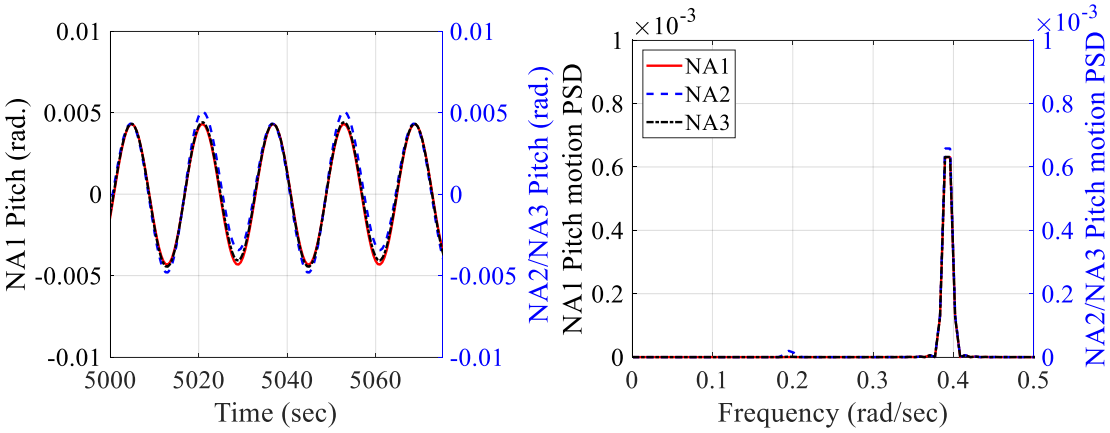

Figure 100. Time series and PSD of pitch motions (H = 3 m, T = 16 sec)

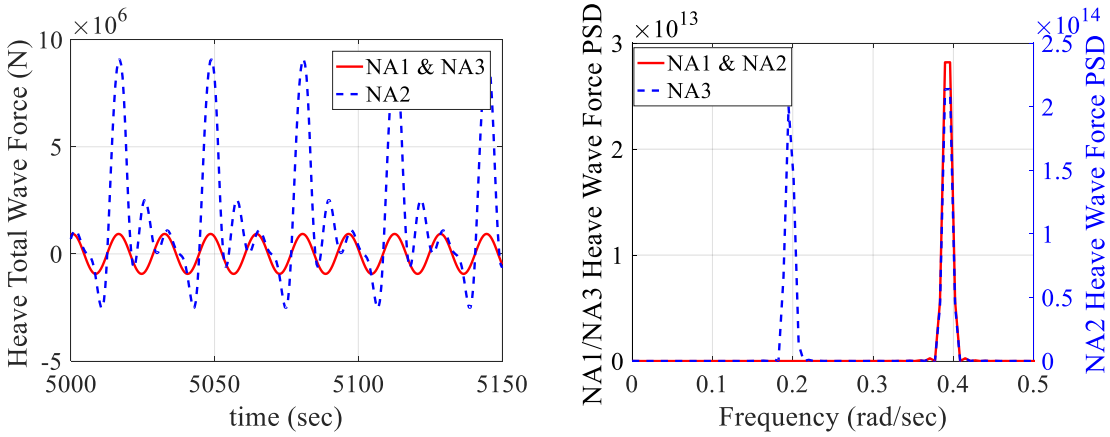

Figure 101. Time series and PSD of heave wave force (H = 3 m, T = 16 sec)

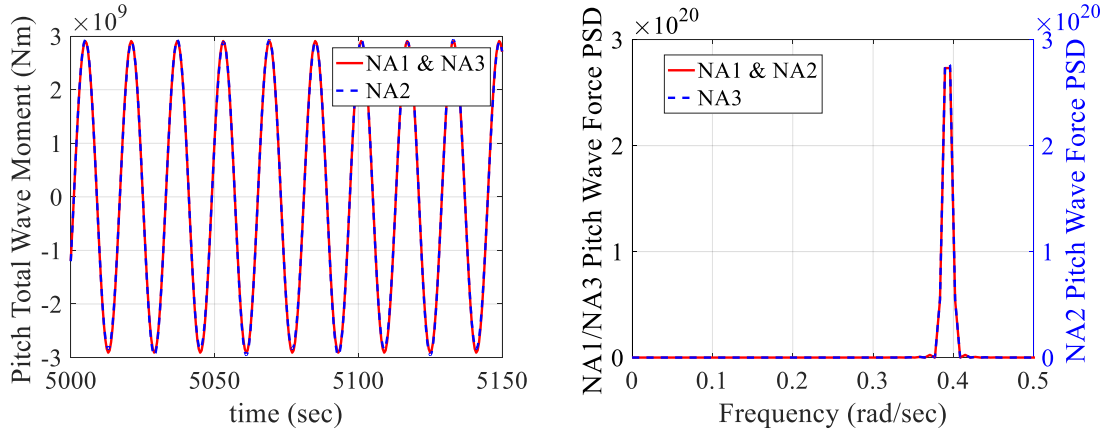

Figure 102. Time series and PSD of pitch wave force (H = 3 m, T = 16 sec)

Table 29. Statistics of an Arctic Spar platform under the regular wave (H = 3 m, T = 16 sec)

	NA1				NA2				NA3			
	Max.	Min.	Mean	Std.	Max.	Min.	Mean	Std.	Max.	Min.	Mean	Std.
Surge (m)	0.85	-0.86	0.00	0.61	0.96	-0.91	0.05	0.62	0.87	-0.87	0.01	0.61
Heave (m)	0.04	-0.04	0.00	0.03	2.90	-2.18	0.54	1.77	1.53	-1.45	0.14	1.05
Pitch (deg.)	0.25	-0.25	0.00	0.18	0.29	-0.28	0.02	0.18	0.25	-0.26	0.00	0.18

A similar trend is observed in the cases with a higher wave height. At a wave height of 5 m, although not shown here, before a steady-state response fully develops, Mathieu instability is initiated earlier than the H=3m case i.e. from 800 sec in NA2 and 1100 sec in NA3, respectively. We find that Mathieu instability in heave is more sensitive to the wave height than the instability in the pitch direction. This is because β-factor is directly associated with the wave amplitude, $\bar{\eta}$, and the order of β-factor in heave is much larger than that in pitch. The time-varying heave restoring coefficients in NA2 and NA3 are presented in Figure 103. At the early stage of simulation with a small heave motion, the wave elevation component mainly contributes to the change in the restoring coefficient with the same frequency as the encounter wave. However, after Mathieu instability occurs due to the resonance, the quadratic term in Eq. (42) influences the heave restoring coefficients far more than the wave. Therefore, the behavior of the time-varying heave restoring coefficient is also changed to that of dual frequency, as can be seen in Figure 103b and c.

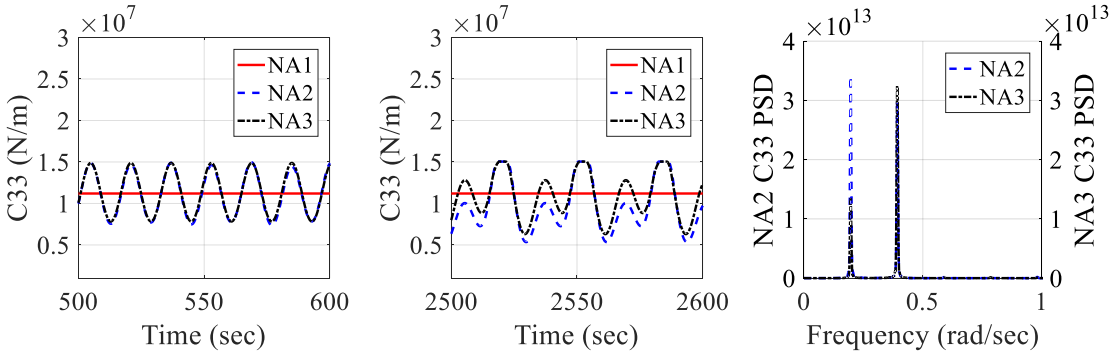

Figure 103. Times series ((a) and (b)) and PSD (c) of heave restoring coefficient, C33 (H = 5m, T = 16 sec)

The heave stability diagram for NA3 is presented in Figure 104. Similar to the pitch case, each marker represents each nonlinear time-domain simulation result. The theoretical diagram predicts the instability and parametric resonances well, which occur at the wave period of 16 sec (H1T16, H3T16, and H5T16). This means that the numerical algorithm for the nonlinear HC can clearly demonstrate essential nonlinear phenomena such as Mathieu instability by having the enlarged motions at the half of the wave frequency, whereas a linear analysis cannot capture it.

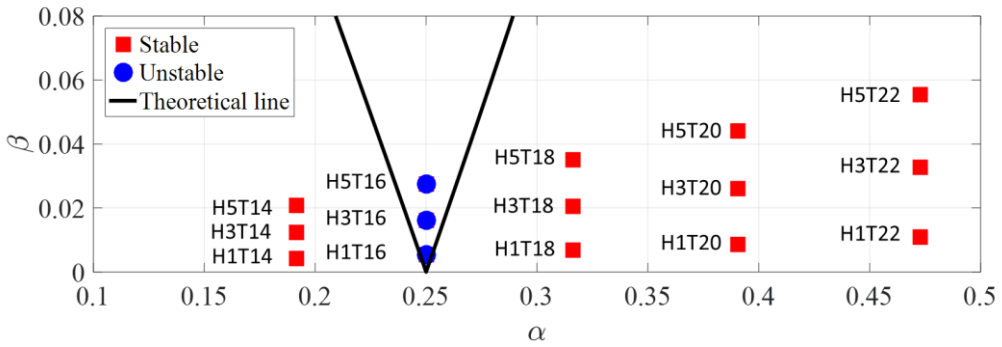

Figure 104. Heave stability diagram for NA3

If enlarged heave motions are generated at the heave natural frequency as a result of heave-to-heave MI instability, the effects of FK force are also to be increased. The amplified motions by larger FK force also enhance the MI instability through the nonlinear HC. This can be called as mutually ascending effect between nonlinear FK force and nonlinear HC for MI. When it happens, the theoretical Mathieu instability line is to be modified due to the nonlinear terms of Eq. (42), as was pointed out by El-Dib (2001). The nonlinear terms in the Mathieu equation generally increase the width of the unstable region.

5.6.4.5. Influence of Wave Height

By varying the wave frequency and height, the heave and pitch amplitude per unit wave height are measured in a time domain simulation and the results are shown in Figure 107 and Figure 109. Due to nonlinear viscous damping, the amplitude in both the heave and pitch decreases with an increase in the wave height. In NA1, the peaks at the motion's natural frequency are observed in both Figure 107 and Figure 109. In the case of NA2, the resonance-type peak is not observed near the heave natural frequency in the heave amplitude plot, while the resonance peak is clearly recognized in the pitch amplitude plot. The frequency of 0.190 rad/sec where the small peak occurs shifts left to 0.179 rad/sec with an increase of wave height. However, the frequency of 0.108 rad/sec where the maximum pitch amplitude occurs shifts right to 0.110 rad/sec with an increase of wave height. These results are consistent with the conclusion from the previous free decay tests. The decaying period in the heave free decay test is larger with greater displacement, and

the decaying period in the pitch free decay test increases with a smaller motion. The trends of the decaying period also correspond to the shift of peak frequencies. Although it is not discussed in this paper, the Mathieu type instability is observed at a frequency that is a half of heave and pitch natural period. The findings also reveal that Mathieu type instability is more likely to arise with an increase in wave height.

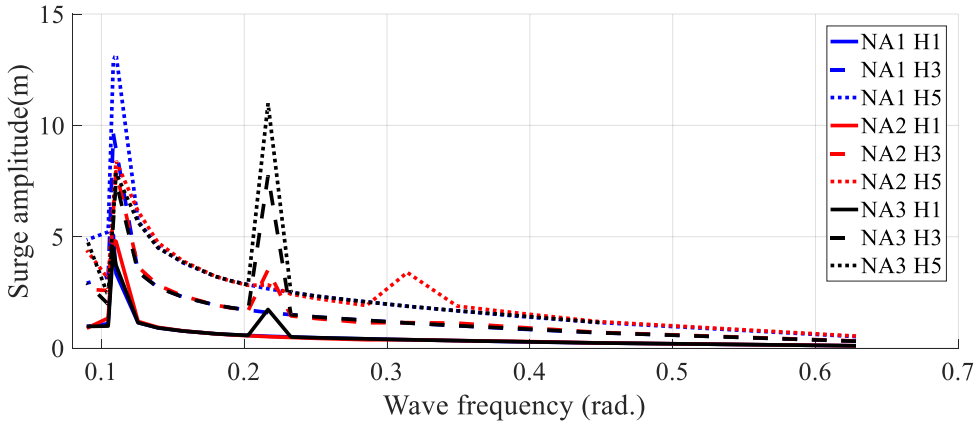

Figure 105. Surge frequency-response curve (H = 1, 3, 5 m)

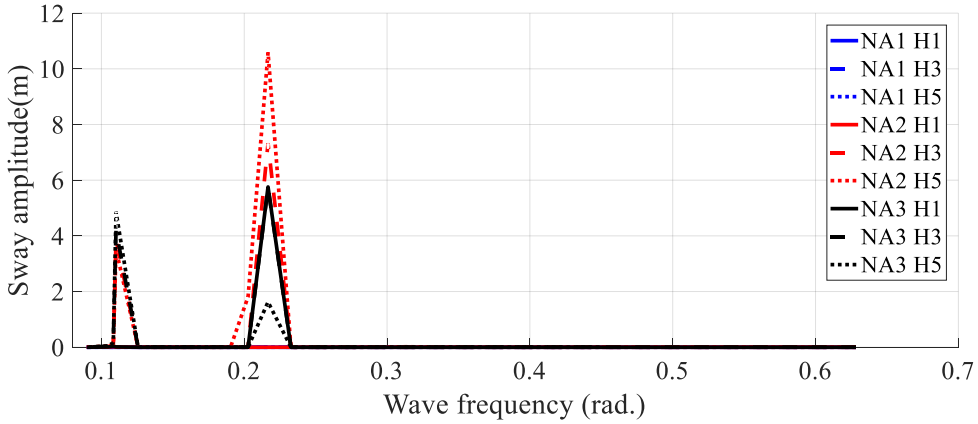

Figure 106. Sway frequency-response curve (H = 1, 3, 5 m)

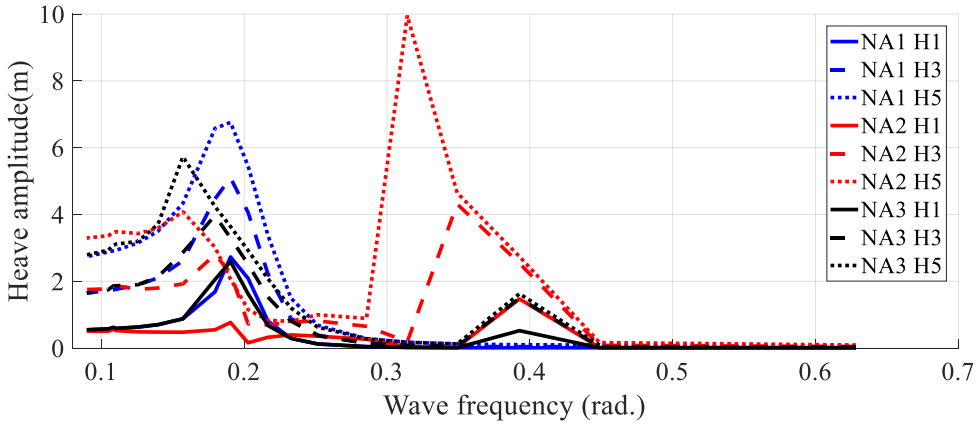

Figure 107. Heave frequency-response curve (H = 1, 3, 5 m)

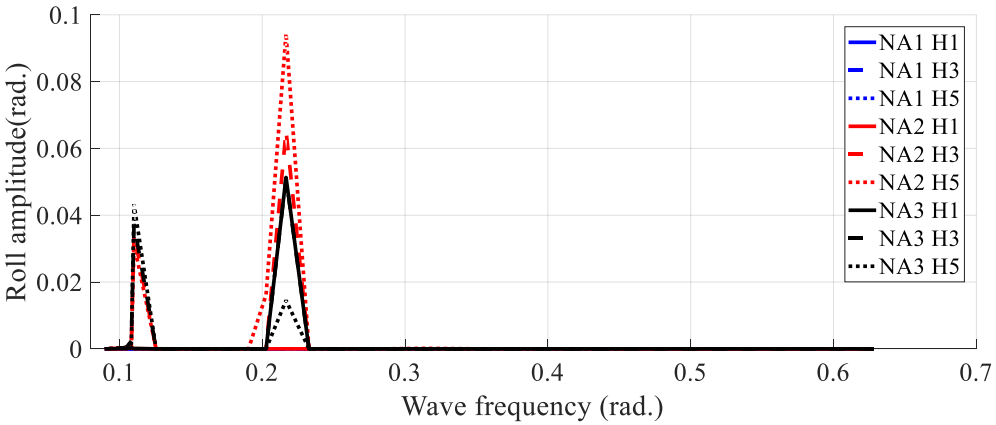

Figure 108. Roll frequency-response curve (H = 1, 3, 5 m)

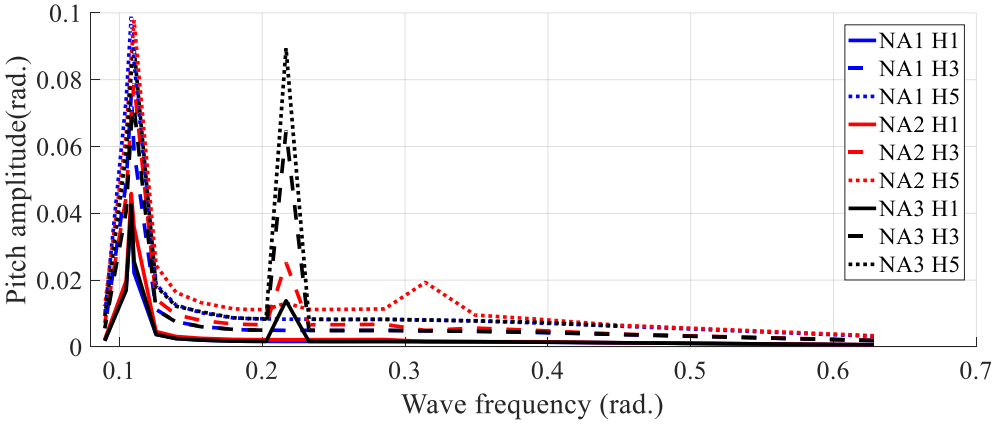

Figure 109. Pitch frequency-response curve (H = 1, 3, 5 m)

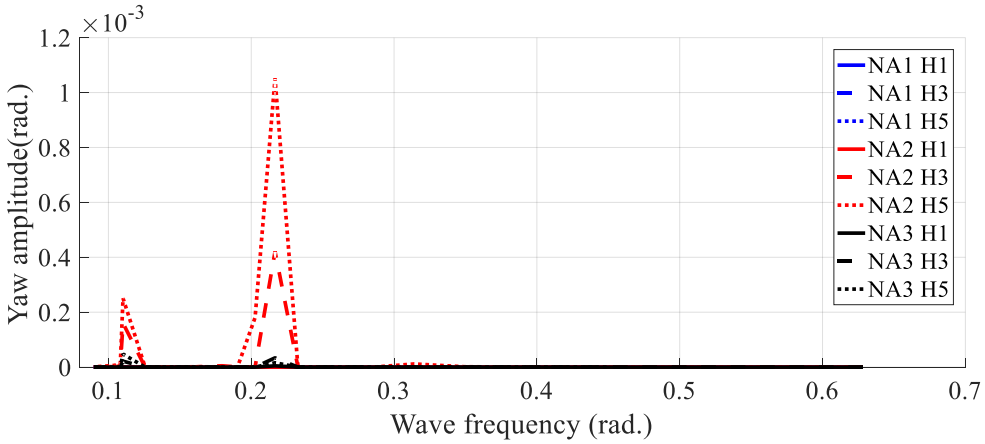

Figure 110. Yaw frequency-response curve (H = 1, 3, 5 m)

5.6.5 Irregular wave test

In this section, the numerical simulation for the same Arctic Spar is conducted under a 100-year storm condition to investigate the nonlinear effects including MI in a more realistic condition. The JONSWAP wave spectrum (Figure 111) is used to generate irregular waves with 100 regular wave components, and frequency intervals are randomly perturbed to generate non-repeating long time history (Kim and Yue, 1991). The current is assumed to be steady with the depth attenuation by 1/7 power law. The environmental conditions are summarized in Table 30, based on Murray et al. (2009). In this section, to observe the 'mutually ascending effect between nonlinear FK and nonlinear HC' more clearly, we introduce another case NA4, in which nonlinear FK force is calculated at the body instantaneous wetted surface but the HC (hydrostatic coefficient) is kept as constant like linear theory. Also, to observe the potential MI phenomenon more clearly, the second-order sum- and difference-frequency wave excitations are intentionally excluded.

Table 30. Random sea environmental conditions

		100-year
Wave	H_s (m)	13
	T_p (sec)	16.5
	Gamma	2.2
Current (m/s)	-	1.8

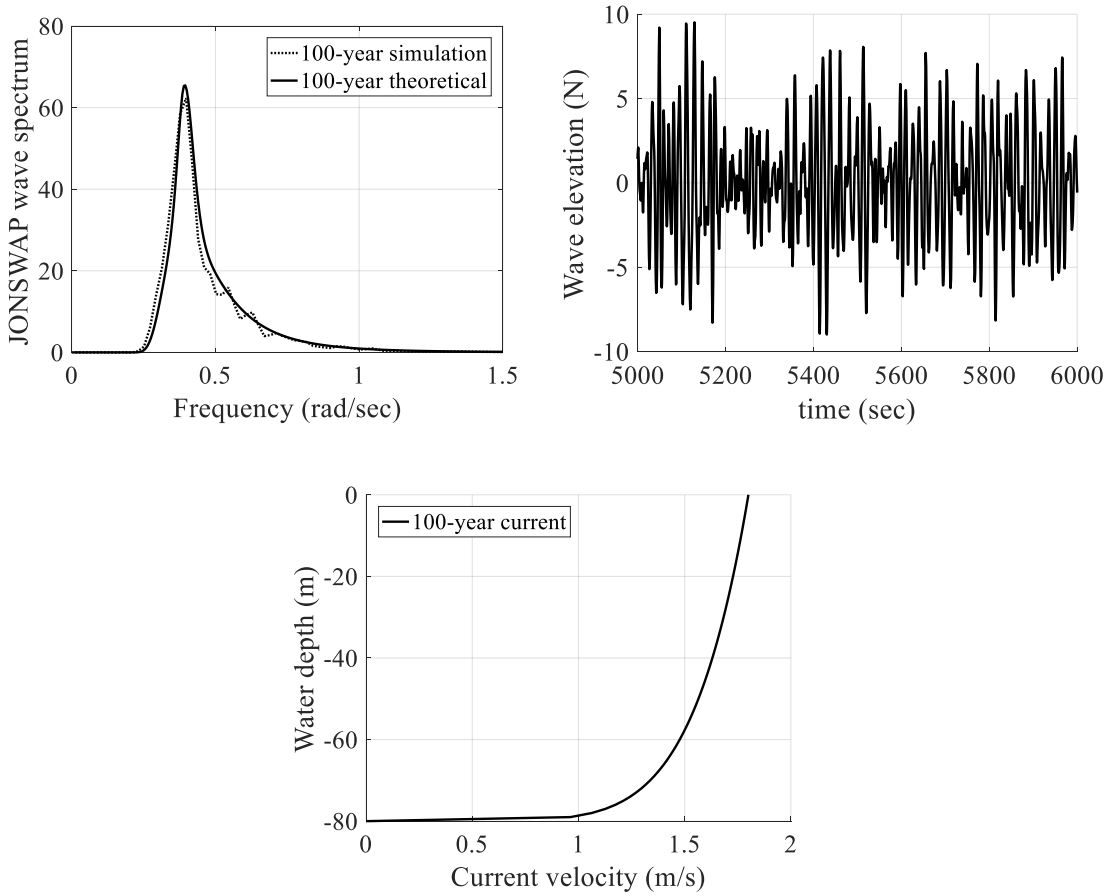

Figure 111. JONSWAP spectrum, time series, and current profile

Figure 112 ~ Figure 117 show the time histories and corresponding PSDs of the platform motions in the 6-DOF directions. The corresponding statistics are tabulated in

Table 31. In surge, the dynamic characteristics of the four cases (NA1, NA2, NA3, and NA4) are similar but two low-frequency peaks are noticeable in NA2 and NA4 due to the nonlinear FK forces. The lowest and second-lowest peaks are at the surge and pitch natural frequencies, respectively. The peak at the pitch natural frequency is caused by the surge-pitch coupled effect.

In the heave direction, since the irregular-wave peak period (T_p) is close to the half of the heave natural period, judging from the insights obtained in the previous regular wave tests, the heave motions in NA2 and NA3 are expected to be largely amplified due to Mathieu instability as subharmonic resonance. However, in NA3, there is no apparent heave-to-heave MI phenomenon and the result is similar to that of NA1, since the wave-frequency heave motions by linear-potential excitations are too small to trigger the MI in NA3 although nonlinear HC is employed. In NA4, we see that the nonlinear FK generates excitations near the heave natural frequency, and thus can amplify the corresponding heave motions. However, since the HC is maintained as constant here, the enlarged motions are not due to MI. In NA2, both nonlinear FK force and nonlinear HC are included, and thus the additional enlargement of heave motions can be attributed to MI. Therefore, we can conclude in this case that both nonlinear FK and nonlinear HC play equally important role in significantly amplifying heave motions through heave-to-heave MI. The standard deviation of heave motion in NA2 is 6.4 times greater than that of linear theory NA1. The above examples demonstrate that the heave-to-heave MI is more clearly observed in swell (regular-wave) condition but it can also play an important role in irregular waves through mutually ascending effect between nonlinear FK force and

nonlinear HC. This conclusion may be related to the fact that Koo et al. (2004) did not observe spar heave-to-pitch MI in irregular waves when only nonlinear HC was employed but later Nallayarasu et al. (2017b) found spar heave-to-pitch MI when both nonlinear FK and nonlinear HC were included. Because the nonlinear FK forces in NA2 and NA4 have positive mean values due to the sloping hull surface near the waterline, as are shown in Figure 118, positive mean values in the heave direction are observed.

In pitch, wave-frequency responses are the same in the four conditions. However, NA2 and NA4 generate low-frequency pitch motions at the pitch natural frequency although there is no wave energy there. There are no nonlinear FK pitch moments there, as can be seen in Figure 119. Large heave motions are generated in NA2 and NA4 only at twice the pitch natural frequency and they trigger the heave-to-pitch/roll MI, as is observed in the regular-wave cases. Their amplitudes are however not that significant to be of practical importance for the present Arctic Spar under this 100-year-storm condition.

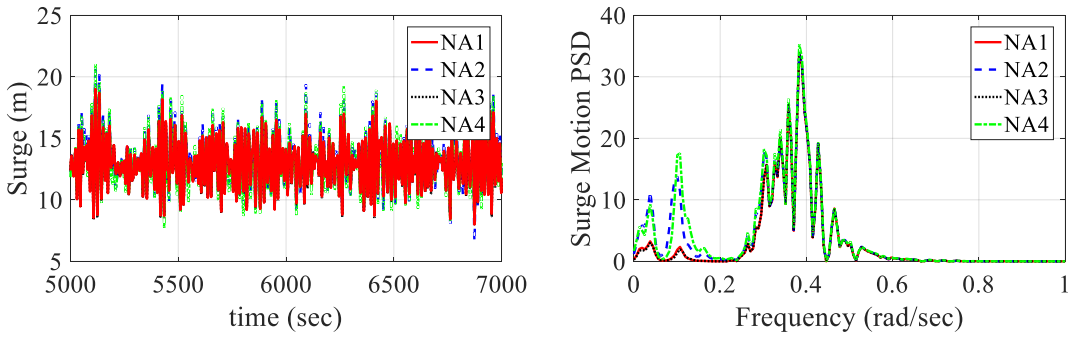

Figure 112. Time-series and PSD of 100-year surge motion

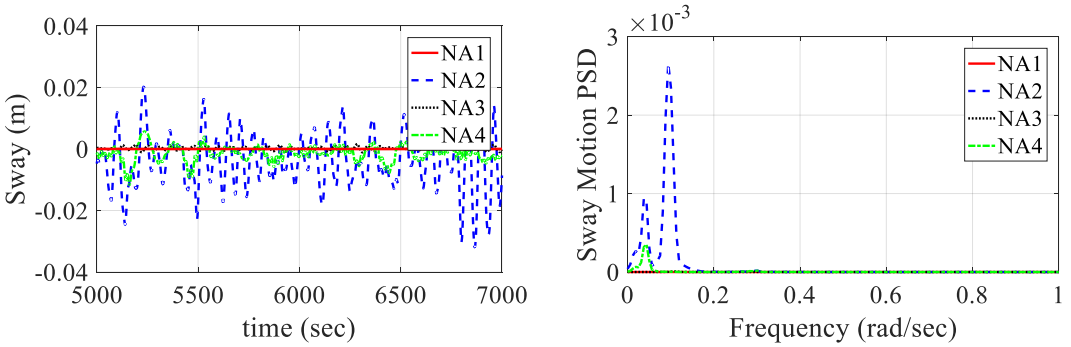

Figure 113. Time-series and PSD of 100-year sway motion

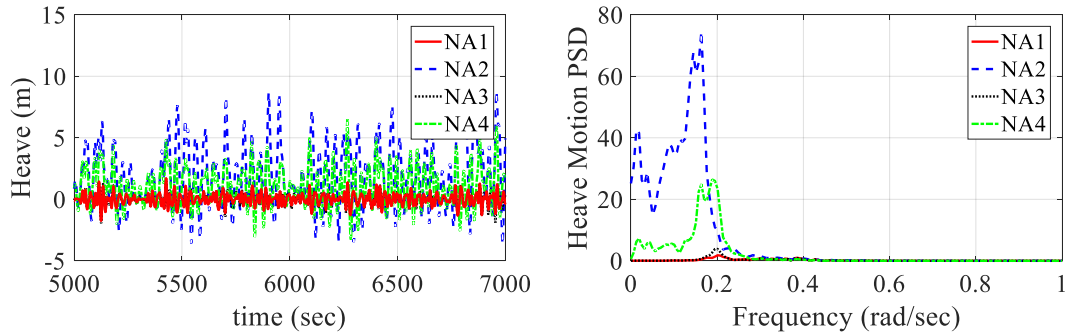

Figure 114. Time-series and PSD of 100-year heave motion

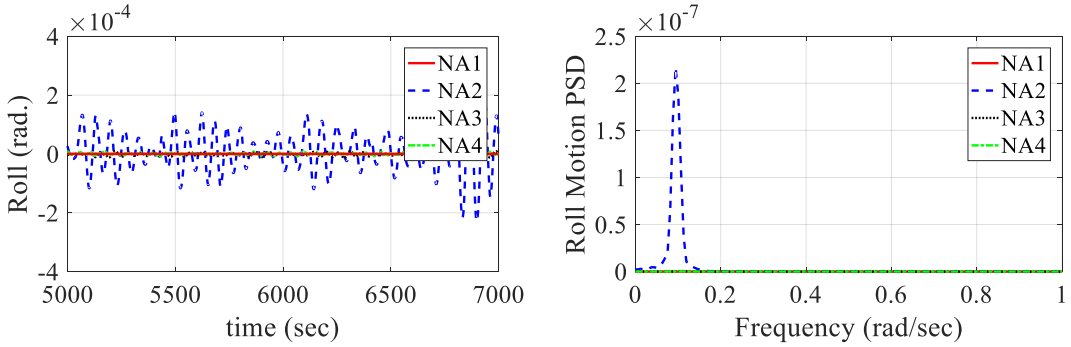

Figure 115. Time-series and PSD of 100-year roll motion

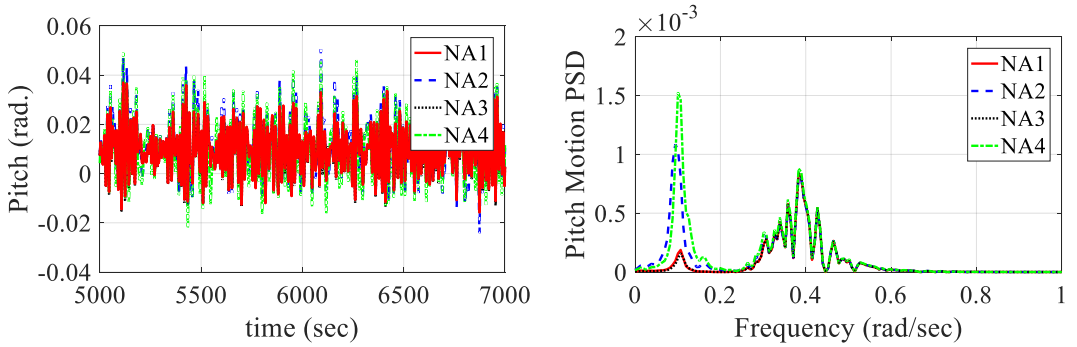

Figure 116. Time-series and PSD of 100-year pitch motion

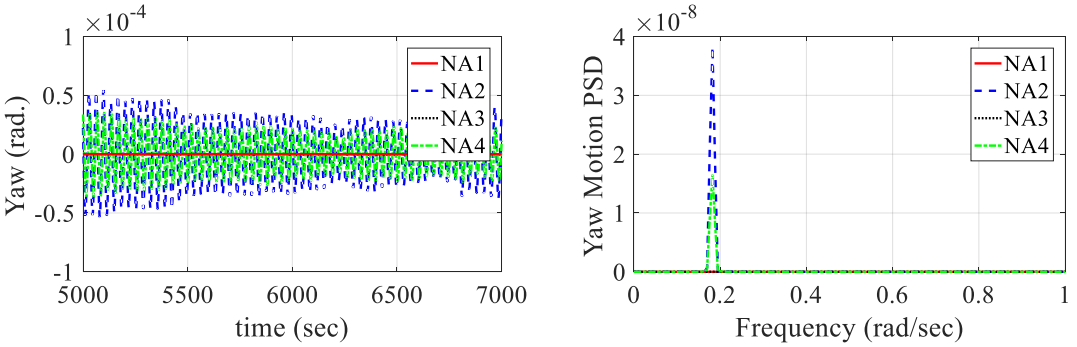

Figure 117. Time-series and PSD of 100-year yaw motion

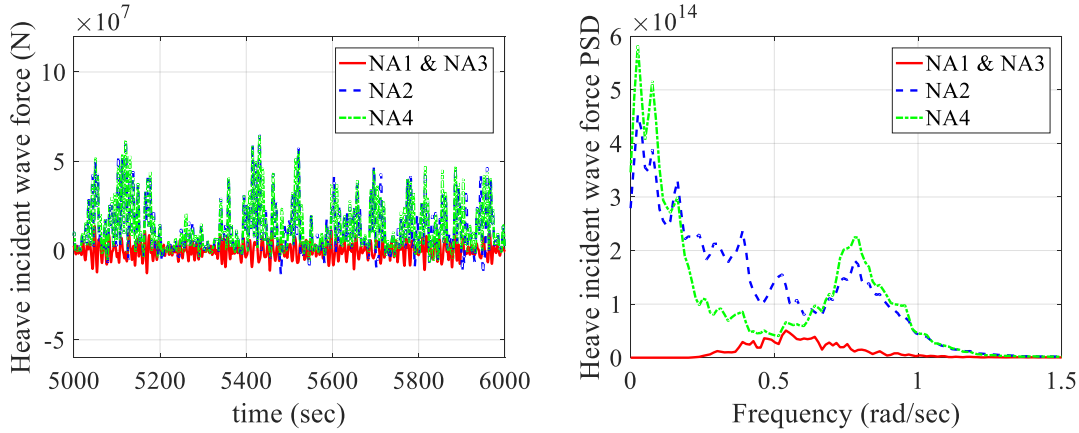

Figure 118. Time-series and PSD of incident heave forces

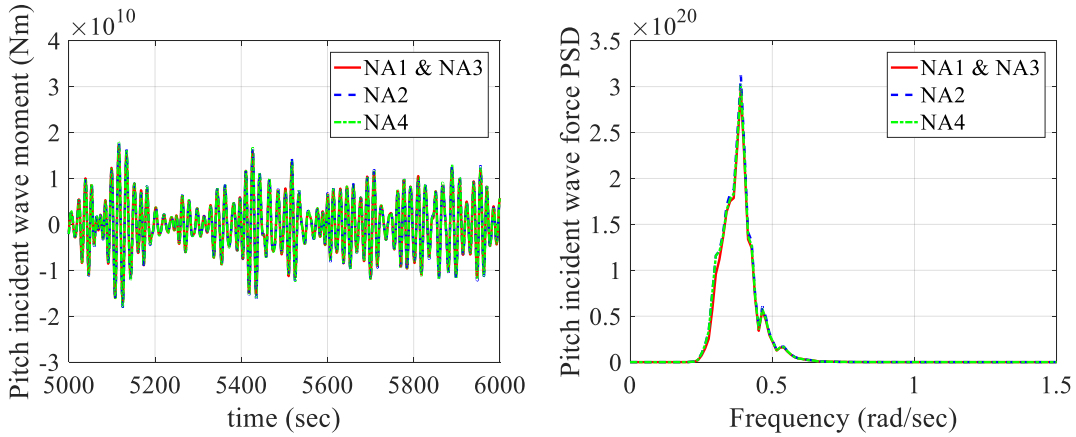

Figure 119. Time-series and PSD of incident pitch moments

Table 31. Statistics of an Arctic Spar platform under the 100-year storm condition

		Surge (m)	Sway (m)	Heave (m)	Roll (rad.)	Pitch (rad.)	Yaw (rad.)
NA1	Max.	19.250	0.000	1.784	0.000	0.042	0.000
	Min.	7.401	0.000	-2.167	0.000	-0.018	0.000
	Mean	12.960	0.000	0.007	0.000	0.010	0.000
	Std.	1.726	0.000	0.454	0.000	0.009	0.000
NA2	Max.	21.962	0.030	14.481	0.000	0.062	0.000
	Min.	6.634	-0.049	-4.728	0.000	-0.024	0.000
	Mean	13.266	-0.004	2.104	0.000	0.012	0.000
	Std.	1.948	0.010	2.875	0.000	0.011	0.000

Table 31. Continued

		Surge (m)	Sway (m)	Heave (m)	Roll (rad.)	Pitch (rad.)	Yaw (rad.)
NA3	Max.	19.018	0.002	2.036	0.000	0.040	0.000
	Min.	7.320	-0.002	-2.419	0.000	-0.019	0.000
	Mean	12.905	0.000	0.053	0.000	0.009	0.000
	Std.	1.725	0.001	0.512	0.000	0.009	0.000
NA4	Max.	21.090	0.008	6.490	0.000	0.056	0.000
	Min.	7.746	-0.013	-3.375	0.000	-0.027	0.000
	Mean	13.066	-0.002	1.082	0.000	0.010	0.000
	Std.	1.999	0.003	1.555	0.000	0.011	0.000

5.7 Conclusion

The Mathieu instability on Arctic Spar is investigated in both heave and pitch/roll directions by applying a nonlinear time-domain model, which considers the time-varying hydrostatic restoring forces (NA3) plus FK forces (NA2). The nonlinear simulation results are compared to the linear case. By deriving the MI equation for heave and pitch, the parameters in the Mathieu equation are defined and the stability diagram is discussed. From the numerical free-decay test, the natural frequency and damping ratio are determined and compared. A series of regular wave tests are carried out to examine the

nonlinear behavior of Arctic Spar including MI. Furthermore, the dynamic performance of Arctic Spar is considered under a 100-year storm condition. The conclusions drawn from the numerical simulations are summarized as follows.

- The numerical algorithm is validated by comparing the heave restoring stiffness and volume to the exact values. The difference in the restoring stiffness between the linear analysis and nonlinear analysis increases with increasing displacements. The heave coupling effect on the pitch restoring moment is more significant than the pitch coupling effect on the heave restoring force. It is also observed that the stiffness becomes either hardened or softened depending on the heave displacement.
- In the free-decay test, the effects of the nonlinear time-varying restoring stiffness are clearly observed. In heave and pitch, the decaying period changes in time because of the sloped hull surface near the waterline. As the motion is dampened and becomes small, the nonlinearity becomes insignificant, and the decaying period converges to the value of the linear analysis.
- The nonlinear FK force for Arctic Spar plays an important role when the wave frequency is close to the heave natural frequency, by preventing significantly enlarged resonance motion.
- A nonlinear analysis considering the time-varying restoring stiffness can capture the Mathieu instability of Arctic Spar at subharmonic resonant frequency, whereas a linear analysis cannot. In heave-to-pitch/roll, the parametric resonance occurs at the

wave frequency twice the pitch/roll natural frequency. As the wave height increases, instability is initiated earlier. The simulation results coincide well with the theoretical stability diagram.

- The same phenomenon of instability is observed in heave when the wave frequency is twice the heave natural frequency. This heave-to-heave MI is caused by the sloped hull surface near the waterline, and thus unique for Arctic Spar. The simulation results coincide well with the theoretical stability diagram. When nonlinear FK force generates excitations as the resonance motion develops by MI, the combined effects can further amplify the heave motion.

- According to a comparison of the motion amplitude per unit wave height, the heave motion in NA2 is smaller than that in NA1, in general. The influence of the wave height on the amplitude is also investigated. Due to the nonlinear viscous effect, the amplitude decreases with increasing wave height. The shift of the peak values is observed in NA2 due to nonlinear hydrostatic effects. It is also found that the range of Mathieu instability increases with increasing wave height.
- Under the 100-year-storm irregular-wave condition, significantly enlarged heave motions are observed as a result of heave-to-heave Mathieu instability, which can be of practical importance. Both nonlinear FK forces and nonlinear HC play equally important roles in triggering the phenomenon.

CHAPTER VI

CONCLUSIONS AND FUTURE WORK

6.1 General Conclusion

The dynamic interactions of level ice and offshore structures in three different interaction scenarios are presented using newly developed numerical simulation tools. Using a scientific background and modern numerical techniques, analytical and mechanical models of level ice are employed to estimate the ice load on offshore structures and are implemented into or coupled with either FAST, CHARM3D, or LIGGGHTS software. Throughout the extensive numerical simulations and systematical comparisons, the structural behavior is investigated in time domain.

In Chapter I, the motivation of this research on the interaction between ice-offshore structures is addressed. Although the development of arctic regions has occurred for decades, there is still a lack of standardized specifications for the design of arctic offshore structures because of the complexity of ice-structure interaction. In addition, according to the field and experiment data, significant structure motions induced by ice loads have been observed, which can cause serious damage to artic structures. Thus, the ice-structure interaction in three different approaches are explained in the following chapters.

In Chapter II a fixed-type monopile offshore wind turbine in level ice is investigated. The numerical algorithm to estimate the ice crushing load on a cylindrical structure is

implemented into FAST software. For verification, the numerical results are compared with the experimental data, which are reasonably well matched in terms of the magnitude and frequency of the ice load. The interaction of level ice and an offshore wind turbine is examined in both operating and parked conditions by varying the ice drift velocities. As a result, the three different crushing modes (i.e., ductile failure, frequency lock-in, continuous brittle crushing) are well described in the ice breaking model. In the parked condition, the wind turbine tower at an ice velocity of 0.05 m/s experiences resonance-type motion with a large amplitude and a frequency equal to the ice force frequency. However, the tower in the operating condition does not exhibit amplified motion due to the aerodynamic damping from the rotation of the wind turbine rotor. The results also showed that the blade is mainly influenced by the rotor rotation rather than the ice force.

In Chapter III, the floating Arctic Spar in level ice is investigated. The interaction of level ice and Arctic Spar is divided into three phases and numerically integrated in CHARM3D software by introducing the analytical equations of ice motion in each phase. The ice is modeled as an elastic beam on an elastic foundation, and the breaking, buoyancy, and frictional forces on Arctic Spar are considered in the numerical simulations. Extensive parametric studies are performed to identify the effects of ice properties on the estimation on the ice force. The ice force acting on Arctic Spar are compared with two theoretical methods with reasonable agreement. The dynamic characteristic of Arctic Spar including nonlinear mooring dynamics are also presented by varying ice velocity and thickness. In the low ice velocity range, due to the large ice impact force at very instant time, the structure drift away from the intact level ice and moves back again by mooring tensions.

For this reason, the structure motion in surge has the frequency equal to the surge natural frequency. In the high-speed range, ice forces apply continuously to the structure with high frequency, which results in a small amplitude structure motion in surge. The findings also reveal that that the pattern of mooring tensions is similar to that of surge motions.

In Chapter IV, a numerical simulation tool is used to investigate the level ice interaction with arbitrary-shaped floating offshore structures, and level ice is modelled with an assembly of multiple spherical particles. In addition, interaction with the structure is solved using the DEM with the parallel bond method. The open source software, LIGGGHTS, is coupled with CHARM3D, and the two programs solve the fully coupled ice-floater-mooring dynamics simultaneously by sharing the essential data. The particle properties used in the DEM are adopted from the physical ice properties, and the bonding strength is determined by a numerical three-point beam test. The ice load on the structure by the DEM is validated by comparing it with the model test data. For the level ice interaction with Arctic Spar, two Arctic Spar designs are considered and extensively compared with multiple numerical simulations.

In Chapter V, the nonlinear behavior of Arctic Spar including Mathieu instability is studied using a nonlinear time-domain simulation. The time-varying nonlinear HC and nonlinear FK force is computed by gridding the wetted surface of a hull at every timestep. According to the free-decay tests, due to the nonlinear stiffness, the natural frequency of the platform shifts to the low and high frequency regions in heave and pitch, respectively. The heave-to-pitch and heave-to-heave Mathieu-type instabilities are investigated in regular and irregular waves. The nonlinear time-domain simulation clearly demonstrates

that Mathieu-type instabilities occur when the incident wave frequency is twice the natural frequency of the platform, whereas a linear analysis cannot capture these instabilities. In a 100-year storm condition, the study shows that both nonlinear FK forces and nonlinear HC play equally important roles in triggering the Mathieu-type instability phenomenon.

6.2 Future Work

Since the ice flexural strength is much smaller than the ice crushing strength, a sloped structure at the waterline is recommended to prevent significant ice load. In Chapter II, the structural integrity of an offshore wind turbine system is assessed numerically by applying the ice crushing model. With development in Chapter III and Chapter IV, the dynamic response of offshore wind turbines could be examined, considering the level ice interaction with a sloped structure.

The analytical ice bending model in Chapter III could be potentially improved by: 1) adding a 3D effect in the ice breaking phase, 2) developing fluid interaction with broken ice pieces, and 3) analyzing the structural performance by combining other environmental loads such as current, wind, and wave loads.

The coupled ice-floater-mooring interaction in Chapter IV can be updated in a parametric study to investigate the effects of the ice thickness, the number of layers, and ice properties. The DEM model can also be improved by using a cubical-shaped particle and developing the nonlinear model for the interaction between bonded particles.

The significant nonlinear behavior of an Arctic Spar caused by an inverted conical-shaped hull is observed in Chapter V using nonlinear time-domain simulations. The heave-to-pitch Mathieu instability for a conventional Spar has been conducted and observed in experimental tests (Haslum and Faltinsen, 1999; Rho et al., 2005; Neves et al. 2008; Nallayarasu and Kumar, 2017). However, to the best of our knowledge, the experimental test for an Arctic Spar at a wave frequency near half of the heave natural frequency has not yet been conducted. A physical experimental test would be beneficial to understand the nonlinear behavior of Arctic Spar.

REFERENCES

Aksnes, V. (2010). A simplified interaction model for moored ships in level ice. *Cold regions science and technology, 63*(1-2), 29-39.

Ashby, M., Palmer, A., Thouless, M., Goodman, D., Howard, M., Hallam, S., . . . Ponter, A. (1986). *Nonsimultaneous failure and ice loads on arctic structures.* Paper presented at the Offshore Technology Conference.

Barker, A., & Sayed, M. (2012). Upward-or downward-breaking cones in ice: which one should you use? *Cold Regions Engineering 2012: Sustainable Infrastructure Development in a Changing Cold Environment* (pp. 715-724).

Barker, A., Sudom, D., & Sayed, M. (2015). *Conical Structures in Ice: Ride-Up, Radius and Results.* Paper presented at the OTC Arctic Technology Conference.

Barker, A., Timco, G., Gravesen, H., & Vølund, P. (2005). Ice loading on Danish wind turbines: part 1: dynamic model tests. *Cold regions science and technology, 41*(1), 1-23.

Bezzubik, O. N., Bitsulya, A. V., Karulin, E. B., Karulina, M. M., Klementyeva, N. Y., Sazonov, K. E., . . . Kupreev, V. V. (2004). *Experimental investigation of interaction of moored platforms with drifting ice features.* Paper presented at the 17th International Symposium on Ice.

Bird, K. J., Charpentier, R. R., Gautier, D. L., Houseknecht, D. W., Klett, T. R., Pitman, J. K., . . . Wandrey, C. R. (2008). Circum-Arctic resource appraisal: Estimates of undiscovered oil and gas north of the Arctic Circle: Geological Survey (US).

Bruun, P. K., Husvik, J., Le Guennec, S., & Hellmann, J.-H. (2009). *Ice model test of an Arctic SPAR.* Paper presented at the Proceedings of the International Conference on Port and Ocean Engineering Under Arctic Conditions.

Bruun, P. K., Løset, S., Gürtner, A., Kuiper, G., Kokkinis, T., Sigurdsen, A., & Hannus, H. (2011). *Ice Model Testing of Structures With a Downward Breaking Cone at the Waterline JIP: Presentation, Set-Up and Objectives.* Paper presented at the ASME 2011 30th International Conference on Ocean, Offshore and Arctic Engineering.

Cao, Y., Tahchiev, G., Zhang, F., Aarsnes, J. V., & Glomnes, E. B. (2010). *Effects of Hydrostatic Nonlinearity on Motions of Floating Structures.* Paper presented at the ASME 2010 29th International Conference on Ocean, Offshore and Arctic Engineering.

Chernetsov, V., & Karlinsky, S. (2006). *Ice-resistant spar-type platform for middle sea depth.* Paper presented at the The Sixteenth International Offshore and Polar Engineering Conference.

Chernetsov, V., Malyutin, A., & Karlinsky, S. (2008). *Floating production platform for polar seas designed to resist iceberg impact.* Paper presented at the The Eighteenth International Offshore and Polar Engineering Conference.

Comfort, G., Singh, S., & Spencer, D. (1999). Evaluation of ice model test data for moored structures.

Croasdale, K. (1978). *Ice forces on fixed rigid structures*.

Croasdale, K., Cammaert, A., & Metge, M. (1994). *A method for the calculation of sheet ice loads on sloping structures.* Paper presented at the IAHR Ice Symposium, Trondheim, Norway.

Dalane, O. (2014). Influence of pitch motion on level ice actions. *Cold regions science and technology, 108*, 18-27.

Dalane, O., Knudsen, F. F., & Løset, S. (2012). Nonlinear Coupled Hydrostatics of Arctic Conical Platforms. *Journal of Offshore Mechanics and Arctic Engineering, 134*(2), 021602.

DNVGL. (2012). Barents 2020: Assessment of international standards for safe exploration, production and transportation of oil and gas in the Barents Sea (Vol. Final Report Phase 4).

El-Dib, Y. O. (2001). Nonlinear Mathieu equation and coupled resonance mechanism. *Chaos, Solitons & Fractals, 12*(4), 705-720.

Eranti, E., Hayes, F., Maattanen, M., & Soong, T. (1981). Dynamic Ice-Structure Interaction Analysis for Narrow Vertical Structures.

Gravesen, H., Sørensen, S. L., Vølund, P., Barker, A., & Timco, G. (2005). Ice loading on Danish wind turbines: Part 2. Analyses of dynamic model test results. *Cold regions science and technology, 41*(1), 25-47.

Guérinel, M., Alves, M., & Sarmento, A. (2011). Nonlinear modelling of the dynamics of a free floating body. *EWTEC, Southampton*.

Haslum, H., & Faltinsen, O. (1999). *Alternative shape of spar platforms for use in hostile areas.* Paper presented at the Offshore technology conference.

Haslum, H. A. (2000). Simplified methods applied to nonlinear motion of spar platforms. *NTNU, Doctoral thesis*.

Heinonen, J., Hetmanczyk, S., & Strobel, M. (2011). *Introduction of ice loads in overall simulation of offshore wind turbines.* Paper presented at the Proceedings of the International Conference on Port and Ocean Engineering Under Arctic Conditions.

Hendrikse, H., & Metrikine, A. (2015). Interpretation and prediction of ice induced vibrations based on contact area variation. *International Journal of Solids and Structures, 75*, 336-348.

Hetenyi, M. Beams on elastic foundation, 1946. *Ann Arbor: University of Michigan Press*.

Hetmanczyk, S., Strobel, M., & Heinonen, J. (2011). *Dynamic ice load model in overall simulation of offshore wind turbines.* Paper presented at the The Twenty-first International Offshore and Polar Engineering Conference.

Hopkins, M. A. (1992). Numerical simulation of systems of multitudinous polygonal blocks: Cold Regions Research And Engineering Lab Hanover NH.

Hopkins, M. A. (1998). Four stages of pressure ridging. *Journal of Geophysical Research: Oceans, 103*(C10), 21883-21891.

Huang, G., & Liu, P. (2009). A dynamic model for ice-induced vibration of structures. *Journal of Offshore Mechanics and Arctic Engineering, 131*(1), 011501.

ISO. (2010). ISO 19906:2010 Petroleum and natural gas industries -- Arctic offshore structures. International Organization for Standardization.

Jacobsson, S., Karltorp, K., & Dolff, F. (2014). Towards a strategy for offshore wind power in Sweden.

Ji, S., Di, S., & Liu, S. (2015). Analysis of ice load on conical structure with discrete element method. *Engineering Computations, 32*(4), 1121-1134.

Jingrui, Z., Yougang, T., & Wenjun, S. (2010). A study on the combination resonance response of a classic spar platform. *Journal of vibration and control, 16*(14), 2083-2107.

Jochmann, P., & Evers, K. (2014). *Best Practice in Ice Model Testing On Moored Floaters.* Paper presented at the OTC Arctic Technology Conference.

Jonkman, J. M., & Buhl Jr, M. L. (2005). FAST user's guide. *National Renewable Energy Laboratory, Golden, CO, Technical Report No. NREL/EL-500-38230.*

Kärnä, T. (1994). Finite ice failure depth in penetration of a vertical indentor into an ice edge. *Annals of Glaciology, 19*, 114-120.

Kärnä, T., & Järvinen, E. (1994). *Dynamic unloading across the face of a wide structure.* Paper presented at the Proceedings of the 12th International Association of Hydraulic Engineering and Research on Ice Symposium (IAHR'94).

Kärnä, T., Kamesaki, K., & Tsukuda, H. (1999). A numerical model for dynamic ice–structure interaction. *Computers & structures, 72*(4-5), 645-658.

Kang, H.Y., & Kim, M.H. (2014). Safety assessment of Caisson transport on a floating dock by frequency-and time-domain calculations. *Ocean Systems Engineering, 4*(2), 99-115.

Karr, D. G., Troesch, A. W., & Wingate, W. C. (1993). Nonlinear dynamic response of a simple ice-structure interaction model. *Journal of Offshore Mechanics and Arctic Engineering, 115*(4), 246-252.

Kim, H., & Keune, J. N. (2007). Compressive strength of ice at impact strain rates. *Journal of materials science, 42*(8), 2802.

Kim, M.H. (2006). CHARM3D User Manual. *Offshore Technology Research Center, Texas A&M University*.

Kim, M.H., Koo, B.J., Mercier, R., & Ward, E. (2005). Vessel/mooring/riser coupled dynamic analysis of a turret-moored FPSO compared with OTRC experiment. *Ocean Engineering, 32*(14-15), 1780-1802.

Kim, M.H., Ran, Z., & Zheng, W. (2001). Hull/mooring coupled dynamic analysis of a truss spar in time domain. *International Journal of Offshore and Polar Engineering, 11*(01).

Kim, M.H., & Yue, D. (1991). Sum and difference-frequency wave loads on a body in unidirectional Gaussian seas.

Kloss, C., Goniva, C., Hager, A., Amberger, S., & Pirker, S. (2012). Models, algorithms and validation for opensource DEM and CFD–DEM. *Progress in Computational Fluid Dynamics, an International Journal, 12*(2-3), 140-152.

Koo, B.J., Kim, M.H., & Randall, R. (2004). Mathieu instability of a spar platform with mooring and risers. *Ocean Engineering, 31*(17-18), 2175-2208.

Kotras, T. V. (1983). Predicting ship performance in level ice. *SNAME Trans, 91*, 329-349.

Kry, P. (1978). *A Statistical Prediction of Effective Ice Crushing Stresses on Wide Structure.* Paper presented at the Proc. of IAHR Ice Symposium.

Kumar, N. S., & Nallayarasu, S. (2016). *Experimental and Numerical Investigation on the Effect of Varying Hull Shape Near the Water Plane on the Mathieu-Type Instability of Spar*. Paper presented at the ASME 2016 35th International Conference on Ocean, Offshore and Arctic Engineering.

Løset, S. (1994). Discrete element modelling of a broken ice field—Part I: model development. *Cold regions science and technology, 22*(4), 339-347.

Lindstrom, C. (1990). *Numerical estimation of ice forces acting on inclined structures and ships in level ice.* Paper presented at the Offshore Technology Conference.

Liu, J., Lau, M., & Williams, F. M. (2006). *Mathematical modeling of ice-hull interaction for ship maneuvering in ice simulations.* Paper presented at the Proceedings of 7th International Conference and Exhibition on Performance of Ships and Structures in Ice (ICETECH), Banff, Alberta, Canada.

Liu, L., & Ji, S. (2018). Ice load on floating structure simulated with dilated polyhedral discrete element method in broken ice field. *Applied Ocean Research, 75*, 53-65.

Liu, M., & Kronbak, J. (2010). The potential economic viability of using the Northern Sea Route (NSR) as an alternative route between Asia and Europe. *Journal of Transport Geography, 18*(3), 434-444.

Long, X., & Ji, S. (2017). *The Attributes of Local Ice Pressure Analyzed by Discrete Element Method.* Paper presented at the In Proc. of the 24th Int. Conf. on Port and Ocean Engineering under Arctic Conditions, POAC'17, Busan, Korea.

Lu, W., Lubbad, R., Høyland, K., & Løset, S. (2014). Physical model and theoretical model study of level ice and wide sloping structure interactions. *Cold regions science and technology, 101*, 40-72.

Määttänen, M. (2014). *Dynamic Ice Structure Interaction - Evolution in 50 Years*. Paper presented at the 22nd IAHR International Symposium on Ice, Singapore.

Matlock, H., Dawkins, W. P., & Panak, J. J. (1971). Analytical model for ice-structure interaction. *Journal of Engineering mechanics*.

Matsuishi, M., & Ettema, R. (1985). *The dynamic behavior of a floating, cable-moored platform continuously impacted by ice floes*: Iowa Institute of Hydraulic Research, the University of Iowa.

Mayne, D., & Brown, T. (2000). *Rubble pile observations.* Paper presented at the The Tenth International Offshore and Polar Engineering Conference.

Michel, B., & Toussaint, N. (1977). Mechanisms and theory of indentation of ice plates. *Journal of glaciology, 19*(81), 285-300.

Morgan, D., Sarracino, R., McKenna, R., & Thijssen, J. W. (2015). *Simulations of ice rubbling against conical structures using 3D DEM.* Paper presented at the Proceedings of the International Conference on Port and Ocean Engineering Under Arctic Conditions.

Murray, J., LeGuennec, S., Spencer, D., Yang, C. K., & Yang, W. (2009). *Model tests on a spar in level ice and ice ridge conditions.* Paper presented at the ASME 2009 28th International Conference on Ocean, Offshore and Arctic Engineering.

Murray, J., & Yang, C. (2009). *A comparision of spar and single column floater in an arctic environment.* Paper presented at the Offshore Technology Conference (OTC 10953). Houston, TX.

Nallayarasu, S., & Kumar, N. S. (2017). Experimental and numerical investigation on hydrodynamic response of buoy form spar under regular waves. *Ships and Offshore Structures, 12*(1), 19-31.

Nallayarasu, S., & Senthil Kumar, N. (2017). Experimental and numerical investigation on hydrodynamic response of buoy form Spar under random waves. *Ships and Offshore Structures, 12*(5), 734-746.

Nevel, D. E. (1965). A semi-infinite plate on an elastic foundation: Cold Regions Research And Engineering Lab Hanover NH.

Paavilainen, J., Tuhkuri, J., & Polojärvi, A. (2011). 2D numerical simulations of ice rubble formation process against an inclined structure. *Cold regions science and technology, 68*(1-2), 20-34.

Palmer, A. (2011). *Moving on from ISO 19906: What ought to follow?* Paper presented at the Proceedings of the International Conference on Port and Ocean Engineering Under Arctic Conditions.

Polojärvi, A., & Tuhkuri, J. (2009). 3D discrete numerical modelling of ridge keel punch through tests. *Cold regions science and technology, 56*(1), 18-29.

Polojärvi, A., & Tuhkuri, J. (2013). On modeling cohesive ridge keel punch through tests with a combined finite-discrete element method. *Cold regions science and technology, 85*, 191-205.

Potyondy, D. O., & Cundall, P. (2004). A bonded-particle model for rock. *International journal of rock mechanics and mining sciences, 41*(8), 1329-1364.

Ralston, T. (1979). *Sea ice loads.* Paper presented at the Technical seminar on Alaskan Beaufort Sea gravel island design.

Ralston, T. (1980). Plastic limit analysis of sheet ice loads on conical structures *Physics and Mechanics of Ice* (pp. 289-308): Springer.

Sablok, A., Ramachandran, M., & Kim, J. W. (2011). *Disconnectable arctic spar.* Paper presented at the OTC Arctic Technology Conference.

Salo, O., & Syri, S. (2014). What economic support is needed for Arctic offshore wind power? *Renewable and Sustainable Energy Reviews, 31*, 343-352.

Schulson, E. M. (2001). Brittle failure of ice. *Engineering fracture mechanics, 68*(17-18), 1839-1887.

Shi, W., Tan, X., Gao, Z., & Moan, T. (2016). Numerical study of ice-induced loads and responses of a monopile-type offshore wind turbine in parked and operating conditions. *Cold regions science and technology, 123*, 121-139.

Sodhi, D. S. (1998). Nonsimultaneous crushing during edge indentation of freshwater ice sheets. *Cold regions science and technology, 27*(3), 179-195.

Sodhi, D. S. (2001). Crushing failure during ice–structure interaction. *Engineering fracture mechanics, 68*(17-18), 1889-1921.

Timco, G., & Weeks, W. (2010). A review of the engineering properties of sea ice. *Cold regions science and technology, 60*(2), 107-129.

Wan, L., Gao, Z., & Moan, T. (2015). Experimental and numerical study of hydrodynamic responses of a combined wind and wave energy converter concept in survival modes. *Coastal Engineering, 104*, 151-169.

Wille, S. F., Kuiper, G. L., & Metrikine, A. V. (2011). *On the Dynamic Interaction Between Drifting Level Ice and Moored Downward Conical Structures: A Critical Assessment of the Applicability of a Beam Model for the Ice.* Paper presented at the ASME 2011 30th International Conference on Ocean, Offshore and Arctic Engineering.

Withalm, M., & Hoffmann, N. (2010). Simulation of full-scale ice–structure-interaction by an extended Matlock-model. *Cold regions science and technology, 60*(2), 130-136.

Yang, C. K., & Kim, M.H. (2011). The structural safety assessment of a tie-down system on a tension leg platform during hurricane events. *Ocean Systems Engineering, 1*(4), 263-283.

Yang, H., & Xu, P. (2015). Effect of hull geometry on parametric resonances of spar in irregular waves. *Ocean Engineering, 99*, 14-22.